Photon production in the Color Glass Condensate Formalism

Marius Constantin Cautun

Department of Physics
McGill University
Montréal, Québec H3A 2T8
Canada

July 2009

A Thesis submitted to the
Faculty of Graduate Studies and Research
in partial fulfillment of the requirements for the degree of
Master of Science

© Marius Constantin Cautun, 2009

Contents

List of Figures

List of Tables

Abstract

In this thesis, the classical field model developed by Krasnitz *et al.* is used to compute quark and photon production in heavy ion collisions. The first part of the thesis serves as an independent verification of previous results for quark production. To do so, an iterative method is developed to solve the non-linear system of equations that gives the initial condition for the gluonic field. In the second part, the expression giving the photon production rate is simplified using the symmetries and properties of the Color Glass Condensate and McLerran-Venugopalan models. From the two Feynman diagrams that give the leading order contribution, one is much larger than the other. The dominant diagram is given by a continuum spectrum with a very prominent peak superimposed on it.

Résumé

Dans cette thèse, le modèle développé par Krasnitz *et al.* basé sur les champs classiques est utilisé pour calculer la production de quarks et de photons dans les collisions d'ions lourds. La première partie de la thèse consiste en une vérification indépendante de certains résultats sur la production de quarks. Pour se faire, une méthode itérative est développée afin de solutionner le système d'équations non-linéaires qui donnent les conditions initiales du champ de gluon. Dans la seconde partie, l'expression donnant le taux de production de photons est simplifié en utilisant les symétries et les propriétés du *Color Glass Condensate* et du modèle de McLerran-Venugopalan. Deux diagrammes de Feynman donnent la contribution à l'ordre dominant mais l'un d'eux est plus important que l'autre. Le diagramme dominant donne un spectre continu superposé d'un pic proéminant.

Acknowledgments

I would like to start by giving the most sincere thanks to my supervisor Prof. Sangyong Jeon. My work and this thesis would not have been possible without his constant support, guidance and insightful ideas. He was always there to listen and give advice.

I am also grateful to Dr. François Fillion-Gourdeau for his work at the gluon time evolution code and for many helpful discussions. I found him to be a good explainer and a passionate physicist. Special thanks are also deserved by Dr. Bjoern Schenke for very productive discussions and to Dr. Tuomas Lappi for his correspondence.

I also thank my friends and colleagues Mohammed Mia, Gojko Vujanovic, Rémi Labrecque, Simon Caron-Huot, Jean-Francois Paquet and Adrian Buzatu for many stimulating and interesting conversations. I would also like to mention Paul Mercure and Juan Gallego for helping me with the technical details of the numerical simulations.

And last, but not least, I would like to thank my family for their constant support and understanding in my pursuit of physics. I give my deepest gratitude to my wife Claudia for her patience, encouragement and for proofreading my thesis.

1

Introduction

1.1 Heavy ion collisions

The goal of high energetic collisions is to produce and study new particles and states of matter that are not accessible in everyday physics on Earth. One can differentiate high energetic collisions in two important groups. The first involves collisions between elementary particles (like electrons, positrons) and/or single hadrons (like protons). This field is known as particle physics and the main goal of it is to discover the particles and interactions that govern the quantum world. Such collisions give rise to relatively few[1] particles that propagate in vacuum until hitting the detectors. Because of the small number of reaction products, the detected particles and interactions can be reconstructed individually. This is helpful in studying free particles as well as the interaction between particles in the absence of a medium. A famous example of such an experiment is the Large Electron-Positron Collider (LEP) which has run at beam energies of $\sqrt{s} = 90 - 200$ GeV[2][3]. It made very precise measurement for the mass of the W and Z bosons as well as constrained the number of light neutrino flavors to 3. Another important example is the Large Hadron Collider (LHC) which will run at a peak energy of $\sqrt{s} = 14$ TeV and is expected to find the Higgs boson (the only missing particle from the Standard Model (SM)) and look into new physics beyond

[1] Very high energy collisions can produce many particles, but this number is still small compared to the number of particles resulted from nucleus-nucleus collisions.

[2] The center of mass energy $\sqrt{s}$ is defined as $s = (k1 + k2)^2$ where $k1$ and $k2$ are the 4-momenta of the two colliding particles. $\sqrt{s}$ gives the maximum energy available to produce particles in a collision.

[3] The beam energy at LEP was increased over the lifetime of the collider.

SM, like supersymmetry and string theory.

The second category of high energy collisions are the ones between heavy ions which is the field of nuclear physics. These collisions involve large nuclei (like Au or Pb) and thus will result in a large number of reaction products. The only way to analyze such collisions is to use statistical observables averaged over many particles. This makes the task of studying the physical phenomena during the collision even more challenging, but it has the advantage of studying the properties of the elementary particles and interactions in the presence of a medium[1]. Moreover, these collisions are used to study the medium itself. This is especially important since in the very early universe the particles were in a medium similar to the one produced nowadays in heavy ion collisions (HIC). Typical examples here include the Relativistic Heavy-Ion Collider (RHIC) which collides protons and heavy ions at center of mass energies per nucleon pair[2] $\sqrt{s} = 200$ GeV and LHC which will also have heavy ion collisions at center of mass energies in the TeV range.

One of the most important goals of current high energy HIC experiments is the search for a new state of matter, the Quark Gluon Plasma (QGP). QGP has been inferred theoretically for over 25 years, but only recently, with the start of the RHIC experiment, did the collision energies become large enough such that it was expected to see the QGP. The QGP is defined as "a (locally) thermally equilibrated state of matter in which quarks and gluons are deconfined from hadrons, so that color degrees of freedom become manifest over nuclear, rather than merely nucleonic, volumes" [1]. This state of matter is believed to be present only in very extreme and energetic conditions, such as the early universe, neutron stars or high energy HIC.

Before going into more details about QGP, let us look in more detail at the current

[1]The medium is created by the very large number of particles produced during the collision.

[2]For HIC the center of mass energy $\sqrt{s}$ is defined per nucleon pair and not for the two nuclei. This is because only individual partons† from the two different nucleons collide to form new particles. Since each colliding parton can have at most the total energy of the nucleon which it is part of, the maximum energy available for new particle creation is given by the center of mass energies per nucleon pair. †Partons is a general term to denote the constituents of a nucleon, i.e. quarks and gluons.

understanding of HIC. The two colliding nuclei are moving towards each other at speeds close to the speed of light (0.99995c at RHIC). In the center of mass frame, due to the high Lorentz γ factor[1], the two nuclei will look like two "pancakes" moving towards each other. During the collision, partons from the first nucleus will interact with partons from the second nucleus to form new particles. The newly created particles will form a "fireball" that will expand until reaching the detector. More precisely, one can differentiate the following stages in a HIC:

1. Initial hard collisions
2. Pre-equilibrium
3. Thermalization
4. QGP
5. Hadronic phase
6. Free streaming

The first stage, that of hard collisions, takes place during the first instances of the collision between the two nuclei. It is characterized by a large momentum transfer between the interaction partons, so this stage is well described by perturbative Quantum Chromodynamics (QCD). The following two stages are the next steps in the evolution of the fireball towards a system in (at least local) thermal equilibrium. They involve additional particle production due to the hard partons inside the fireball. Moreover, due to collisions between different partons, the outcome of these two stages is a local thermal equilibrium. These stages are more difficult to model analytically due to the out of equilibrium processes taking place. There are several formulations that seem to give reasonable results, one of them being the Color Glass Condensate

[1]At the RHIC energies of $\sqrt{s} = 200$ GeV per nucleon pair, the Lorentz contraction factor is $\gamma \approx 100$ for each nucleus. Each nucleus has a longitudinal size given by $\frac{2R}{\gamma}$ with R the radius of the nucleus. Hence for $\gamma \approx 100$, the longitudinal size of the nucleus will be much smaller than the transverse one.

(CGC) formalism that is described in Sec. 2.2. An important part in describing the thermalization stage is played by the Boltzmann equation and transport theory.

At the end of the thermalization stage, the fireball is expected to be a system of hot and dense partons with a high energy density. At RHIC the energy density is estimated to be larger than 5 GeV/fm^3 [1, 2]. This is well above the estimated threshold of around 1 GeV/fm^3 necessary to obtain the QGP stage [3] (result calculated in lattice QCD simulations). Hence at RHIC there should already be a QGP stage. As the fireball expands further, the energy density decreases until it reaches the critical value when the QGP transforms into a gas of hadrons, called the hadronic phase. Both the QGP and hadronic state are well described by relativistic hydrodynamics. As the fireball expands even further, the mean free path between hadrons increases past the size of the system, then the hadrons become free streaming until they eventually end up in the detector.

The search and study of QGP proves to be experimentally challenging due to several reasons. The first is due to difficulties in describing analytically the 2nd and 3rd stages of the collision, since QCD is both non-linear and asymptotically free. The other main challenge comes from the experimental side, since the detectors measure only the final state of the collision and not the time evolution of the fireball. So to detect the QGP one must try and look for signatures which are particular to QGP only. A few such signatures are [4]:

- Suppression of high-p_T hadrons due to energy loss of a parton in QGP.
- Changes in the properties of heavy mesons (J/Ψ, Ψ') due to the color Debye screening in QGP.
- Enhancement of thermal photon and dileptons due to emission from deconfined QCD plasma.

RHIC data shows evidence for the existence of a thermalized medium that can be explained only by the presence of a QGP state [1, 2]. Due to the high background of a HIC, the experimental data includes signals from all the stages of the HIC collision.

This is why is very important to have theoretical models that give good predictions for all the stages of the collision. Only then the contribution of the QGP stage can be singled out and matched with the experimental data.

The photon spectrum can be a good probe for QGP. It has the main advantage that photons, due to the smallness of the fine structure constant, once produced, propagate trough the medium with only very little interaction. Hence photons are very good probes of all the stages of HIC collision. The downside of the method is that the detector cannot distinguish between photons created at different stages during the collision, since it measures only the total flux of photons. Since photons are produced in all the stages, with the exception of the last one, there is a need for theoretical models to compute photon production in all HIC stages.

1.2 Objectives and statement of originality

In the previous section we tried to argue that HIC are very complex phenomena that require a good understanding of every stage of the fireball in order to obtain theoretical predictions which can be compared with experimental data. The main goal of this thesis is to develop and asses the feasibility of computing the photon spectrum within the CGC formalism, which is believed to give a good description of the first instant in HIC. Such a result, together with photon production calculations for the other stages of the collision, when compared to experimental data, can be used to give a better understanding of HIC. The main advantage of using photons as a probe is that they have a very small interaction probability with the medium, and hence they travel unimpeded, giving information from all the stages of HIC.

This thesis is organized as follows. In Sec. 2 we shortly revise the basic properties of QCD and give an introduction to the CGC and McLerran-Venugopalan (MV) models. We also present the Schwinger-Keldysh formalism which is primarily used in finite temperature quantum field theory as well as in condensed matter physics. These give the background material necessary for understanding this thesis. In Sec. 3 we present the classical field model developed by Krasnitz *et. al.* to describe the

gluon time evolution and study quark production within this model. We discuss at length the discretization of the Dirac equation since it presents several challenges. We end the section with an independent check of previous numerical results for quark pair production within the CGC formalism. Sec. 4 is dedicated to photon production in the CGC and MV models. We start by presenting the computations for the photon production rate, expression which we then particularize for the CGC and MV models. We end the section with numerical tests and results for the photon production spectrum.

The work in this thesis presents several original contributions by the author:

- The development of an iterative method for solving the non-linear set of equations that give the initial condition for the gluon time evolution algorithm.
- A simplification of the expression that gives the photon production rate using the symmetries and properties of the CGC and MV models.
- Numerical results for the photon production rate.

2

Background material

We start this section with a very short overview of classical Quantum Chromodynamics (QCD), which is the theory of strong interaction. Classical QCD represents the framework in which we obtain all the results presented in the thesis. We then continue with the Color Glass Condensate formalism (CGC). We argue why the CGC represents a good description for the early stages of the fireball, after which we present some of the main features of the theory. We end this section with a short introduction in the Schwinger-Keldysh formalism for fermions, which is used in Secs. 3.3 and 4.2 to compute quark pair production and photon production rates respectively.

In this thesis we use natural units where $c = \hbar = 1$. We mostly work in the light cone coordinates which are defined as:

$$x^{\pm} = \frac{1}{\sqrt{2}}(t \pm z) \tag{2.1}$$

and which have associated the light cone momenta:

$$p^{\pm} = \frac{1}{\sqrt{2}}(E \pm p_z). \tag{2.2}$$

In this coordinate system, the scalar product is given by $x \cdot y = x^+y^- + x^-y^+ - \mathbf{x_T} \cdot \mathbf{y_T}$ where $\mathbf{x_T}$ denote the transverse components of the 4-vector. The energy momentum relation reads $2p^+p^- - m_T^2 = 0$ where m_T is the transverse mass given by $m_T^2 = p_T^2 + m^2$. Another useful variable is the momentum rapidity which is given by:

$$y = \frac{1}{2}\ln\left(\frac{E + p_z}{E - p_z}\right) = \frac{1}{2}\ln\left(\frac{p^+}{p^-}\right) = \ln\left(\frac{\sqrt{2}p^+}{m_T}\right) \tag{2.3}$$

where the last expression can be easily shown using the dispersion relation. Additional information about the relations between different coordinate systems and the

transformation rules between them can be found in Appendix A.1.

The Einstein summation convention is implied each time there are two repeating indices. Greek letters will be used when summing over the spatial directions while Latin letters will be used when summing over group elements in the adjoint representation. Moreover, the letter i will be used when summing over the transverse directions. We also make use of the notations $\not{\partial} = \partial_\mu \gamma^\mu$ and $\bar{u} = u^\dagger \gamma^0$.

2.1 The Classical QCD theory

Quantum Chromodynamics (QCD) is the theory of strong interaction which describes the interactions of quarks and gluons. QCD together with Quantum Electrodynamics (QED), weak interaction and the much anticipated Higgs boson form the Standard Model (SM), which is the accepted current theory that describes particle physics. The QCD (in the larger picture of the SM) was shown to give predictions in good agreement with the experimental data in both e^+e^- and proton-antiproton collisions [5, 6]. The QCD is a $SU(3)$ Yang-Mills theory whose degrees of freedom are quarks and gluons. The theory is invariant under local gauge transformation of the $SU(3)$ group. The Lagrangian of the theory is given by:

$$\mathcal{L}(x) = -\frac{1}{4} G_{\mu\nu,a}(x) G_a^{\mu\nu}(x) + \sum_{f=1}^{n_f} \bar{\Psi}_f^\alpha(x)[i \not{D}_{\alpha\beta} - m_f]\Psi_f^\beta(x) \tag{2.4}$$

with the non-abelian field tensor and covariant derivative given by:

$$G_a^{\mu\nu}(x) = \partial^\mu A^\nu(x) - \partial^\nu A^\mu(x) - g f_{abc} A_b^\mu(x) A_c^\nu(x) \tag{2.5}$$

$$D_{\alpha\beta}^\mu = \partial^\mu \delta_{\alpha\beta} + i g A_a^\mu(x) t_{\alpha\beta}^a \tag{2.6}$$

where α and β run from 1 to 3 and represent indices for the fundamental representation of $SU(3)$. $A_a^\mu(x)$ represents the gluonic fields in the adjoint representation and t^a are the $SU(3)$ group generators. f_{abc} is the structure constant and g is the strong coupling constant. Ψ_α^f is the wavefunction of the quark species f with corresponding mass m_f. To keep notation simple, in the following we will refer to only one quark species, so we will drop the index f. Moreover we will also drop the index α from Ψ

such that from now on Ψ will represent a vector in the fundamental representation of $SU(3)$.

The Lagrangian given in Eq. (2.4) is not enough to describe QCD completely; one must also provide values for the strong coupling constant g, the number of flavors n_f and for the quark masses m_f. Under the current development of the SM, there is no analytical way to predict the values of the above set of parameters, so they must be measured experimentally. Experimental results show that there are 6 quark flavors with masses which run widely from $m_{up} = 3$ MeV to $m_{top} = 171$ GeV [7]. The value of the coupling constant runs with the energy scale, which will be discussed later on.

Starting from the Lagrangian in Eq. (2.4), the classical equations of motion are given by:

$$(i\not{D} - m)\Psi(x) = 0 \tag{2.7}$$

$$[D_\nu, G^{\nu\mu}] = J^\mu \tag{2.8}$$

where $J^\mu = g\bar{\Psi}(x)\gamma^\mu\Psi(x)$ is the source term. The above two equations are known as the Dirac equation and the Yang-Mills equation respectively.

Since QCD is a local gauge invariant theory under the $SU(3)$ group, it is interesting to see how the gauge and fermion fields charge under a gauge transformation. A gauge transformation is given by an element $V(x)$ of the group $SU(3)$ and is generally represented as:

$$V(x) = \exp(i\theta_a(x)t_a) \tag{2.9}$$

with arbitrary real numbers $\theta_a(x)$. The fermion field transforms via:

$$\Psi'(x) = V(x)\Psi(x). \tag{2.10}$$

The gauge invariance requirement for the Lagrangian density in Eq. (2.4) requires that the term $\bar{\Psi}(x)D_\mu\Psi(x)$ remains invariant, so we must have:

$$D'_\mu(x) = V(x)D_\mu V^{-1}(x). \tag{2.11}$$

Using Eq. (2.6) it is obvious that the gauge field $A^\mu(x) = A^\mu_a(x)t_a$ must gauge transform via:

$$A'_\mu(x) = V(x)A_\mu(x)V^{-1}(x) - \frac{i}{g}V(x)\left(\partial_\mu V^{-}1(x)\right) \tag{2.12}$$

$$G'_{\mu\nu}(x) = V(x)G_{\mu\nu}(x)V^{-1}(x) \tag{2.13}$$

where the gauge transformation for the field tensor was found using the gauge transformation for the gauge field $A_\mu(x)$ and Eq. (2.5). Now it is obvious that indeed the QCD Lagrangian is gauge invariant since both terms of Eq. (2.4) are gauge invariant separately. The terms given in Eq. (2.4) are not the only possible combinations of terms that are gauge invariant. In fact the term $\epsilon_{\mu\nu\delta\rho}G^{\mu\nu}(x)G^{\delta\rho}$ is also gauge invariant and has dimension 4. So theoretically there is no reason why this term should be absent from the QCD Lagrangian, but experimentally (by measuring CP conservation) this term was found to be absent. Additional gauge invariant terms must be of dimension higher than 4, but such terms are problematic due to renormalizability of the quantum QCD theory.

In this thesis we will work only within the confines of the classical QCD theory, so we only shortly discuss the features of the quantized QCD theory. The classical theory given in Eq. (2.4) can be quantized using path integral techniques with the help of the Fadeev-Popov method which is discussed at length in [8]. In the quantized theory, the Lagrangian density will have new terms in addition of those from Eq. (2.4). These terms are due to the gauge fixing procedure and also due to the addition of unphysical fields called "ghosts".

An important feature of the quantized QCD theory is the asymptotic freedom which means that the strong coupling constant g decreases with increasing energy scale. So short range interactions between strong interacting fields (high momentum transfer) are weak, whereas long range interactions are strong. This behavior leads to the phenomenon of confinement. A qualitative interpretation is that by increasing the distance between quarks, at some point it becomes energetically favorable to create a quark-antiquark pair rather than to further increase the distance.

The strong-interaction analogue of the fine structure constant $\alpha_s = g^2/(4\pi)$ varies

depending on the energy scale according to the following equation[1] [8]:

$$\alpha_s(Q^2) = \frac{4\pi}{\left(11 - \frac{2}{3}n_f\right)\ln\left(\frac{Q^2}{\Lambda^2}\right)} \tag{2.14}$$

where Q is the energy scale we consider and Λ is another energy scale that can be found using experimental data. n_f is the number of quark flavors with a mass smaller than Q. Experimental results yield a value of $\Lambda \approx 200$ MeV ([8]). This energy scale is important since for $Q \approx \Lambda$, α_s is of order 1 or higher, so we are in the strong coupling regime of QCD. On the other hand, for $Q \gg \Lambda$, α_s will be small, so one can use perturbation theory techniques to analytically make QCD predictions. In the following, we will denote this important energy scale by Λ_{QCD}.

In the classical QCD theory, the coupling constant, the quark masses and wave-function renormalization constants are scale independent. This is the case since in the classical theory there are no loops, as is the case for the quantum theory. So to be able to have a good treatment of the physical phenomena at a given scale using the classical theory, one must use the corresponding values of the above constants at that given energy scale, values which have to be taken from the quantum theory.

2.2 The Color Glass Condensate formalism

The Color Glass Condensate (CGC) is a formalism meant to describe the initial stages of heavy ion collisions. The name of the theory comes from the following concepts [9, 10]:

1. Color: CGC describes strong interactions of color charged particles.

2. Glass: There are two characteristics time scales. The soft particles evolve much faster in time than the hard ones. This is similar to the behavior of glass, which is solid on short time scales but is disordered and liquid on long time scales.

3. Condensate: At high energies, due to saturation effects, there is a wide momentum range with a high density of gluons. The gluon density saturates at a small

[1] Eq. (2.14) is valid only to leading order in perturbation theory.

coupling constant, which is similar to a Bose-Einstein condensate.

At high energies, QCD cannot be described perturbatively, even though the strong coupling constant is small, due to large densities of partons. In this case, one uses CGC as an effective theory to describe high energy scattering in QCD. One of the main features of CGC is that it incorporates the saturation effects due to a large density of gluons. The goal of CGC is to provide insight into outstanding concepts of QCD in the asymptotically large energies. More precisely, it can be used to compute observables as particle multiplicity or cross-section dependence on rapidity and transverse momentum.

2.2.1 Experimental observations leading to CGC

To be able to understand the underlying concepts of CGC, we must start with some experimental observation in high energy heavy ion collisions. The collisions consist of two nuclei moving towards each other at a speed that is very close to the speed of light (0.9995 c at RHIC). Due to such high speeds, the Lorentz γ factor will be around 100 or higher, so the nuclei will be highly Lorentz contracted along the direction of motion. Moreover, for high center of mass energies, most of the interactions during the collision should involve a large momentum transfer ($Q \gg \Lambda_{QCD}$). So the collision can be treated in the approximation of a small strong coupling constant, according to Eq. (2.14). In such a setting, the following were observed in nuclear physics experiments:

1. The high energy partons lose only a small fraction of the available energy.

2. The density of gluons increases with the decreasing x (fraction of longitudinal momentum) as well as with the increasing momentum transfer Q.

The first observation can be inferred from Fig. 2.1. This shows the rapidity distribution of net-protons for different beam energies. For small energies most of the resulting particles are clustered around mid-rapidity which suggests that the valence partons inside the nuclei can lose a considerable fraction of their energy. But as the

collision energy increases, an important shift takes place. Most of the resulting particles will be at rapidities close to the beam rapidity, suggesting that they lose only a small fraction of their energy.

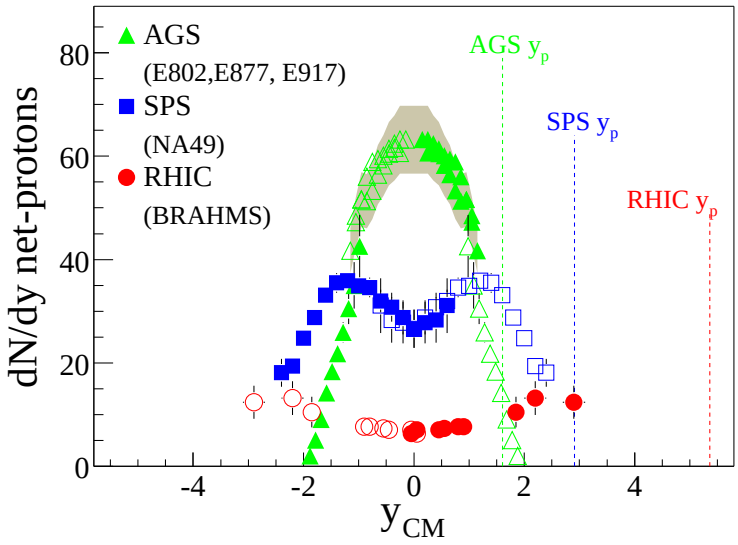

Figure 2.1: Net-proton rapidity distribution in central collisions for AGS (Au+Au at $\sqrt{s} = 5$ GeV), SPS (Pb+Pb at $\sqrt{s} = 17$ GeV) and RHIC (Au+Au at $\sqrt{s} = 200$ GeV) [11]. Even though the beam rapidity at RHIC is $y = 5.4$, the experimental setup allows for measurements only up to $y \leq 3$.

To get a more quantitative understanding, let us follow the reasoning in [9, 10]. Let us consider the beam moving in the positive z direction and with momentum $(P^+, P^-, \mathbf{0})$. The rapidity of the beam is $y_{beam} = \ln\left(\frac{\sqrt{2}P^+}{M}\right)$. A particle moving in the same direction but with a smaller longitudinal momentum given by $p^+ = xP^+$[1] has a rapidity given by:

$$y = \ln\left(\frac{\sqrt{2}p^+}{m_T}\right) = y_{beam} - \ln\left(\frac{1}{x}\right) + \ln\left(\frac{M}{m_T}\right). \tag{2.15}$$

with m_T the transverse mass of the particle. So for rapidities close to the beam rapidity, we have $x \approx \frac{m_T}{M}$. One can differentiate two extreme cases, when the particle

[1] x is called the longitudinal momentum fraction and is defined as:

$$x = \frac{p^+}{P^+}$$

with p^+ the particle momentum and with P^+ the beam momentum. This definition is valid only for a direction of motion in the positive z direction. For an opposite direction of motion, one must use p^- and P^-.

mass $m \approx M$ and the second when $m \ll M$. When the particle mass m is similar to M, since $x \leq 1$, we must have $x \approx 1$ and $p_T \approx 0$. When $m \ll M$ we still have $x \approx 1$, but in this case $p_T^2 \approx M^2$ suggesting a very large transfer of transverse momentum. So the valence partons during the collision will lose only a very small fraction of the longitudinal momentum and are characterized by large values of x.

On the other hand, particles moving at mid-rapidity ($y \approx 0$) have typical longitudinal momentum fractions given by $x \approx \frac{m_T}{\sqrt{s}}$. This means that the more energetic the collisions are, the smaller the values of x probed in the collision are.

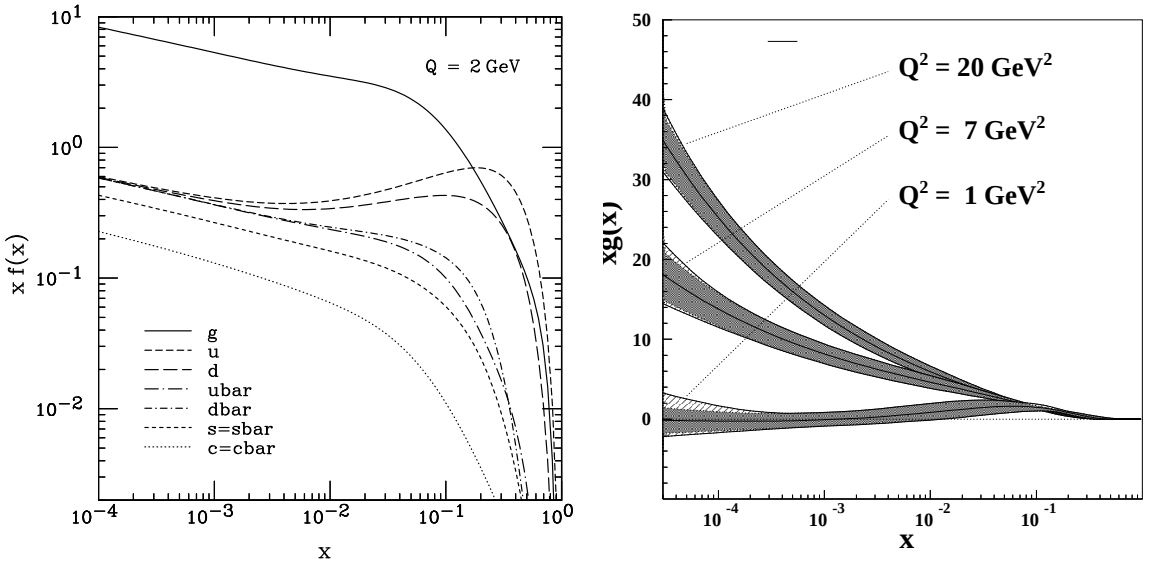

Figure 2.2: Left: The ZEUS results for gluon and quarks PDFs at transverse momentum $Q = 2$ GeV [12]. Right: The ZEUS results for gluon PDF for different transverse momenta Q [13]. The shaded regions represent the error range of the result.

The second important experimental observation is the behavior of the parton distribution functions (PDF)[1] with x and Q (the transverse momentum). At small x, the gluons are the dominant constituents of the hadrons, as can be seen from Fig. 2.2 left graph. As the collision energy increases, the average transferred momentum increases as well. So for higher energies, the number of gluons for a given x becomes even larger, as can be seen from the right panel in Fig. 2.2. This is why it is believed

[1]PDF are defined as the probability for finding a parton inside a hadron with a given momentum fraction x for a given transverse momentum Q^2. Due to the non-perturbative nature of low energy QCD, the only known values for PDFs are the ones inferred from experimental data.

that at high energies one can deal only with the gluons and neglect the rest of the partons.

The high gluon density at small x yields a very important approximation in the CGC model. The gluonic field can be treated classically since the quantum coherent states will have a large occupancy number $\propto 1/\alpha_s \gg 1$ [9, 10]. In this limit, commutations between the creation and annihilation operators can be neglected[1].

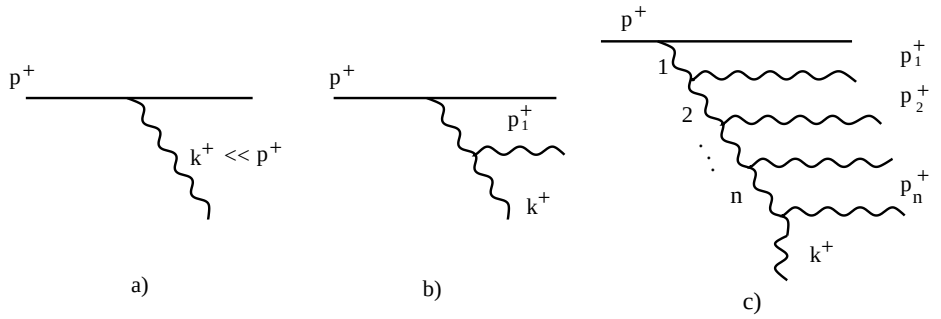

Figure 2.3: Feynman diagrams for small x gluon emission from a fast parton. a) The lowest order (LO) emission. b) LO emission plus LO radiative correction. c) Gluon cascade.

Now let us analyze in more detail the reason behind the enhancement of gluon distribution functions at small x. This leads to an important distinction between the hard degrees of freedom (large x) and the soft ones (small x). To get the qualitative behavior it is enough to look only at the tree diagrams, but to get the full result one also has to include self-energy insertions and vertex corrections. Typical tree level diagrams included in this analysis are shown in Fig. 2.3. Fig. 2.3 a) shows the emission of a gluon with momentum $k^+ = xP^+$ (P^+ is the beam momentum) by a parton with momentum $p^+ = x_0P^+$. Since we want to analyze the small x behavior, we must have $1 > x_0 \gg x$. Fig. 2.3 b) shows the next radiative correction to the process from Fig. 2.3 a). This correction will have a contribution proportional to [9, 10]:

$$\alpha_s \ln\left(\frac{x_0}{x}\right) \tag{2.16}$$

[1]The commutator between the creation and annihilation operators is of order 1 and hence much smaller than the typical products of operators which are of order N, the number of particles.

which is higher order in the coupling constant α_s. But, due to the large value of $\ln\left(\frac{x_0}{x}\right)$, even for small α_s (weak coupling limit), the diagram from Fig. 2.3 b) brings a leading order contribution to the gluon emission process. In general, any tree level diagram as the one shown in Fig. 2.3 c) with the additional requirement:

$$p^+ \gg p_1^+ \gg \ldots \gg p_n^+ \gg k^+ \tag{2.17}$$

will bring a contribution proportional to:

$$\left(\alpha_s \ln\left(\frac{x_0}{x}\right)\right)^n. \tag{2.18}$$

Similarly to Eq. (2.16), the above contribution is to leading order even in the small coupling limit. So a process that produces n gluons is as important as a process that produces one gluon. To be able to get a consistent result to LO, one must sum the contributions from all the tree diagrams shown in Fig. 2.3[1].

The strong ordering in the momenta from Eq. (2.17) also implies a strong ordering in the lifetimes of the emitted gluons. To see this, let us start from the Heisenberg uncertainty principle that $\Delta x^+ \Delta k^- \sim 1$[2], which when applied to our problem leads to:

$$\Delta x^+ \sim \frac{1}{k^-} = \frac{2k^+}{m_T^2} = \frac{2xP^+}{m_T^2} \tag{2.19}$$

where we used $2k^+k^- - m_T^2 = 0$ and that $k^+ = xP^+$. This shows that the lifetime of soft gluons is much smaller than that of hard gluons. For the general case of the gluon cascade shown in Fig. 2.3 c), the above result is generalized to:

$$\Delta x_1^+ \gg \Delta x_2^+ \gg \ldots \gg \Delta x_{n-1}^+ \gg \Delta x_n^+. \tag{2.20}$$

Since the average interaction time of the gluons is proportional to their lifetime, the small x gluons will see the hard gluons as frozen in time. This separation of scales

[1] A complete calculation for the gluon distribution function yields [9, 10]:

$$xg(x, Q^2) \propto x^{-4 \ln 2 \, \alpha_s \frac{N_c}{\pi}}.$$

This implies that the gluon number increases continuously as x becomes smaller and smaller.

[2] One can refer to x^+ as the light cone "time" [9, 10]. Since on the light cone $p \cdot x = p^- x^+ + p^+ x^- - \mathbf{p_T} \cdot \mathbf{x_T}$ it is natural to interpret p^- as the light cone "energy".

between soft and hard gluons is very important in the CGC formalism. It allows treating the hard gluons as static sources of color charge.

2.2.2 Saturation momentum

Up to now we saw that the gluonic density increases very fast with small x values. Then the logical question to ask is: does the gluon density increase indefinitely or is there a process which regulates the increase and can even cause gluon saturation? Indeed, gluon recombination can lead to gluon saturation. A typical Feynman diagram of such a process can be seen in Fig. 2.4. The main absorption of gluons does not come from interactions with quarks (since the quark density is much smaller than the gluon one) but from interactions with other gluons. This process is not enhanced by large logarithms (as is the case for the processes in Fig. 2.3), but if the gluon density is large enough, it can have an important effect. This is because gluon absorption probability is directly proportional to the gluon density.

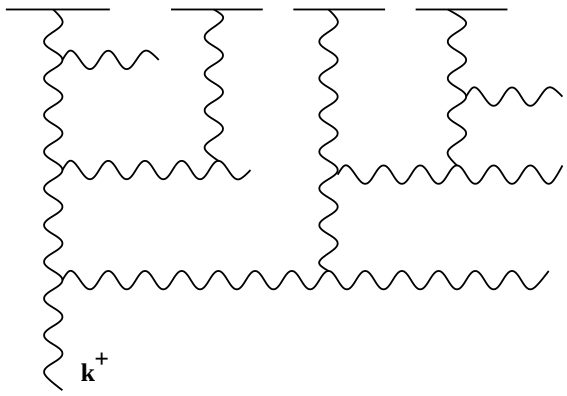

Figure 2.4: A typical Feynman diagram that is implicitly resumed in the CGC formalism. This is an example of gluon recombination. The horizontal lines represent hard partons.

More quantitatively, the interaction probability for gluons from different parton cascades can be estimated as [14]:

$$\sigma(Q^2) \times n(x, Q^2) \sim \frac{\alpha_s N_c}{Q^2} \times \frac{1}{N_c^2 - 1} \frac{xG(x, Q^2)}{\pi R^2} \tag{2.21}$$

where $\sigma(Q^2)$ is the cross-section for gluons with transverse momentum Q^2 and $n(x, Q^2)$ is the density of gluons of a given color at transverse momentum Q^2 and longitudinal

momentum fraction x. πR^2 is the transverse size of the nucleus while $G(x, Q^2)$ is the gluonic PDF of the nucleus. This probability becomes large when:

$$Q_s^2 \simeq \frac{\alpha_s N_c}{N_c^2 - 1} \frac{xG(x, Q_s^2)}{\pi R^2} \tag{2.22}$$

where Q_s is the saturation momentum, i.e. the scale for which the saturation effects become important. For $Q^2 \gg Q_s^2$ the saturation effects (that give rise to non-linear effects) can be neglected and one can use linear evolution equations. But for $Q^2 \lesssim Q_s^2$ the saturation effects are essential and are expected to tame the growth of the gluon distribution functions which we found in the previous section.

A parametric estimation for Q_s yields [14]:

$$Q_s^2(x, A) \sim A^{\delta} x^{-\lambda} \tag{2.23}$$

with the exponents $\delta \approx 0.3$ and $\lambda \approx 0.3$ [15]. Using the above parametrization it is straightforward to see that we can obtain $Q_S^2 \gg \Lambda_{QCD}$ as long as the nucleus is large and x small enough. In this case we are in a regime with $\Lambda_{QCD} \ll Q^2 < Q_s^2$ where even though the coupling is small, non-linear effects play a very important role. Experimental data estimate that the saturation scale is about 1-2 GeV at RHIC and 2-3 GeV at LHC [15].

2.2.3 Classical CGC

CGC is the effective theory designed to cope with the separation of the soft and hard degrees of freedom and with the saturation effects in the weak coupling limit. The main features of the CGC formalism (summarized in the introduction of [14]) are:

1. Classical Yang-Mills theory for the soft degrees of freedom, so the time evolution is given by Eq. (2.8). The classical fields represent the small x gluons.

2. The gauge field sources propagate nearly at the speed of light and their internal dynamics is "frozen". They represent the hard degrees of freedom, like valence quarks. These sources do not participate directly in the scattering (as we saw in the previous sections), but act as color sources for the small x gluons.

3. The color charges are given by a random distribution. We will argue this statement later on.

At saturation, the color fields are strong and thus one must solve the full non-linear Yang-Mills equation. By doing so, one also takes into account the saturation effects.

Let us start by analyzing the properties of the source term in the Yang-Mills equation. We have a nucleus that is moving very close to the speed of light in the x^+ direction (in 4-dimensional space-time). The current is proportional to the velocity so the current will be given by $J_a^\mu = \delta^{\mu+}\rho_a^V$ with ρ_a^V the volume density of color charge. The hard degrees of freedom are frozen in time compared to the soft ones, thus the charge density is independent on x^+, yielding:

$$J_a^\mu = \delta^{\mu+}\rho_a^V(x^-, \mathbf{x_T}). \tag{2.24}$$

To simplify calculations even more, one can take the limit when the nucleus moves with the speed of light. Then, due to the Lorentz contraction, the color charge density can be taken only as a function of the transverse coordinate, such that we finally obtain:

$$J_a^\mu = \delta^{\mu+}\delta(x^-)\rho_a(\mathbf{x_T}) \tag{2.25}$$

where $\rho_a(\mathbf{x_T})$ denotes the transverse surface color charge density. The justification for such a form is based on the Heisenberg principle. The color charge sources, the hard partons, have a high p^+ and hence due to the uncertainty principle, they are well localized on the x^- direction. On the other hand, the soft partons have small x and hence much smaller k^+. So they are much more spread along the x^- direction, effectively seeing the color sources as delta functions on the x^- direction.

Let us denote with $W[\rho]$ the weight function which characterizes the random distribution of color charges. The weight function must have the property:

$$\int \mathcal{D}\rho\, W[\rho] = 1 \tag{2.26}$$

where $\mathcal{D}\rho$ means a sum over all possible charge configurations. The weight function $W[\rho]$ depends on the dynamics of the large x partons and hence is an external input

to the CGC model. Physical observables are obtained by averaging the solution of the Yang-Mills equation over different charge configurations. Quantitatively, the physical observable $\mathcal{O}$ is given by:

$$\langle \mathcal{O} \rangle = \int \mathcal{D}\rho \, W[\rho] \mathcal{O}[\rho] \tag{2.27}$$

where $\mathcal{O}[\rho]$ denotes the value of $\mathcal{O}$ computed using a given distribution of charge density ρ.

The only piece still missing is the weight function $W[\rho]$. A complete treatment for computing $W[\rho]$ must also include the dependence of the weight function on the scale x of the soft partons. To see why this is the case, just imagine that as we probe smaller x values, there will be more and more high x values that become "frozen" because of reducing the x of soft gluons. Such effects can be included and will give rise to a renormalization group equation for $W[\rho]$. This is known as Jalilian-Iancu-McLerran-Weigert-Leonidov-Kovner (JIMWLK) evolution equation. Such a complex treatment is beyond the scope of this thesis, so we restrict to a simpler model for obtaining the weight function.

The weight function $W[\rho]$ can be obtained using the McLerran-Venugopalan (MV) model in the limit of very large nuclei ($A \gg 1$) [16, 17, 18]. Let us start by looking at a soft parton with transverse momentum k_T. If $k_T \leq \Lambda_{QCD}$ than the parton is confined within a hadron inside the nucleus. If $k_T > \Lambda_{QCD}$ than the parton has a transverse size $\delta x_T \sim \frac{1}{k_T}$ (simply due to the uncertainty principle). At the same time, its size along the longitudinal direction is given by $\Delta x^- \sim \frac{1}{k^-} = \frac{1}{xP^+} \sim \frac{\Delta X^-}{x}$ with ΔX^- the longitudinal size of a nucleus. Hence this small x parton has a much larger longitudinal size than a nucleus. This means that along the longitudinal direction, the parton will feel the average charge from many nuclei which are in the tube of transverse area $(\delta x_T)^2$. So the parton interacts simultaneously, on average, with $N_{valence}$ valence partons. The number of valence partons can simply be computed as:

$$N_{valence} = n(\delta x_T)^2 = \frac{N_c A}{\pi R_A^2} (\delta x_T)^2 \tag{2.28}$$

where n is the density of valence partons in the transverse plane. If we take the nucleus uniform in the transverse plane, than n is just the total number of valence partons in the nucleus divided by the transverse area. Since $R_A \propto A^{\frac{1}{3}}$, Eq. (2.28) reduces to $N_{valence} \propto A^{\frac{1}{3}}$. This means that as the nucleus size increases, the soft partons will feel the interaction with more and more hard partons. Since the partons belong to different hadrons, they are uncorrelated due to confinement. Moreover, due to the large number of valence partons, one can treat them as classical sources. Adding up all this, we obtain that the weight function can be approximated with a Gaussian probability distribution. This can be argued by using the central limit theorem in the limit of a very large nucleus. So, within the MV model, one obtains a Gaussian weight:

$$W[\rho] = \mathcal{N} \exp\left(-\frac{1}{2g^2\mu_A^2}\int d^2\mathbf{x_T}\rho^2(\mathbf{x_T})\right) \tag{2.29}$$

where μ_A^2 is the density of charge squared fluctuations per unit area divided by g^2 and $\mathcal{N}$ is a normalization constant. The parameter μ_A^2 can be determined from elementary calculations. The averaged color charge square of a quark is $\langle Q^2\rangle = \frac{4}{3}g^2$, combining with the transverse density of valence quarks gives [16]:

$$\mu_A^2 = \frac{4}{3}\frac{3A}{\pi R_A^2} = 1.1\ A^{\frac{1}{3}}\ \text{fm}^{-2} \tag{2.30}$$

where the last equation was computed using that $R_A \approx 1.1\ A^{\frac{1}{3}}$ fm. Now, starting with Eq. (2.29), we can evaluate the color charge correlation function to be:

$$\langle \rho^a(\mathbf{x_T})\rho^b(\mathbf{y_T})\rangle = g^2\mu^2\delta^2(\mathbf{x_T}-\mathbf{y_T}). \tag{2.31}$$

The MV model is based on heuristic arguments and is not derived from first principles of QCD. It is however a solution of the JIMWLK equation in the mean field approximation, so it can be used to get the hard parton color charge density for the CGC model.

2.3 The Schwinger-Keldysh formalism

The Schwinger-Keldysh formalism was developed in the 1960's in the context of many-body quantum field theory in/out-of equilibrium [19, 20]. It is used primarily in finite

temperature quantum field theory as well as in condensed matter physics.

The standard formalism for zero-temperature (in equilibrium) quantum theories involves the adiabatic switch "on" and "off" of the interactions in the distant past and future respectively. The system starts at $t \to -\infty$ in the state $|0_{\text{in}}\rangle$ of the non-interacting system, then the interactions are turned on and off, such that at $t \to +\infty$ the system is in the state $|0_{\text{out}}\rangle$. The crucial assumption is that $|0_{\text{out}}\rangle$ is unique and independent on the details of the interactions that are switched on and off. So the final state at $t \to +\infty$ is $|0_{\text{in}}\rangle$ up to a phase factor.

This is not the case for out-of equilibrium processes. Starting from some arbitrary non-equilibrium state, and then switching the interactions on and off leads to a new state which clearly depends on the details of the interaction. Thus the entire reasoning sketched in the previous paragraph fails for out-of equilibrium theories. Schwinger's suggestion is to take the final state the same as the initial one, but to let the quantum system evolve first in the forward time direction and then again to evolve the system back in time [21]. This time evolution is sketched in Fig. 2.5 by the contour $\mathcal{C}$. Following the time path $\mathcal{C}$, it does not matter what the final state of the system is, since the system returns back to the initial state.

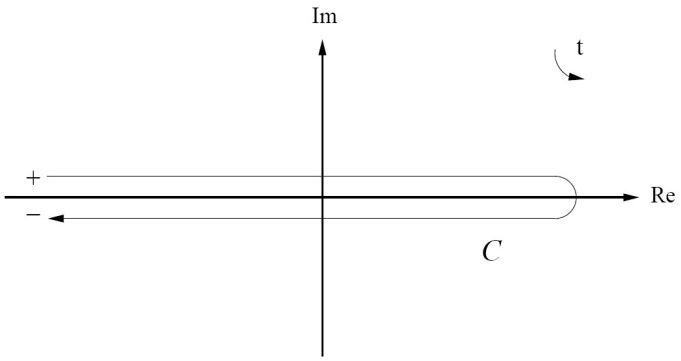

Figure 2.5: The closed time path used in the SK formalism.

But the SK approach has a price, a doubling of the degrees of freedom. At every moment in time one needs to specify a field residing on the upper branch (denoted by $+$) as well as on the lower branch (denoted by $-$) of path $\mathcal{C}$. The main difference between a zero field theory and the SK formalism is that in the latter each time we

compute field correlations we need to order the fields in time according to path $\mathcal{C}$. We will do so by inserting the path-order operator $\mathcal{P}_\mathcal{C}$ which forces the fields to be ordered with decreasing time, from left to right.

Due to the doubling of the degrees of freedom, there are two types of fields, the $+$ and the $-$ ones. These give rise to two types of vertices, denoted by $+$ and $-$, who have a $-$ sign difference between the contributions they bring. When considering internal vertices, one must sum over both the $+$ and $-$ vertices.

2.3.1 SK formalism for fermions

In the following we follow the approach in [22], which even though is presented for a scalar field, can be easily generalized for fermion fields. We will need this formalism when computing the photon production rate in Sec. 4.

According to Wick's theorem, any n point correlation function can be expressed only in terms of 2 point functions. In the SK formalism there are 4 such 2 point functions which for fermions are given by:

$$D_{e_1e_2}(x,y) = \langle 0_{\text{in}}|\mathcal{P}_\mathcal{C}\bar{\Psi}^{e_1}(x)\Psi^{e_2}(y)|0_{\text{in}}\rangle \tag{2.32}$$

where with $e_{1,2}$ we denote the two types of fields, the $+$ and $-$ ones. These are known as the full propagators. The free quark propagators are defined as in Eq. (2.32) but using the "in" fields. We get:

$$D^0_{++}(x,y) \equiv \langle 0_{\text{in}}|\mathcal{P}_\mathcal{C}\bar{\Psi}^+_{\text{in}}(y)\Psi^+_{\text{in}}(x)|0_{\text{in}}\rangle = \langle 0_{\text{in}}|T\bar{\Psi}_{\text{in}}(y)\Psi_{\text{in}}(x)|0_{\text{in}}\rangle \tag{2.33}$$

$$D^0_{--}(x,y) \equiv \langle 0_{\text{in}}|\mathcal{P}_\mathcal{C}\bar{\Psi}^-_{\text{in}}(y)\Psi^-_{\text{in}}(x)|0_{\text{in}}\rangle = \langle 0_{\text{in}}|\bar{T}\bar{\Psi}_{\text{in}}(y)\Psi_{\text{in}}(x)|0_{\text{in}}\rangle \tag{2.34}$$

$$D^0_{+-}(x,y) \equiv \langle 0_{\text{in}}|\mathcal{P}_\mathcal{C}\bar{\Psi}^-_{\text{in}}(y)\Psi^+_{\text{in}}(x)|0_{\text{in}}\rangle = -\langle 0_{\text{in}}|\bar{\Psi}_{\text{in}}(y)\Psi_{\text{in}}(x)|0_{\text{in}}\rangle \tag{2.35}$$

$$D^0_{-+}(x,y) \equiv \langle 0_{\text{in}}|\mathcal{P}_\mathcal{C}\bar{\Psi}^+_{\text{in}}(y)\Psi^-_{\text{in}}(x)|0_{\text{in}}\rangle = \langle 0_{\text{in}}|\bar{\Psi}_{\text{in}}(y)\Psi_{\text{in}}(x)|0_{\text{in}}\rangle \tag{2.36}$$

where T and $\bar{T}$ denote the time and anti-time ordering. In momentum space the

above propagators are given by:

$$D^0_{++}(p) = i\frac{\not{p} + m}{p^2 - m^2 + i\epsilon} \tag{2.37}$$

$$D^0_{--}(p) = -i\frac{\not{p} + m}{p^2 - m^2 - i\epsilon} \tag{2.38}$$

$$D^0_{+-}(p) = \theta(-p_0)(\not{p} + m)\ 2\pi\delta(p^2 - m^2) \tag{2.39}$$

$$D^0_{-+}(p) = \theta(p_0)(\not{p} + m)\ 2\pi\delta(p^2 - m^2) \tag{2.40}$$

Using the above definition it is easy to see that not all the 4 propagators are independent, but in fact they are related via:

$$D^0_{++} + D^0_{--} = D^0_{+-} + D^0_{-+}. \tag{2.41}$$

In the following it is useful to write the above propagators in matrix form via:

$$D^0 = \begin{pmatrix} D^0_{++} & D^0_{+-} \\ D^0_{-+} & D^0_{--} \end{pmatrix} \text{ and } \Sigma = \begin{pmatrix} \Sigma_{++} & \Sigma_{+-} \\ \Sigma_{-+} & \Sigma_{--} \end{pmatrix} \tag{2.42}$$

where Σ is the self-energy matrix (each element of it denotes the self-energy between those two type of vertices). Now we are ready to write the full propagator as:

$$D(x, y) = D^0(x, y) - i \int d^4z d^4z' D^0(x, z)\Sigma(z, z')D(z', y) \tag{2.43}$$

which is known as the Lippmann-Schwinger integral equation. This equation can be solved to find the full propagators. The easiest way to solve the Lippmann-Schwinger equation is to do a change of basis for the propagators. A clever change of basis, which uses Eq. (2.41) to get rid of one of the propagators, is called the Advanced-Retarded (RA) basis. The change of basis is given by the matrix:

$$U = \frac{1}{\sqrt{2}} \begin{pmatrix} 1 & -1 \\ 1 & 1 \end{pmatrix} \tag{2.44}$$

such that the new propagator matrix becomes:

$$D^0_{RA} = \begin{pmatrix} 0 & D^0_A \\ D^0_R & D^0_S \end{pmatrix} \tag{2.45}$$

where D_A^0, D_R^0 and D_S^0 are the free advanced, retarded and symmetric propagators. They are given by [23]:

$$D_A^0(x,y) \equiv \theta(x_0 - y_0)\langle 0_{\rm in}|\{\Psi_{\rm in}(x), \bar{\Psi}_{\rm in}(y)\}|0_{\rm in}\rangle \tag{2.46}$$

$$D_R^0(x,y) \equiv -\theta(y_0 - x_0)\langle 0_{\rm in}|\{\Psi_{\rm in}(x), \bar{\Psi}_{\rm in}(y)\}|0_{\rm in}\rangle \tag{2.47}$$

$$D_S^0(x,y) \equiv \langle 0_{\rm in}|[\Psi_{\rm in}(x), \bar{\Psi}_{\rm in}(y)]|0_{\rm in}\rangle. \tag{2.48}$$

And in momentum space their expressions are given by:

$$D_A^0(p) = i\frac{\not{p} + m}{p^2 - m^2 - ip_0\epsilon} \tag{2.49}$$

$$D_R^0(p) = i\frac{\not{p} + m}{p^2 - m^2 + ip_0\epsilon} \tag{2.50}$$

$$D_S^0(p) = (\not{p} + m)\ 2\pi\delta(p^2 - m^2) \tag{2.51}$$

Now, in the RA basis, Eq. (2.43) is particularly simple to solve due to the simplified expression for the D_{RA}^0 matrix. Using iterative insertion of the Lippmann-Schwinger equation within itself, we obtain [22]:

$$D_{-+}(x,y) = \int d^4z d^4z' [D_R (D_R^0)^{-1}](x,z)\ D_{-+}^0(z,z')\ [(D_A^0)^{-1} D_A](z',y) \tag{2.52}$$

$$D_{+-}(x,y) = \int d^4z d^4z' [D_R (D_R^0)^{-1}](x,z)\ D_{+-}^0(z,z')\ [(D_A^0)^{-1} D_A](z',y) \tag{2.53}$$

where:

$$[D_R (D_R^0)^{-1}](x,z) = D_R(x,z)(-i\overleftarrow{\not{\partial}}_z - m) \tag{2.54}$$

$$[(D_A^0)^{-1} D_A](z',y) = (i\overrightarrow{\not{\partial}}_{z'} - m) D_A(z',y) \tag{2.55}$$

with D_A and D_R the full advanced and retarded propagators. The free propagators $D_{-+}^0(z,z')$ and $D_{+-}^0(z,z')$ can be simply obtained from Eq. (2.39) and Eq. (2.40) by taking the inverse Fourier transform. We will use these expressions when computing the photon production rate in Sec. 4.

3

Gluon and quark production

In this section we will shortly revise the theoretical framework as well as the numerical details for the gauge field evolution and solutions of the Dirac equation within the CGC and MV models [24, 25, 26]. This is necessary since photon production is a complex process that involves many steps. In the initial stages of heavy ion collision photons are emitted only by quarks. So to compute photon production one needs to know the quarks wavefunction inside the fireball resulted from the collision. On the other hand, to compute the Dirac field associated to soft quarks one needs to know the gauge field associated with small x gluons. Hence the first step is to start from a calculation of the gluonic field within the CGC formalism. The theoretical and numerical background of such a calculation were developed in [24, 25]. The next step is the computation of the quarks wavefunction, based on the model and algorithm described in [26]. And finally, the quark wavefunction can be used to compute the quark propagators and hence photon production.

We start in Sec. 3.1 with a short revision of the formalism developed in [24, 25] to compute the gauge field. This computation is done within the framework of the classical field theory due to the high number of gluons present at small x. We present the most important details from [24, 25] for both the continuum and the lattice theories. The gluon field calculation is simplified by the boost invariance of the gauge fields. The initial condition for the gauge fields on the lattice involves the solution of a non-linear set of equations. We developed an iterative method for solving the set of non-linear equations, method that we present in Sec. 3.2.

In Sec. 3.3 we describe the necessary steps to compute the quark wavefunction in

the gluonic background field described in the previous paragraph. We closely follow the derivation from [26]. This task is computationally intensive both because the Dirac field has to be considered for the full 3 dimensional lattice and since the Dirac equation has to be discretized implicitly due to explicit dependence of the equation on time and spatial coordinates. We deal with these problems in Sec. 3.4.

We end with Sec. 3.5 that presents the numerical results for both gluon and quark pair production within the CGC and MV formalisms. We use the results for both testing the numerical code and to give an independent verification of the results already published in [26, 27, 28, 29, 30, 31].

3.1 Gluon production in CGC

3.1.1 Continuum Model

The theoretical formalism for describing the gauge field created in the collision of two high energy nuclei within the CGC theory was developed in [24, 25]. Ref. [32] and [27, 28, 33] computed gluon production and other gauge observable for $SU(2)$ and $SU(3)$ respectively.

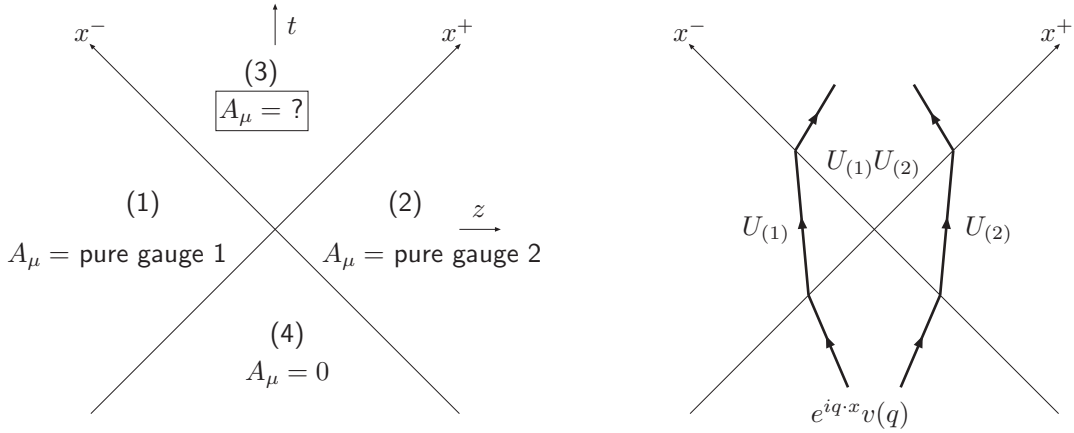

Figure 3.1: The light cone coordinate representation of two colliding nuclei in the limit of moving at the speed of light. Left: The background gauge fields in the CGC formalism. Right: The two possible way for a Dirac field to propagate from $t \to -\infty$ to $\tau = 0$.

The current produced by the two colliding nuclei is given by:

$$J^\mu = \delta^{\mu+}\delta(x^-)\rho_{(1)}(\mathbf{x_T}) + \delta^{\mu-}\delta(x^+)\rho_{(2)}(\mathbf{x_T}) \tag{3.1}$$

where we denoted with $\rho_{(1),(2)}$ the static charge densities for the two nuclei; with nucleus 1 moving along the x^+ direction and with nucleus 2 moving in opposite direction (see Fig. 3.1). The above current is just the sum of the two individual currents of each nuclei that are given within the CGC and MV models (see Sec. 2.2 for additional details). The charge current from Eq. (3.1) gives rise to pure gauge fields in the regions denoted with (1) and (2) in the left panel of Fig. 3.1. The transverse fields are given by [34, 35]:

$$A^i_{(m)}(\mathbf{x_T}) = \frac{i}{g} e^{i\Lambda_{(m)}(\mathbf{x_T})} \partial_i e^{-i\Lambda_{(m)}(\mathbf{x_T})}, \text{ with} \tag{3.2}$$

$$\nabla_{\mathbf{T}}^2 \Lambda_{(m)}(\mathbf{x_T}) = -g\rho_{(m)}(\mathbf{x_T}) \tag{3.3}$$

where $m = 1, 2$ denotes the two nuclei (and also regions (1) and (2) in Fig. 3.1) and $i = 1, 2$ denotes the two transverse directions. The rest of the field components, i.e. $A^{\pm}$, are 0.

Eqs. (3.1) - (3.3) are valid only in the light cone (LC) gauge of each nucleus[1] [34, 35]. For $\tau = 0$, the LC gauges for the two nuclei are the same and also coincide with the temporal gauge $A_\tau = (A^+x^- + A^-x^+)/\tau = 0$. In the following we work within the temporal gauge which has the advantage of allowing the use of a Hamiltonian formalism.

To find the initial conditions for the field inside region (3) of the left panel in Fig. 3.1 one must require that the fields of different regions match smoothly on the light cone. By doing so, one obtains [34, 35]:

$$A^i_{(3)}(\mathbf{x_T})|_{\tau=0} = A^i_{(1)}(\mathbf{x_T}) + A^i_{(2)}(\mathbf{x_T}) \tag{3.4}$$

$$A^\eta_{(3)}(\mathbf{x_T})|_{\tau=0} = \frac{ig}{2}[A^i_{(1)}(\mathbf{x_T}), A^i_{(2)}(\mathbf{x_T})]. \tag{3.5}$$

The above initial conditions are boost invariant, therefore it is natural to assume that the field inside region (3) of the left panel in Fig. 3.1 is also boost invariant[2].

[1] LC gauge is given by $A^+ = 0$ (respectively $A^- = 0$) for the nucleus moving in the x^+ direction (respectively x^- direction).

[2] Ref. [34] has shown that the boost invariance of the pure gauge fields $A^i_{(1),(2)}$ makes the equations of motion boost invariant.

This means that one must not perform rapidity dependent gauge transformation. This requirement reduces the A_η field component to a adjoint scalar field that we will denote with ϕ.

In the $A_\tau = 0$ gauge the Hamiltonian density is given by [25]:

$$\mathcal{H} = \ \mathrm{Tr}\left\{\frac{1}{\tau}E^i E^i + \frac{\tau}{2}F_{ij}F_{ij} + \tau\pi^2 + \frac{1}{\tau}[D_i,\phi][D_i,\phi]\right\} \tag{3.6}$$

with $i = 1, 2$ denoting the transverse direction and with the momenta given by:

$$E^i = -\tau\partial_\tau A^i \tag{3.7}$$

$$\pi = \frac{1}{\tau}\partial_\tau\phi. \tag{3.8}$$

Starting from Eq. (3.6), the equations of motion can be found by taking the Poisson brackets between the fields and the Hamiltonian such that for any quantity x we have $\dot{x} = \{\mathcal{H}, x\}$.

3.1.2 Lattice description

Using the Kogut-Susskind procedure described in [36], and following the steps detailed in [25], the continuum Hamiltonian density reduces to the following version for the lattice case:

$$\mathcal{H}_\mathcal{L} = \frac{g^2}{\tau}\ \mathrm{Tr}E^i E^i + \frac{2N_c\tau}{g^2}\left(1 - \frac{1}{N_c}\ \mathrm{Re}\ \mathrm{Tr}U_{1,2}\right) + \tau\ \mathrm{Tr}\pi^2 + \frac{1}{\tau}\sum_i\ \mathrm{Tr}(\phi - \tilde{\phi}_i)^2$$

where E^i and π are the canonical momenta defined via:

$$E^i_a = \frac{2i\tau}{g^2}\ \mathrm{Tr}(t_a U_i \dot{U}_i^\dagger) \tag{3.9}$$

$$\pi = \frac{1}{\tau}\dot{\phi} \tag{3.10}$$

and represent the transverse and respectively the longitudinal electric fields. The notation $\dot{U}_i$ denotes a derivative with respect to proper time τ. U_i are the link matrices on the lattice which are defined as:

$$U_\mu(x) = e^{igaA_\mu(x)} \tag{3.11}$$

where a is the lattice constant[1]. With $U_{i,j}$ we denoted the plaquette in the transverse plane which is given by:

$$U_{i,j}(\mathbf{x_T}) = U_i(\mathbf{x_T})U_j(\mathbf{x}+\mathbf{e_i})U_i^\dagger(\mathbf{x}+\mathbf{e_j})U_i^\dagger(\mathbf{x_T}) \tag{3.12}$$

where e_μ is the unit vector along the μ direction times the lattice spacing in that direction ($\mathbf{x_T}+\mathbf{e}_\mu$ gives the coordinates of the next neighbor in the μ direction for the lattice point $\mathbf{x_T}$). We also defined the parallel transport field $\tilde{\phi}$ as:

$$\tilde{\phi}_i = U_i(\mathbf{x_T})\phi(\mathbf{x_T}+\mathbf{e_i})U_i^\dagger(\mathbf{x_T}) \tag{3.13}$$

with no implicit sum over the index i.

The link matrix gauge transforms like:

$$U_i(\mathbf{x_T}) \to V(\mathbf{x_T})U_i(\mathbf{x_T})V^\dagger(\mathbf{x_T}+\mathbf{e_i}) \tag{3.14}$$

while the longitudinal gauge field transforms via:

$$\phi(\mathbf{x_T}) \to V(\mathbf{x_T})\phi(\mathbf{x_T})V^\dagger(\mathbf{x_T}) \tag{3.15}$$

with the gauge transformation $V(x)$ an $SU(N_c)$ group element. Using the above equations it is easily seen that the lattice Hamiltonian density is gauge invariant.

Using the Poisson brackets relations, it can be easily shown that the equations of motion are given by [25]:

$$\dot{U}_i = \frac{ig^2}{\tau}E^iU_i \text{ (no sum over } i) \tag{3.16}$$

$$\dot{\phi} = \tau\pi \tag{3.17}$$

$$\dot{E}^1 = \frac{i\tau}{2g^2}\left(U_{1,2}+U_{1,-2}-\text{h.c.}\right) - \text{trace} + \frac{i}{\tau}[\tilde{\phi}_1,\phi] \tag{3.18}$$

$$\dot{E}^2 = \frac{i\tau}{2g^2}\left(U_{2,1}+U_{2,-1}-\text{h.c.}\right) - \text{trace} + \frac{i}{\tau}[\tilde{\phi}_2,\phi] \tag{3.19}$$

$$\dot{\pi} = \frac{1}{\tau}\sum_i\left(\tilde{\phi}_i+\tilde{\phi}_{-i}-2\phi\right) \tag{3.20}$$

[1]Even though $U_\mu(x)$ is defined at x, it is an object which "lives" at $x+\frac{1}{2}e_\mu$. The link matrices are used to transport fields from one lattice point to another, such that quantities at different lattice points can be evaluated independent of gauge. A few examples are the $\tilde{\phi}$ field defined in Eq. (3.13) or the covariant derivative given in Eq. (3.60).

where with "h.c." we denoted the Hermitian conjugate of the expression within the brackets. The "-trace" term means subtracting the part proportional to the unit matrix since $E^i = \sum_a E^i_a t_a$.

The last step for the lattice theory is to find the initial conditions at $\tau = 0$ for the fields in region (3) of the left panel in Fig. 3.1. These initial conditions are given by [25]:

$$\mathrm{Tr}\left[t_a \left(U_i^{(1)} + U_i^{(2)}\right)\left(1 + U_i^{\dagger(3)}\right) - \mathrm{h.c.}\right] = 0 \tag{3.21}$$

which gives the link matrices $U_i^{(3)}$ in region (3) at $\tau = 0$ and:

$$\begin{aligned}\pi(\mathbf{x_T}) = \sum_i \frac{-i}{4g}\Big[&\left(U_i^{(3)}(\mathbf{x_T}) - 1\right)\left(U_i^{\dagger(2)}(\mathbf{x_T}) - U_i^{\dagger(1)}(\mathbf{x_T})\right) - \mathrm{h.c.} \\ &+ \left(U_i^{\dagger(3)}(\mathbf{x_T} - \mathbf{e_i}) - 1\right)\left(U_i^{(2)}(\mathbf{x_T} - \mathbf{e_i}) - U_i^{(1)}(\mathbf{x_T} - \mathbf{e_i})\right) - \mathrm{h.c.}\Big]\end{aligned} \tag{3.22}$$

which gives the initial condition for the longitudinal electric field. The subscript i denotes the two transverse directions while the superscript (j) (with $j = 1, 2, 3$) denotes the link matrices corresponding to region (j) in the left panel of Fig. 3.1. The gauge fields of the two nuclei are given by:

$$U_i^{(m)}(\mathbf{x_T}) = e^{i\Lambda_{(m)}(\mathbf{x_T})} e^{-i\Lambda_{(m)}(\mathbf{x_T} + \mathbf{e_i})} \tag{3.23}$$

with $\boldsymbol{\nabla}^{\mathbf{2}}_{\mathbf{T}}\Lambda_{(m)} = -g\rho_{(m)}$ for $m = 1, 2$ and $\rho_{(m)}$ the color charge density of the two nuclei.

The initial conditions on the lattice pose a problem due to the non-linear set of equations given in Eq. (3.21). The non-linear requirement arises since $U_i^{(3)}$ must be an element of the $SU(3)$ group. We propose an iterative method for solving such a system of equations, method which is presented in details in Sec. 3.2. Our method is much faster than typical simulated annealing methods that were used until now.

Now it is straightforward to discretize Eqs. (3.16)-(3.20) for example using the leapfrog algorithm[1]. This algorithm is especially useful in Hamiltonian time evolution since it makes the algorithm time reversal invariant and also second order accurate in time.

[1]In the leapfrog algorithm the momenta and coordinates are known at different time steps. So if the coordinates are know at τ and $\tau + a_\tau$, than the momenta are known at $\tau - a_\tau/2$ and $\tau + a_\tau/2$.

3.2 Solving the initial condition for the gluonic field

The initial condition for the numerical simulation of the $SU(N)$ gluonic field involves solving Eq. (3.21). For the $SU(2)$ case, this equation can be solved analytically [25]. But for a larger number of colors ($N \geq 3$), solving the non-linear[1] system of equations can be a challenging and time intensive task. In this section we present an iterative method developed by us to solve Eq. (3.21). We restrict our analysis to the particular case of $SU(3)$, but the algorithm for solving Eq. (3.21) can be applied to any $SU(N)$ group.

Solving Eq. (3.21) for the $SU(3)$ case cannot be done analytically since it involves a set of nonlinear equations, so an iterative method must be used. In the following, for simplicity of notation, we drop from Eq. (3.21) the subscript i which denotes the transverse direction. The first step of the algorithm it involves to take a good initial guess for the link matrix $U^{(3)}$. We take as initial guess:

$$U^{(3)} = U^{(1)}U^{(2)}, \tag{3.24}$$

which is the solution of Eq. (3.21) for the abelian case. Inserting the guess in Eq. (3.21) results in:

$$\text{Re Tr}\left[t_a(U^{(1)} + U^{(2)})(1 + U^{\dagger(3)})\right] = f_a \tag{3.25}$$

where f_a is a set of real numbers. Since $U^{(3)}$ is an element of $SU(3)$, the solution of Eq. (3.21) is given by:

$$U^{(3)}_{new} = e^{ix_a t_a} U^{(3)}_{old} \tag{3.26}$$

where $U^{(3)}_{old}$ is the guess which satisfies Eq. (3.25). Using only the first two terms in the Taylor expansion of the exponential in Eq. (3.26) and imposing the condition that $U^{(3)}_{new}$ satisfies Eq. (3.21), we obtain:

$$x_b \text{ Im Tr}\left[t_b t_a (U^{(1)} + U^{(2)}) U^{\dagger(3)}_{old}\right] = -f_a. \tag{3.27}$$

[1]The non-linearity of Eq. (3.21) arises from the requirement that the link matrix $U^{(3)}$ are elements of the $SU(N)$ group.

This linear system of equations can be easily solved for x_b, which means that we can find $U^{(3)}_{new}$. Since $U^{(3)}_{new}$ is an element of $SU(3)$, to compute it from $U^{(3)}_{old}$ we must use Eq. (3.26) without any approximations for the exponential. Hence now we have:

$$\text{Re Tr}\left[t^a(U^{(1)}+U^{(2)})(1+U^{\dagger(3)}_{new})\right] = f'_a. \tag{3.28}$$

A simpler expression for f'_a can be found using the Taylor expansion for the exponential in Eq. (3.26). The first non-zero term reads:

$$f'_a = -\frac{1}{2}x_b x_c \text{ Re Tr}\left[t_b t_c t_a (U^{(1)}+U^{(2)})U^{\dagger(3)}_{old}\right]. \tag{3.29}$$

Close to the continuum limit, the Wilson lines can be approximated to unit matrices. So in the continuum limit Eq. (3.27) reduces to $x_a = -f_a$ and hence Eq. (3.29) can be simplified to read:

$$f'_a = -\frac{1}{4}f_b f_c d_{abc}. \tag{3.30}$$

If the initial guess was a good one, than f_a should be small, in which case $|f'_a| < |f_a|$. So by iterating the above process, one can get a converging algorithm for finding the solution of Eq. (3.21). Even though Eq. (3.30) was obtained in the continuum limit, it can be used to draw more general conclusions. We expect f'_a to be roughly proportional to $f_b f_c$ also in the general case, even though the exact dependence will be more complicated. This means that for good initial guesses (small f_a) we expect that $|f'_a| < |f_a|$ and hence the algorithm described above will converge.

We tested the above algorithm as well as an improved version of it for different lattice sizes as well as for different values of the color charge density μ[1]. The improved version of the algorithm is especially efficient away from the continuum limit when the initial guess given by Eq. (3.24) is not a very good one. The improved method supposes that by solving Eq. (3.27) we get the right direction in which to move in

[1]Both the transverse lattice size N^2 and the parameter μ characterize how close the lattice fields are to the continuum limit. For the same value of μ, a larger transverse lattice means closer to the continuum limit. On the other hand, for the same lattice size, bigger μ means further away from the continuum limit.

order to get f_a closer to zero, but that the size of the move is not the correct one. Hence we take the solutions of Eq. (3.27) and before inserting them into Eq. (3.26), we multiply them by a constant factor α such that the new value for the Wilson line is given by:

$$U^{(3)}_{new} = e^{i\alpha x_a t_a} U^{(3)}_{old}. \tag{3.31}$$

When the new value of the Wilson line is close to the desired solution (i.e. small f_a) than we take $\alpha = 1$, which results in the initial algorithm.

Since we cannot be certain that our algorithm will always converge, we supplemented the above method with a simulated annealing method (SAM) for finding a better initial guess for $U^{(3)}$. We call the SAM when we do not get convergence after a certain number of steps using the above algorithm (this number of steps is small, of the order 10-50[1]).

	$\mu = 0.5$ GeV			$\mu = 2$ GeV		
N^2	SAM* (%)	calls†	time‡ (μs)	SAM* (%)	calls†	time‡ (μs)
32^2	7 ± 1	7.3 ± 0.3	5.9	19 ± 1	10.7 ± 0.2	13.2
64^2	0.04 ± 0.02	4.26 ± 0.04	1.3	15.7 ± 0.6	10.0 ± 0.1	10.7
128^2	0	3.43 ± 0.02	0.73	8.4 ± 0.4	7.83 ± 0.09	6.7
256^2	0	3.00 ± 0.01	0.64	0.20 ± 0.03	4.32 ± 0.02	1.5

Table 3.1: The results of using the basic method (not the improved one) in iteratively solving Eq. (3.21) for different values of μ ($g = 2$). * The average number of times the simulated annealing method (SAM) was called for each lattice point. † The average number of iterations of the basic method for each lattice point. ‡ The average computational time for each lattice point. (All the errors are systematic errors from simulations over 20 different random configurations of initial charge density.)

Table 3.1 shows that the basic method described above (the one with the $\alpha = 1$) gives a convergent algorithm for most of the lattice points. In the continuum limit (small μ and large N^2) the algorithm is converging very fast, on average needing only

[1]We use several criteria for deciding if convergence will be reached depending how big $\sum_a |f_a|$ is during a given iteration. These criteria have no impact on the convergence speed but only on the computational time.

3 iterations to get to $\sum_a |f_a| < 10^{-13}$ (which is the numerical test when we consider that Eq. (3.21) is satisfied). But the further away the Wilson lines are from the continuum expressions, the higher is the number of cases in which the method does not converge. This was expected since there is no reason why the analysis presented in this section will hold for any distribution of the gluonic field.

	$\mu = 2$ GeV		$\mu = 5$ GeV		$\mu = 20$ GeV	
N^2	SAM* (%)	time† (μs)	SAM* (%)	time† (μs)	SAM* (%)	time† (μs)
32^2	1.6 ± 0.4	2.8	2.5 ± 0.4	3.4	2.4 ± 0.4	3.4
64^2	1.3 ± 0.1	2.5	2.2 ± 0.3	3.2	2.1 ± 0.2	3.2
128^2	0.84 ± 0.05	2.0	2.07 ± 0.08	3.2	2.0 ± 0.1	3.2

Table 3.2: The results of using the improved method in iteratively solving Eq. (3.21) for different values of μ ($g = 2$). The results presented here are obtained for $\alpha = 0.5$. On average, there are 10 calls of the iterative method for each lattice point. * The average number of times the simulated annealing method (SAM) was called for each lattice point. † The average computational time for each lattice point. (All the errors are systematic errors from simulations over 20 different random configurations of initial charge density.)

We also studied the convergence speed of the improved algorithm for different values of the α parameter. We found that as α decreases the number of times the SAM is called also decreases, which decreases very much the computational time. But the downside of a small α is an increase in the number of iterations of the method, which can also have the effect of an increased computational time. The smallest computational time is obtained for α in the range 0.4 to 0.6[1].

As can be seen from Table 3.2, the improved method does not totally cancel the need to use the SAM, but it does reduce significantly the number of times the SAM is called. This decreases the computational time by almost an order of magnitude, depending on the lattice size and the value of μ. Moreover, as the Wilson lines are even further apart from their continuum limit, the improved method behaves as well,

[1]The difference in computational time between two values of α in the interval 0.4 to 0.6 are at most 5%. As the Wilson lines go further away from their continuum limit, the value of α corresponding to the fastest convergence slightly decreases (but still remains in the interval 0.4 to 0.6 and any differences in computational time still remain small).

as it can be seen for $\mu = 5$ GeV and $\mu = 20$ GeV. The computational times given in Tables 3.1 and 3.2 can be decreased even further by at least a factor of 2[1].

The iterative method described in this section can be summarize in the following steps:

1. Start with the initial guess $U^{(3)} = U^{(1)}U^{(2)}$.

2. Solve the linear system from Eq. (3.27).

3. Use Eq. (3.31) to update the new value of $U^{(3)}$ with $\alpha = 0.5$ if $\sum_a |f_a| > 0.5$ [2] or with $\alpha = 1$ otherwise.

4. Check to see if Eq. (3.21) is satisfied, if not continue from step 2. If steps 2 to 3 were already executed several times (around 20 to 40) and Eq. (3.21) is not satisfied, switch to the SAM.

5. In SAM take the temperature proportional to $\sum_a |f_a|$ and lower it until $\sum_a |f_a| < 0.5$ [3], such that for each temperature there are enough steps to achieve a good

[1] After these tests were performed, the computational time of the iterative method was decreased by a factor of 2. This results in a halving of the times in Table 3.1 for $\mu = 0.5$ GeV and around a 1.5 times decrease for the times in Table 3.2. Even smaller computational times can be achieved by loose of flexibility in the code (like hard coding for a specific form of the t_a matrices), but this was not implemented since this part of the numerical simulation takes much less than 1% of the typical running time for the gauge field evolution code.

[2] We choose $\sum_a |f_a| = 0.5$ as the boundary when changing between $\alpha = 0.5$ and $\alpha = 1$ since it optimizes the computational time. Smaller values for $\sum_a |f_a|$ will decrease the number of calls to SAM, but will also increase the overall number of iterative steps for each lattice point. Since there are only a small percentage of calls to SAM, the overall computational time will increase for a smaller value of $\sum_a |f_a|$.

[3] Here again we choose the stop condition as $\sum_a |f_a| = 0.5$ since tests showed that for most of the lattice points this is enough to assure convergence of the iterative method. For most of the lattice points where the code calls the SAM method, it calls it just once; only very rarely it is called more than once for a lattice point. In our numerical implementation, this section of the code was written and tested before implementing the improved method (with $\alpha < 1$), so probably there is even more room for improvement by increasing the value of $\sum_a |f_a|$.

sweep (around 200-300 points are more than enough, but also depends on how fast the temperature is lowered). When $\sum_a |f_a| < 0.5$ switch to step 2.

3.3 Quark pair production

In this section we describe the formalism presented in [26]. The numerical formalism was tested in [26] for the case of only one spatial dimension and then the results were extended to the full three dimensional space in [29, 30, 31]. Compared to gluon calculations, the time evolution of the Dirac wavefunction is more complicated because the quark wavefunction depends on three spatial dimensions and also because the Dirac equation has to be discretized using an implicitly scheme.

3.3.1 General formulation

The average number of quark pairs produced in the collision of two nuclei can be expressed as [23]:

$$\langle n_{q\bar{q}} \rangle = \int \frac{d^3\mathbf{p}}{(2\pi)^3 2E_p} \langle 0_{in} \left| b^\dagger_{out}(\mathbf{p}) b_{out}(\mathbf{p}) \right| 0_{in} \rangle \tag{3.32}$$

$$= \int \frac{d^3\mathbf{p}}{(2\pi)^3 2E_p} \frac{d^3\mathbf{q}}{(2\pi)^3 2E_q} \left| \bar{u}(p) T_R(p,-q) v(q) \right|^2 \tag{3.33}$$

where $T_R(p,-q)$ is the amputated retarded propagator of a quark in an external field with incoming momentum $-q$ and outgoing momentum p. $E_{p,q}$ represents the energy associated to an on shell particle with 3-momentum $\mathbf{p}$ and $\mathbf{q}$ respectively. $u(p)$ and $v(q)$ are Dirac spinors for the plane wave solution of the free Dirac equation. In [26] was shown that one can use the following identity:

$$\bar{u}(p) T_R(p,-q) v(q) = \lim_{t \to +\infty} \int d^3\mathbf{x} e^{i(E_p t - \mathbf{p}\cdot\mathbf{x})} \bar{u}(p) \gamma^0 \Psi_q(t,\mathbf{x}) \tag{3.34}$$

where $\Psi_q(t,\mathbf{x})$ represents the solution of the Dirac equation with initial condition given by:

$$\lim_{t \to -\infty} \Psi_q(t,\mathbf{x}) = e^{iqx} v(q) \tag{3.35}$$

which is just the plane wave solution for a free antiquark. Eq. (3.34) can be trivially modified to describe the multiplicity for a given time t by removing the limit $t \to +\infty$

and evaluating Eq. (3.34) at a fixed time t. This would give a time dependent number of pairs[1]. Since in heavy ion collision the important time parameter is the proper time, one can write Eq. (3.34) using space-time rapidity and proper time coordinates as:

$$\bar{u}(p)T_R(p,-q)v(q)|_\tau = \tau \int d^2\mathbf{x_T} d\eta \; e^{-i\mathbf{p_T}\cdot\mathbf{x_T}} e^{im_T\tau\cosh(y-\eta)} \bar{u}(p)\gamma^\tau \Psi_q(\tau,\eta,\mathbf{x_T}) \quad (3.36)$$

where y is the rapidity of the final state quark and $\eta = \frac{1}{2}\ln\left(\frac{t+z}{t-z}\right)$ is the space-time rapidity. Eq. (3.36) holds since the limit $t \to \infty$ is the same as the limit $\tau \to \infty$, since $t = \tau\cosh(\eta)$. This is true for all values of η with the exception of $\eta \to \pm\infty$. But the contribution to the integral in Eq. (3.36) from large η is 0 due to the very fast oscillation of the exponential which depends on $\cosh(y-\eta)$.

Eq. (3.36) tells us that to find the number of produced quarks at proper time τ one must start with the free antiquark at infinite past. After evolving the antiquark wavefunction to τ, one must take the superposition of the antiquark wavefunction with that of a free quark. This gives the number of produced quarks at a given momentum, but since quarks are produced only in quark-antiquark pairs, it also gives the number of produced pairs. Eq. (3.33) tells us that to get the total number of quark pairs produced in the collision, one must sum over all the possible momenta of the final quark and that of the incoming antiquark.

Now the next logical step is to compute $\Psi_q(\tau,\eta,\mathbf{x_T})$. This can be done analytically up to $\tau = 0$ since the gluonic fields within the CGC approach are known analytically up to $\tau = 0$ [26, 37]. For $\tau > 0$, the Dirac field must be computed numerically since the gauge fields are also evolved in time using a numerical algorithm. The computation of the initial condition for the Dirac field (i.e. $\Psi_q(\tau = 0,\eta,\mathbf{x_T})$) was done in [26, 37]. In [37] $\Psi_q(\tau,\eta,\mathbf{x_T})$ given by Eq. (3.35) was computed for the Abelian case in both the covariant gauge and in the light-cone gauge. In the Abelian case, the gauge and Dirac fields can be computed analytically for all times. In [26] $\Psi_q(\tau = 0,\eta,\mathbf{x_T})$ is again computed analytically within the light-cone gauge (and Coulomb gauge[2] for

[1]It merits further study if one can simply remove the $t \to +\infty$ limit from Eq. (3.34) and still keep the form of the equation intact [31].

[2]The Coulomb gauge for the transverse direction is given by $\partial_i A_i(\mathbf{x_T}) = 0$ with $i = 1, 2$.

the transverse direction) for the Abelian case and than generalized for the $SU(N)$ case. The main difference between Abelian and the non-Abelian theories is that in the former the gauge fields and Wilson lines commute, so multiplication order is not important. But for the non-Abelian theories the ordering of the fields is important, since matrix multiplication is noncomutative. The Abelian result was generalized to the non-Abelian theory by writing it in a compact form that contains only products of identical Wilson lines which automatically commute.

The computation of the initial condition for the quark wavefunction can be done using the retarded quark propagator in the field of the two nuclei (propagator which can be found in [23]) or using some clever guesses for the general form of the quark wavefunction (as was done in [37]). The calculation consists of propagating the fermion on each of the two paths shown in the right panel of Fig. 3.1, after which both contributions must be summed. The only nontrivial calculations are at crossing the light cone axes. One must pay attention to the discontinuities in the Dirac wavefunction that arise due to discontinuities in the gauge fields when crossing the light cone. For example, on the x^- axis the gauge field $A_- = 0$ but A_+ will have a $\theta(x^-)$ discontinuity. Since the Dirac equation in LC coordinates will have terms of the form $\partial_-\gamma^+$ and $\partial_+\gamma^-$ [1], at $x^- = 0$, $\gamma^+\Psi$ is continuous while $\gamma^-\Psi$ is not[2]. Using that $\gamma^\pm P^\mp = 0$, the continuity requirement for $\gamma^+\Psi$ reduces to a continuity requirement for $P^+\Psi$. Similarly, for the $x^+ = 0$ axis we must have that $P^-\Psi$ is continuous.

Another challenge with finding the $\Psi_q(\tau = 0, \eta, \mathbf{x_T})$ is that for $\tau = 0$ there is no dimensionful longitudinal variable. Normally, for $\tau \neq 0$ one uses $\tau e^{\pm\eta}$, but for $\tau = 0$ this does not work. To overcome this problem, and to have a symmetric treatment in $x^\pm$, one takes the longitudinal variable as z. By performing the calculations described above, after rather a few mathematically involved steps, we find that the wavefunction

[1] The LC coordinate Dirac matrices are defined as $\gamma^\pm = \frac{1}{\sqrt{2}}(\gamma^0 \pm \gamma^3)$. With $P^\pm = \frac{1}{2}(1 \pm \gamma^0\gamma^3)$ we denote two projection operators. See Appendix A.2 for properties of the projection operators as well as for additional details about the LC coordinates.

[2] If $\gamma^+\Psi$ would be discontinuous, than the term $\partial_-\gamma^+\Psi$ gives a delta function. Since there is no discontinuity in A_- to compensate for the delta function, such a discontinuity in $\gamma^+\Psi$ is forbidden.

at $\tau = 0$ is [26]:

$$\begin{aligned}
\Psi(\tau = 0, z, \mathbf{x_T}) = & \int \frac{d^2\mathbf{k_T}}{(2\pi)^2} \\
& \times \left\{ P^+ \frac{e^{y_q}}{\omega_q} U_{(1)}(\mathbf{x_T}) U^\dagger_{(1)}(\mathbf{k_T}) \ \exp\left(i \frac{\omega^2_{k+q} e^{y_q}(|z| - z)}{2\omega_q} \right) \right. \\
& + P^- \gamma^0 [i\gamma_\mathbf{T} \cdot \mathbf{D_T} - m] U_{(1)}(\mathbf{x_T}) U^\dagger_{(1)}(\mathbf{k_T}) \frac{1}{\omega^2_{k+q}} \left[\exp\left(i \frac{\omega^2_{k+q} e^{y_q}(|z| - z)}{2\omega_q} \right) - 1 \right] \\
& + P^- \frac{e^{-y_q}}{\omega_q} U_{(2)}(\mathbf{x_T}) U^\dagger_{(2)}(\mathbf{k_T}) \ \exp\left(i \frac{\omega^2_{k+q} e^{-y_q}(|z| + z)}{2\omega_q} \right) \\
& \left. + P^+ \gamma^0 [i\gamma_\mathbf{T} \cdot \mathbf{D_T} - m] U_{(2)}(\mathbf{x_T}) U^\dagger_{(2)}(\mathbf{k_T}) \frac{1}{\omega^2_{k+q}} \left[\exp\left(i \frac{\omega^2_{k+q} e^{-y_q}(|z| + z)}{2\omega_q} \right) - 1 \right] \right\} \\
& \times e^{-i(\mathbf{k_T} + \mathbf{q_T}) \cdot \mathbf{x_T}} \ \gamma^0 \left[\gamma_\mathbf{T} \cdot (\mathbf{k_T} + \mathbf{q_T}) - m \right] v(q)
\end{aligned} \tag{3.37}$$

where $U_{(1),(2)}(\mathbf{x_T})$ and $U^\dagger_{(1),(2)}(\mathbf{k_T})$ are the Wilson lines of the two nuclei and respectively their Fourier transforms defined as:

$$U^\dagger_{(j)}(\mathbf{k_T}) = \int d^2\mathbf{x_T} \ e^{i\mathbf{k_T} \cdot \mathbf{x_T}} U^\dagger_{(j)}(\mathbf{x_T}) \tag{3.38}$$

with $j = 1, 2$. $\mathbf{D_T}$ are the transverse covariant derivatives while $\omega^2_{k+q} = (\mathbf{k_T} + \mathbf{q_T})^2 + m^2$, with m the mass of the initial antiquark. The above result was obtained for QED, but because it contains only products of the same kind of Wilson lines, it also holds for QCD [26].

Using that for $\tau = 0$ $x^\pm = \frac{1}{\sqrt{2}}(|z| \pm z)$, we can immediately see that lines 2 and 3 of Eq. (3.37) depend only on x^- while lines 4 and 5 depend only on x^+. This suggests that lines 2 and 3 resulted from the propagation of the antiquark trough the field of the colliding nuclei on the left path shown in the right panel in Fig. 3.1, while lines 4 and 5 resulted due to the antiquark propagation on the right path shown in the right panel in Fig. 3.1. The resulting wavefunction is the sum of the two contributions.

If the initial wavefunction would be that of a free quark:

$$\lim_{t \to -\infty} \Psi_q(t, \mathbf{x}) = e^{-iqx} u(q) \tag{3.39}$$

and not antiquark (see Eq. (3.35)), than the corresponding initial condition for $\tau = 0$ is very similar to the one given in Eq. (3.37). The only difference comes from replacing

q with $-q$ and $v(q)$ with $u(q)$. In fact, when deriving Eq. (3.37), the only time where the fact that the spinor was corresponding to a antiquark and not a quark was used explicitly was in the relation $(\not{q}+m)v(q) = 0$. But by taking $q \to -q$ and $v(q) \to u(q)$, the above relation would read $(-\not{q}+m)u(q) = 0$, which holds true for any q. Hence Eq. (3.37) holds also for quarks in the initial state with the appropriate substitutions.

3.3.2 Dirac equation in curvilinear coordinates

Starting from the initial condition in Eq. (3.37), one must solve the Dirac equation in the coordinate $(\tau = \sqrt{t^2 - z^2}, z, \mathbf{x_T})$. The easiest way to do so is to transform the coordinates while keeping the fields unchanged [26]. A coordinate transformation from $(t, z, \mathbf{x_T})$ to $(\tau, z, \mathbf{x_T})$ (for details about coordinate transformations see Appendix A.1) acts on the derivatives according to:

$$\partial_t \to \frac{\sqrt{\tau^2 + z^2}}{\tau}\partial_\tau \tag{3.40}$$

$$\partial_z \to \frac{z}{\tau}\partial_\tau + \partial_z \tag{3.41}$$

with the rest of the derivatives remaining unchanged. Exactly the same transformation rules apply to the gauge fields A_μ. Inserting the above into the Dirac equation given in Eq. (2.8) yields:

$$i\gamma^\tau D_\tau \Psi = \left[-i\gamma^3 D_z + (-i\gamma_\mathbf{T} \cdot \mathbf{D_T} + m)\right] \Psi \tag{3.42}$$

where we used the notation:

$$\gamma^\tau = \frac{\sqrt{\tau^2 + z^2}}{\tau}\gamma^0 - \frac{z}{\tau}\gamma^3. \tag{3.43}$$

By multiplying Eq. (3.42) with $-iP^\pm\gamma^0$ we get[1]:

$$\left(\frac{\sqrt{\tau^2 + z^2}}{\tau} - \frac{z}{\tau}\gamma^0\gamma^3\right) D_\tau \Psi^\pm = -\gamma^0\gamma^3 D_z \Psi^\pm + i\gamma^0(i\gamma_\mathbf{T} \cdot \mathbf{D_T} - m)\Psi^\mp \tag{3.44}$$

where for simplicity we used the notation $\Psi^\pm = P^\pm\Psi$. Now using that $\gamma^0\gamma^3 P^\pm = \pm P^\pm$, we finally obtain:

$$D_\tau \Psi^\pm = \frac{\sqrt{\tau^2 + z^2} \pm z}{\tau}[\mp D_z \Psi^\pm + i\gamma^0(i\gamma_\mathbf{T} \cdot \mathbf{D_T} - m)\Psi^\mp] \tag{3.45}$$

[1] After using that $P^\pm\gamma^0\gamma^3 = \gamma^0\gamma^3 P^\pm$, $P^\pm\gamma^0 = \gamma^0 P^\mp$ and $P^\pm\gamma^0\gamma^i = \gamma^0\gamma^i P^\mp$ (with $i = 1, 2$)

Now we still have to specialize Eq. (3.45) to the temporal gauge used in the gluon evolution part (i.e. A_τ=0). Since the gluonic fields are computed in the $(\tau, \eta = \frac{1}{2}\ln\left(\frac{\sqrt{\tau^2+z^2}+z}{\sqrt{\tau^2+z^2}-z}\right), \mathbf{x_T})$ coordinate, we still have to transform the gluonic fields to the $(\tau, z, \mathbf{x_T})$ coordinate. Using the rules from Appendix A.1 we obtain:

$$\begin{aligned} A'_\tau &= A_\tau - \frac{z}{\tau\sqrt{\tau^2+z^2}}A_\eta \\ A'_z &= \frac{1}{\sqrt{\tau^2+z^2}}A_\eta \end{aligned} \tag{3.46}$$

with A' and A the vector fields in $(\tau, z, \mathbf{x_T})$ and $(\tau, \eta, \mathbf{x_T})$ coordinates respectively. The transverse fields are the same in both coordinates. Putting everything together, we get:

$$\partial_\tau \Psi^\pm = \frac{\sqrt{\tau^2+z^2} \pm z}{\tau}\left[\mp\partial_z\Psi^\pm + i\gamma^0(i\gamma_\mathbf{T}\cdot\mathbf{D_T} - m)\Psi^\mp\right] \mp i\frac{\Phi}{\tau}\Psi^\pm \tag{3.47}$$

where we used the notation $\Phi = gA_\eta$[1] and also set $A_\tau = 0$ (the temporal gauge condition).

Now we have all the ingredients necessary to be able to compute the quark production within the CGC and MV models. But before doing so, we have to carefully analyze several problems that may arise due to explicit coordinate dependence of the terms in Eq. (3.47). The first is the $1/\tau$ term which can create problems in the limit $\tau \to 0$, especially in a numerical simulation. Let us start by checking that the initial condition from Eq. (3.37) is indeed a solution of the Dirac equation at $\tau = 0$. For $z < 0$ and $\tau \to 0$, Eq. (3.47) reduces to:

$$\partial_\tau \Psi^- = \frac{-2z}{\tau}\left[\partial_z\Psi^- + i\gamma^0(i\gamma_\mathbf{T}\cdot\mathbf{D_T} - m)\Psi^+\right] \tag{3.48}$$

since we also have the initial condition $\Phi|_{\tau=0} = 0$. For $z < 0$, Ψ^- will be given by rows 3 and 4 of Eq. (3.37) (but only row 3 has a z dependence) while Ψ^+ will be given only by row 2. It is straightforward to check that the terms inside the square brackets of Eq. (3.48) do cancel. Hence for $z < 0$ and $\tau \to 0$, Eq. (3.47) does not have any singularities as might have naively been suggested by the $1/\tau$ term. Similarly it can be shown that also for $z > 0$ the $1/\tau$ term does not create problems.

[1]The Φ field from Eq. (3.47) is related to the scalar longitudinal field ϕ defined in Sec. 3.1 via the equation $\Phi = g\phi$.

3.3.3 Quark production in 1+1 dimensions

It is also instructive to look at the case of one spatial dimension since it provides an easy and fast way to check the numerical behavior of the Dirac equation. Before doing so, let us see how some of the expressions for the full 3+1 case presented above simplify for just one spatial dimension. In this case, the number of produced pairs reduces to:

$$\frac{\langle n_{q\bar{q}}\rangle}{dy} = \int d(y-y')|M_\tau(y-y')|^2 \tag{3.49}$$

$$M_\tau(y-y') = \tau \int d\eta\ \bar{u}(y')e^{im\tau\cosh(\eta-y')}\gamma^\tau\Psi(\tau,z) \tag{3.50}$$

where M_τ represents the amplitude to produce quark pairs at a given time τ. With y and y' we denote the rapidity of the initial antiquark and final quark respectively. Eqs. (3.49)-(3.50) exploit that the background gauge field is boost invariant. Thus the amplitude for quark production depends only on the rapidity difference between the initial state antiquark and final state quark, and not on the individual rapidities of the initial and final state particles.

The initial conditions for the 1+1 dimensional case are found using Eq. (3.37) specified for just one spatial dimension. To do so, one must first remove the dependence on the transverse coordinates by specializing to a 0 transverse gauge field (i.e. $U_{(i)}(\mathbf{x_T}) = 1$ and $U_{(i)}(\mathbf{k_T}) = (2\pi)^2\delta^2(\mathbf{k_T})$). This gives:

$$\Psi(\tau=0,z,\mathbf{x_T}) = e^{-i\mathbf{q_T}\cdot\mathbf{x_T}}\left(e^{iq^+x^-} + e^{iq^-x^+} - 1\right)v(q) \tag{3.51}$$

where $q^\pm = \frac{\omega_q e^{\pm y}}{\sqrt{2}}$ are the LC momenta and $x^\pm$ are the LC coordinates at $\tau = 0$. The next step is to drop the transverse coordinate. It is convenient to split the initial condition in two branches, which we will call left and right. Each branch corresponds to the solution one obtains by propagating the initial free wave from $t \to -\infty$ to $\tau = 0$ by the two possible ways illustrated in the right panel of Fig. 3.1. The initial condition for the left branch is:

$$\begin{aligned}\Psi^+(\tau=0,z) &= -e^{y/2}\sqrt{m}\exp\left(i\frac{me^y}{2}(|z|-z)\right)\\ \Psi^-(\tau=0,z) &= e^{-y/2}\sqrt{m}\left[\exp\left(i\frac{me^y}{2}(|z|-z)\right)-1\right]\end{aligned} \tag{3.52}$$

whereas for the right branch the initial condition reads:

$$\Psi^+(\tau=0,z) = e^{y/2}\sqrt{m}\left[1-\exp\left(i\frac{me^{-y}}{2}(|z|+z)\right)\right]$$
$$\Psi^-(\tau=0,z) = e^{-y/2}\sqrt{m}\exp\left(i\frac{me^{-y}}{2}(|z|+z)\right). \tag{3.53}$$

In the above equations we already used the fact that for 1+1 dimensions the Dirac spinor v is given by:

$$v(y) = \sqrt{m}\begin{pmatrix} e^{y/2} \\ -e^{-y/2}\end{pmatrix} \tag{3.54}$$

Ref. [26] shows that in the absence of an external field, the two paths shown in the right panel in Fig. 3.1, individually give rise to the following amplitude for quark production:

$$|M| = \frac{1}{\cosh\left(\frac{y-y'}{2}\right)} \tag{3.55}$$

while when considered together, the amplitude is 0 as expected in the absence of an external field. A similar relation holds also for the 3 dimensional free Dirac equation, with the difference that we also have to integrate over the transverse momenta of the final state quark.

3.4 The discretized Dirac equation

3.4.1 Discretizing the Dirac equation

In the (τ, x, y, z) coordinate system the Dirac equation can be discretized using a second order method for both the τ and z directions. For the z direction, due to the explicit dependence of the analytical equations on the z position, an explicit discretization scheme is unstable, this is why the z derivative has to be discretized implicitly. The τ derivative of the Dirac field is discretized according to:

$$\partial_\tau\Psi(\tau,z) \to \frac{1}{2a_\tau}\left[\Psi(\tau+a_\tau,z)-\Psi(\tau-a_\tau,z)\right] \tag{3.56}$$

while for the z derivative we start by writing the derivative at τ as the average of the z derivative at $\tau-a_\tau$ and $\tau+a_\tau$

$$\partial_z\Psi(\tau,z) \approx \frac{1}{2}\left[\partial_z\Psi(\tau-a_\tau,z)+\partial_z\Psi(\tau+a_\tau,z)\right], \tag{3.57}$$

after which each of the two right hand side terms is discretized to:

$$\partial_z \Psi(\tau, z) \rightarrow \frac{1}{2a_z} \left[\Psi(\tau, z + a_z) - \Psi(\tau, z - a_z)\right]. \tag{3.58}$$

In the above equations, all the Ψ variables are to be evaluated on the transverse plane at the $\mathbf{x_T}$ coordinate (this notation was dropped for more readability). The constants a_τ and a_z denote the lattice spacing in the τ and z direction respectively. Moreover, it also makes sense to use the following relation (the advantages of using it will be clearer later):

$$\frac{\Phi(\tau)}{\tau}\Psi(\tau, z) \approx \frac{\Phi(\tau)}{2\tau} \left[\Psi(\tau - a_\tau, z) + \Psi(\tau + a_\tau, z)\right]. \tag{3.59}$$

The transverse covariant derivative along the i-th transverse direction is discretized as:

$$D_i \Psi(\mathbf{x_T}) \rightarrow \frac{U_i(\mathbf{x_T})\Psi(\mathbf{x_T} + \mathbf{e_i}) - U_i^\dagger(\mathbf{x_T} - \mathbf{e_i})\Psi(\mathbf{x_T} - \mathbf{e_i})}{2a_i} \tag{3.60}$$

where $U_i(\mathbf{x_T})$ (with $i = 1, 2$) denotes the link matrices along the i-th direction in the transverse plane. The constant a_i denotes the lattice spacing along the i-th transverse direction. The coordinate $\mathbf{x_T} + \mathbf{e_i}$ denotes the next neighbor in the i-th transverse direction for lattice point $\mathbf{x_T}$. The τ and z dependence of Ψ in the upper expression was dropped for readability, but all the Ψ fields have to be evaluated at the same τ, z point. In the following we use $\mathbf{D_T}\Psi$ to denote the transverse gradient of the Dirac field ($\mathbf{D_T}\Psi$ is the sum of Eq. (3.60) for $i = 1$ and $i = 2$ which correspond to the x and y directions).

Now all the previous expressions can be inserted into Eq. (3.47) to give:

$$\begin{aligned}\frac{1}{2a_\tau}(\Psi_{n+1}^{\pm;j} - \Psi_{n-1}^{\pm;j}) = \mp\frac{\sqrt{\tau^2 + z^2} \pm z}{4\tau a_z} \left(\Psi_{n+1}^{\pm;j+1} - \Psi_{n+1}^{\pm;j-1} + \Psi_{n-1}^{\pm;j+1} - \Psi_{n-1}^{\pm;j-1}\right) \\ + \frac{\sqrt{\tau^2 + z^2} \pm z}{\tau} a_\tau \, i\gamma^0(i\gamma_\mathbf{T} \cdot \mathbf{D_T} - m)\Psi_n^{\mp;j} \mp i\frac{\Phi_n}{2\tau}\left(\Psi_{n+1}^{\pm;j} + \Psi_{n-1}^{\pm;j}\right)\end{aligned} \tag{3.61}$$

where n denotes the τ step and j the lattice point in the z direction. All the Ψ fields in the above equation are to be evaluated at the same transverse lattice point $\mathbf{x_T}$.

Eq. (3.61) gives rise to the following system of linear equations:

$$(1 \pm i\frac{\Phi_n a_\tau}{\tau})\Psi_{n+1}^{\pm;j} \pm \frac{\sqrt{\tau^2+z^2} \pm z}{2a_z\tau} a_\tau(\Psi_{n+1}^{\pm;j+1} - \Psi_{n+1}^{\pm;j-1}) = (1 \mp i\frac{\Phi_n a_\tau}{\tau})\Psi_{n-1}^{\pm;j} \mp \frac{\sqrt{\tau^2+z^2} \pm z}{2a_z\tau} a_\tau(\Psi_{n-1}^{\pm;j+1} - \Psi_{n-1}^{\pm;j-1}) + \frac{\sqrt{\tau^2+z^2} \pm z}{\tau} 2a_\tau \; i\gamma^0(i\gamma_{\mathbf{T}} \cdot \mathbf{D_T} - m)\Psi_n^{\mp;j} \tag{3.62}$$

where the unknowns are the Ψ_{n+1} fields isolated on the left hand side. In Eq. (3.62) the Ψ^+ and Ψ^- fields need to be known only at different time steps, hence to minimize memory one can store one field component (lets say Ψ^+) at even τ steps and the other one (Ψ^-) at odd τ steps. And then, after solving the linear system in Eq. (3.62), it can store the values of the Dirac field at the new $n+1$ time step in the same memory location where it stored the values at the $n-1$ time step. So by using the approximation from Eq. (3.59) one needs to store only one copy of the field Ψ and not two copies as one would have expected by using a second order accurate discretization scheme.

Periodic boundary conditions can be used for the transverse directions, but not for the longitudinal one since the Dirac equation is not translation invariant. This is why free boundary conditions must be used for the z directions. It is also very important to replace the z derivative with a second order accurate discretized version for the lattice points at the end of the z direction. Otherwise one will have instabilities which start at these lattice points and propagate into all the lattice points. Even a second order accurate method does not fully solve this problem, but it takes much longer for theses instabilities to rise. The τ value after which these instabilities become important is much larger than the τ to which the code has to be evolved to study HIC. So for the end points of the z lattice one has:

$$\partial_z \Psi^{-J} \to \frac{1}{2a_z}\left[-3\Psi^{-J} + 4\Psi^{-J+1} - \Psi^{-J+2}\right] \tag{3.63}$$

$$\partial_z \Psi^{J} \to \frac{1}{2a_z}\left[3\Psi^{J} - 4\Psi^{J-1} + \Psi^{J-2}\right] \tag{3.64}$$

where $\pm J$ are the endpoints of the z direction such that $2J+1 = N_z$ (N_z is the total number of lattice points along the z direction).

Eq. (3.62) will also take a special form for the first τ step, when one evolves the Dirac wavefunction starting with the initial condition which is know at $\tau = 0$. For the first step the τ derivative can be discretized only to first order accuracy. To obtain a similar equation as Eq. (3.62) for the first step is just enough to replace $2a_\tau$ in Eq. (3.62) with a_τ. The resulting equation will be used when evolving the Dirac wavefunction from the initial condition to the first step as well as when bringing both components of Ψ (Ψ^+ and Ψ^-) to the same τ value.

3.4.2 Solving the linear system

The numerical evolution of the Dirac equation from one τ step to the next reduces to solving the following linear system of equations:

$$M\ \Psi^{\pm}_{n+1} = \xi_n \tag{3.65}$$

with $\Psi^{\pm}_{n+1}$ the column matrix which stores the values of the Dirac field for all points on the z-direction at the $n+1$ time step for a given $\mathbf{x_T}$ transverse lattice point. The $\Psi^{\pm}_{n+1}$ vector can be chosen such that the first entry corresponds to $j = -J$ (the left most point of the z-direction) and the last one corresponds to $j = J$ (the right most point of the z-direction). ξ_n is a column matrix which has as entries the right hand side of equation Eq. (3.62). M is a square matrix whose entries can be read from the left hand side of Eq. (3.62).

A first step in solving this system would be to explicitly take into account the Dirac spinor structure of the Dirac field, which would give:

$$M\ \Psi^{\pm}_{n+1}(i) = \xi_n(i) \tag{3.66}$$

where i runs from 1 to 4 and denotes the spinor entry of the $\Psi^{\pm}$ field given as:

$$\Psi^{\pm}_{n+1} = \begin{pmatrix} \Psi^{\pm}_{n+1}(1) \\ \Psi^{\pm}_{n+1}(2) \\ \Psi^{\pm}_{n+1}(3) \\ \Psi^{\pm}_{n+1}(4) \end{pmatrix} \qquad \xi_n = \begin{pmatrix} \xi_n(1) \\ \xi_n(2) \\ \xi_n(3) \\ \xi_n(4) \end{pmatrix}. \tag{3.67}$$

The M matrix in this case is simpler than the one in Eq. (3.65) since it does not have a spinor structure and also since it does not depend on the Dirac spinor entry i - it is obvious from Eq. (3.62) that M is Dirac spinor independent. To simplify notations, until the end of this section, Eq. (3.66) will be written just as $M\Psi = \xi$.

M is a $N \times N$ matrix[1,2] which is almost trigonal (has entries only on the diagonal, above and below the diagonal plus two more entries - m_{13} and m_{NN-2}). Schematically the M matrix is given by:

$$M = \begin{pmatrix} m_{11} & m_{12} & m_{13} & 0 & & \dots & & \\ m_{21} & m_{22} & m_{23} & 0 & & & & \\ 0 & m_{32} & m_{33} & m_{34} & & & & \\ \vdots & & & \ddots & & & & \vdots \\ & & & & m_{N-2N-3} & m_{N-2N-2} & m_{N-2N-1} & 0 \\ & & & & 0 & m_{N-1N-2} & m_{N-1N-1} & m_{N-1N} \\ & \dots & & & 0 & m_{NN-2} & m_{NN-1} & m_{NN} \end{pmatrix} \quad (3.68)$$

where the entries of the M matrix can be easily read from Eq. (3.62). If the gluonic field is generated by a SU(N_c) local gauge symmetry (with N_c the number of colors) than each element of the M matrix is in fact a $N_c \times N_c$ matrix.

The simplest way to solve the system given in Eq. (3.66) with the matrix M given by Eq. (3.68) is to use the LU decomposition method. The matrix M is written as:

$$M = LU \quad (3.69)$$

where L is a lower diagonal matrix and U is an upper diagonal matrix with entries

[1] M is a $N \times N$ matrix only when looking at the m_{ij} elements, since each m_{ij} term is a $N_c \times N_c$ matrix (N_c=number of colors), M is even a larger matrix.

[2] In this section we will denote for simplicity $N \equiv N_z = 2J + 1$.

given by:

$$L\,U = \begin{pmatrix} 1 & 0 & 0 & & \dots & & \\ l_1 & 1 & 0 & & & & \\ 0 & l_2 & 1 & & & & \\ \vdots & & \ddots & & & & \vdots \\ & & & l_{N-3} & 1 & 0 & 0 \\ & & & 0 & l_{N-2} & 1 & 0 \\ & \dots & & 0 & l_N & l_{N-1} & 1 \end{pmatrix} \begin{pmatrix} d_1 & u_2 & u_1 & 0 & & \dots & \\ 0 & d_2 & u_3 & 0 & & & \\ 0 & 0 & d_3 & u_4 & & & \\ \vdots & & & \ddots & & & \vdots \\ & & & & d_{N-2} & u_{N-1} & 0 \\ & & & & 0 & d_{N-1} & u_N \\ & \dots & & & 0 & 0 & d_N \end{pmatrix}$$

Comparing the above equation with Eq. (3.68), one obtains the following algorithm:

1. Set $d_1 = m_{11}$, $u_1 = m_{13}$ and $u_2 = m_{12}$.

2. Set $l_1 = m_{21}d_1^{-1}$ and $u_3 = m_{23} - l_1u_1$.

3. Set $u_j = m_{j-1j}$ for all $j \geq 4$.

4. Set $d_j = m_{jj} - l_{j-1}u_j$ (for $2 \leq j \leq N-1$) and $l_j = m_{j+1j}d_j^{-1}$ (for $2 \leq j \leq N-2$).

5. Set $l_N = m_{NN-2}d_{N-2}^{-1}$, $l_{N-1} = (m_{NN-1} - l_Nu_{N-1})d_{N-1}^{-1}$ and $d_N = m_{NN} - l_{N-1}u_N$.

After finding the elements of both the LU matrices as well as for the ξ column vector, the equation $LU\Psi = \xi$ can be solved as follows. Start by denoting $\chi = U\Psi$, then the linear system becomes $L\chi = \xi$, which can simply be solved by:

1. Set $\chi_1 = \xi_1$.

2. Set $\chi_j = \xi_j - l_{j-1}\chi_{j-1}$ for $2 \leq j \leq N-1$.

3. Set $\chi_N = \xi_N - l_N\chi_{N-2} - l_{N-1}\chi_{N-1}$.

In a numerical code the values of χ can be stored in the same memory partition that stores the values of the ξ array. Now the remaining linear system of equations reads $U\Psi = \chi$, which can be solved as:

1. Set $\Psi_N = d_N^{-1}\chi_N$.

2. Set $\Psi_j = d_j^{-1}(\chi_j - u_{j+1}\Psi_{j+1})$ for $N-1 \geq j \geq 2$.

3. Set $\Psi_1 = d_1^{-1}(\chi_1 - u_2\Psi_2 - u_1\Psi_3)$.

The final set of instructions give the components of the Dirac field at the $n+1$ time step for a given Dirac spinor i. Now this algorithm must be iterated for the remaining 3 Dirac spinors. This part of the numerical code can be sped up by choosing a smart basis for the Dirac γ matrices. In the Weyl or chiral basis the fields $\Psi^{\pm}$ have only 2 nonzero entries each, such that the above algorithm has to be used only twice at each transverse point for each τ step (instead of 4 times).

For the full 3+1 dimensions case, for each τ step the system will have to solve this algorithm $2N_xN_y$ times (with N_x and N_y the size of the lattice in the x and y direction respectively). For the case of 1+1 dimensions, this algorithm must be solved only once for each τ step. For more details about the implementation of this algorithm see the Appendix B.

3.4.3 The quark initial condition on the lattice

To obtain the lattice version for the initial condition of the antiquark wavefunction we can start from Eq. (3.37). This can be easily taken from the continuum and onto the lattice since it does not explicitly contain gauge fields, but only covariant derivatives and Wilson lines. The covariant derivatives on the lattice are given in a gauge invariant way by Eq. (3.60). The same equation also determines the dispersion relation, since the lattice quark momentum depends on the expression of the discretized derivative.

On a N point linear lattice the allowed values of the momentum are $k_x = \frac{2\pi}{N}n_x$ with $n_x = -\frac{N}{2}+1, \ldots, \frac{N}{2}$, with similar expression for the other directions. The discretization choices made in Sec. 3.4.1 mean that the lattice dispersion relation for a quark is given by:

$$\begin{aligned} E^2 &= m^2 + \frac{\sin^2(k_x a_x)}{a_x^2} + \frac{\sin^2(k_y a_y)}{a_y^2} + m_T^2 \sinh^2(y_k) \\ &= m_T^2 \cosh^2(y_k) \end{aligned} \tag{3.70}$$

where y_k is the quark rapidity and m_T is the transverse mass given by:

$$m_T^2 = m^2 + k_T^2 \tag{3.71}$$

$$k_T^2 = \frac{\sin^2(k_x a_x)}{a_x^2} + \frac{\sin^2(k_y a_y)}{a_y^2} \tag{3.72}$$

which is the lattice transverse momentum for fermions.

As can be seen from Eq. (3.72), there are several values of (k_x, k_y) which give the same fermion momentum k_T. This effect is know as fermion doubling. One way to deal with it is to restrict to only a quarter of the Brillouin zone, effectively considering only momenta which do not create a degeneracy in the fermion momentum. In our case, we will restrict to fermion momenta $k_{x,y} = \frac{2\pi}{N} n_{x,y}$ with $n_{x,y} = -\frac{N}{4}, \ldots, \frac{N}{4}$ for both the momentum of the initial antiquark as well as for that of the final quark.

3.5 Numerical Results

3.5.1 Gluon production

In this section we compute a few observables of the gluonic field and compare them with the numerical results from [27]. This section will be short since the gluonic field evolution is not the main part or the most complex one of our study.

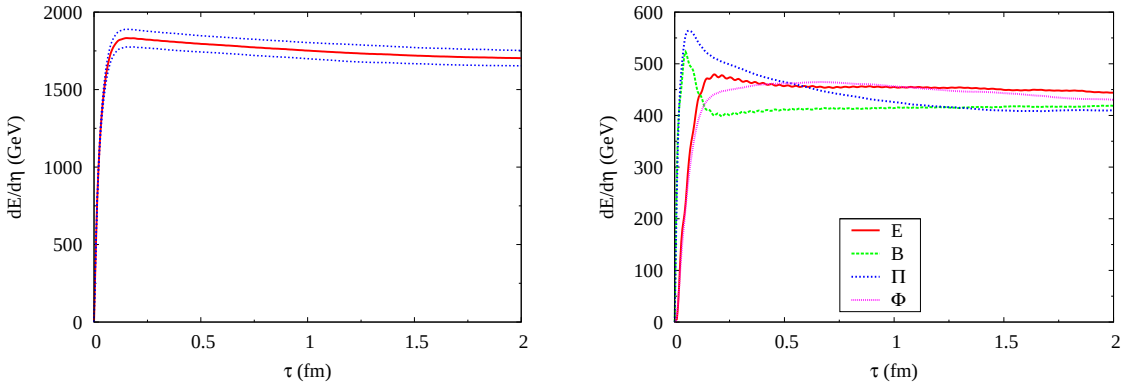

Figure 3.2: Left: The total energy in the gluonic field per unit rapidity for $\mu = 0.5$ GeV. The dotted curves give a statistical error estimate for 5 different configurations of the initial charge distribution. Right: The energy per unit rapidity in each field component for the same simulation as in the right graph.

The gluon evolution is characterized by three free parameters: the strong coupling constant g, the color charge density parameter μ and the transverse area of the nucleus πR_A^2. For each numerical simulation we have that $\pi R_A^2 = N^2 a^2$ with N^2 the number of lattice points for the transverse lattice and a the lattice spacing in the transverse direction. For the numerical results presented here we take $\pi R_A^2 = 150$ fm^2 and $g = 2$. Even though the model has 3 physical parameters, the qualitative behavior of it depends only on one parameter, $g^2 \mu R_A$. Small values of the $g^2 \mu R_A$ give the weak field limit while large values of $g^2 \mu R_A$ give rise to a strong field. The latter is the regime where we expect that the model described in Sec. 3.1 to be valid.

The left panel in Fig. 3.2 shows that the energy per unit rapidity in the field increases very fast at small τ values after which it remains at almost a constant value. As expected from the equipartition theorem, the energy in the fields and in the momenta should be the same. This is the case (up to numerical errors), as can be seen from the right panel in Fig. 3.2 which shows the energy in each component

of the field. Using this fact, the multiplicity can be defined as [27]:

$$n(\mathbf{k_T}) = \frac{1}{N^2}\frac{2}{|\mathbf{k_T}|}\left[\frac{g^2}{2\tau}E_i^a(\mathbf{k_T})E_i^a(-\mathbf{k_T}) + \frac{\tau}{2}\pi^a(\mathbf{k_T})\pi^a(-\mathbf{k_T})\right]. \tag{3.73}$$

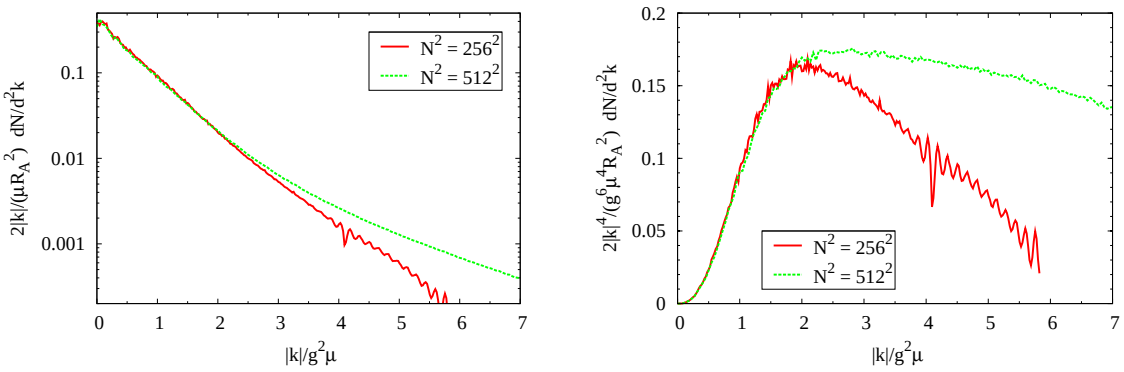

Figure 3.3: Left: $\frac{2\pi|\mathbf{k_T}|}{\pi R_A^2}\frac{dN}{d^2k_T}$ as a function of the transverse momentum for $\mu = 0.5$ GeV for two different lattice sizes. Right: $\frac{2\pi|\mathbf{k_T}|^4}{g^6\mu^4\pi R_A^2}\frac{dN}{d^2k_T}$ as a function of the transverse momentum for $\mu = 0.5$ GeV for two different lattice sizes.

Using Eq. (3.73) one can compute the gluon spectrum; the numerical results are shown in the left panel in Fig. 3.3. In the weak field limit, one expects that $\frac{dN}{d^2k_T} \propto \frac{1}{|\mathbf{k_T}|^4}$ [27]. Hence we would expect that $|\mathbf{k_T}|^4\frac{dN}{d^2k_T}$ tends to a constant in the weak field limit. The right panel of Fig. 3.3 shows that for high $|\mathbf{k_T}|$ there is indeed a crossover to something similar to a $\frac{1}{|\mathbf{k_T}|^4}$ behavior, but that the exact behavior is not reached. This may be due to lattice size effects, as can be seen by comparing the two lattice sizes. Another reason for the mismatch is that the CGC formalism works best in the classical strong field regime while the above predictions holds only in the weak field limit. All the numerical result obtain in this section are in very good agreement with the ones given in [27].

3.5.2 Quark production in 1+1 dimensions

In this section we analyze the behavior of the numerical solution for the Dirac equation for one spatial dimension. This is especially useful since it allows to analyze the numerical solution on a much larger range of parameters than it would be possible in three spatial dimensions (due to memory and computational time limitations).

Moreover, many of the parameter dependencies of the equation for 1+1 dimensions (one spatial and one time) also hold for the full 3+1 dimensions.

a) Time evolution of the numerical Dirac solution

The Dirac equation in (τ, z) coordinates can pose a problem due to the $1/\tau$ term from Eq. (3.47). In the analytical case, when $\tau \to 0$, we have that $\tau\partial_\tau \Psi^{\pm} = 0$, hence analytically the $1/\tau$ factor does not pose a problem. Moreover, the $1/\tau$ factor arises due to the new coordinates used, not due to a physical singularity. For the numerical implementation of the equation, we have to be careful that the right hand side term of the Dirac equation does not pose a problem due to discretization errors. In general, the larger the lattice spacing is, the larger are the discretization errors which arise from replacing derivatives with finite differences. To minimize these errors, one can choose a smaller lattice spacing or can replace the derivative with higher order discretization schemes.

This is why it is important to study the behavior of our code for different parameter settings around $\tau = 0^+$. For the first few time steps, the numerical Dirac wavefunction will be independent of the a_τ (lattice spacing along the τ direction) value. This is true since everywhere in the Dirac equation we only find the ratio a_τ/τ and not a_τ or τ alone (in fact we have a few $\sqrt{\tau^2 + z^2}$ terms but for small τ these terms are just $|z|$ plus small errors).

Fig. 3.4 shows the time behavior of the Dirac field at a given lattice point for different values of the ma_z parameter. As expected, the bigger the ma_z parameter, the greater is the difference from the "expected" result. Another important feature of the results in Fig. 3.4 is the "jiggling" of the numerical solution at the start of the simulation for high values of the ma_z parameter, as shown in the inlet in Fig. 3.4. This is due to discretization errors and to the $1/\tau$ term in the Dirac equation. For large ma_z parameters the error in the discrete z-derivative are large and hence the right hand term from Eq. (3.47) is large (analytically it should be 0). The consequences are that the τ derivative is large, this is why initially the change in the Dirac wavefunction between two consecutive time steps can be large. The size of this "jiggling" can be

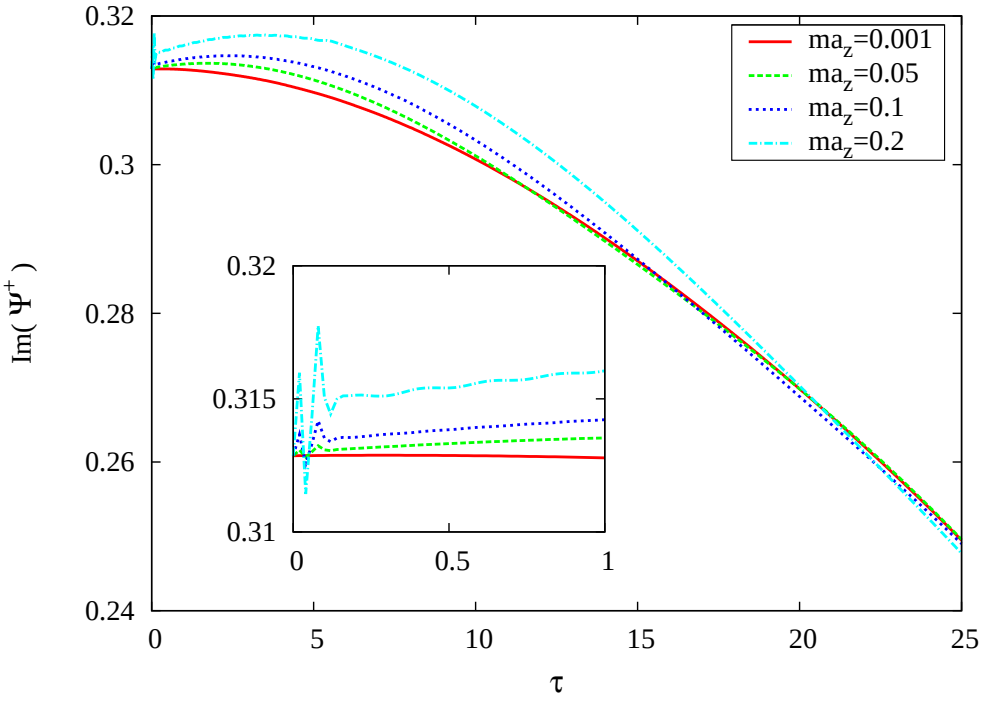

Figure 3.4: The dependence of the wavefunction on proper time for different values of the longitudinal lattice spacing for the free Dirac equation ($\phi = 0$).

decreased only by choosing a smaller ma_z value and not by choosing a smaller a_τ. To minimize the "jiggling" one should restrict to $ma_z \leq 0.05$, even though this will not always be possible. Fig. 3.4 also shows that even for a strong "jiggling" at early times, the numerical solution does not diverge from the expected result for later times.

The results shown in Fig. 3.4 are only for $y = 0$. If $y \neq 0$ than the size of the error is controlled by the values of the $ma_z e^{|y|}$ parameter. This is because the error in the discretization of the z-derivative depends on the value of the parameters $ma_z e^{y}$ and $ma_z e^{-y}$ (these are the parameters that give the z behavior of the initial condition for the Dirac field in 1+1 dimensions).

b) Free Dirac Equation

For the free case, we expect the amplitude for quark pair production to be 0. But if we compute the amplitude M for each of the two branches in which we split the initial condition for the 1+1 dimensions Dirac field (see Eqs. (3.52)-(3.53)) we expect to get a non-zero amplitude given by Eq. (3.55) in Sec. 3.3.3.

The amplitude for quark production is given by Eq. (3.50) which for the τ, z coordinate system reduces to:

$$M(y,y') = \int \frac{\tau dz}{\sqrt{\tau^2+z^2}} \bar{u}(y') e^{im[\sqrt{\tau^2+z^2}\cosh(y') - z\sinh(y')]} \gamma^0\gamma^\tau \Psi(\tau,z) \qquad (3.74)$$

where $\Psi(\tau,z)$ is the numerically evolved Dirac field with initial condition given by Eqs. (3.52)-(3.53). Eq. (3.50) suggest that $M(y,y')$ will be mainly given by the region $\eta \approx y'$ (due to the $e^{im\tau\cosh(\eta-y')}$ factor which oscillates very fast for large exponents). When η is very different from y', the argument of the hyperbolic cosine will be large, and hence the exponential function will vary very fast with η. This would mean that we can get an accurate value for $M(y,y')$ just by considering only a relatively small interval in η around $\eta = y'$.

An important inconvenience of Eqs. (3.50) and (3.74) for finite integration limits is that the integrand is nonzero at the integration boundaries (this is because the Dirac field does not die out at large η). In fact this integrand will vary greatly for even a slightly change in the integration limits, due to the fast variation of the exponential function. So the quark amplitude defined previously is a highly oscillatory function of the integration limits. In the analytical case when the integration limits are infinite, this oscillations will average out and will give rise to a well defined result, but this is not the case for the numerical simulation with a finite lattice. To solve this problem we compute $M(y,y')$ from Eqs. (3.50) and (3.74) for different integration limits and than we will take an average of the values thus obtained. To obtain accurate results, the range in η (or z) over which we vary the integration limits has to contain several oscillation periods of the $M(y,y')$ function. In the following, each time we compute M, we average over the z integration limits such that the integration limits vary from $z_{max}/2$ to z_{max} (with $2z_{max}$ the length of the lattice in the z direction).

First we test if indeed we can reproduce the analytical results from Eq. (3.50) by just taking a small interval in η around $\eta = y'$. Since we only know the numerical Dirac field at given z points, we will use Eq. (3.74) for computing the quark production amplitude. The integration limits z_{min} to z_{max} will be given by the corresponding value of η_{min} to η_{max} for which we want to compute $M(y,y')$. Since we consider only

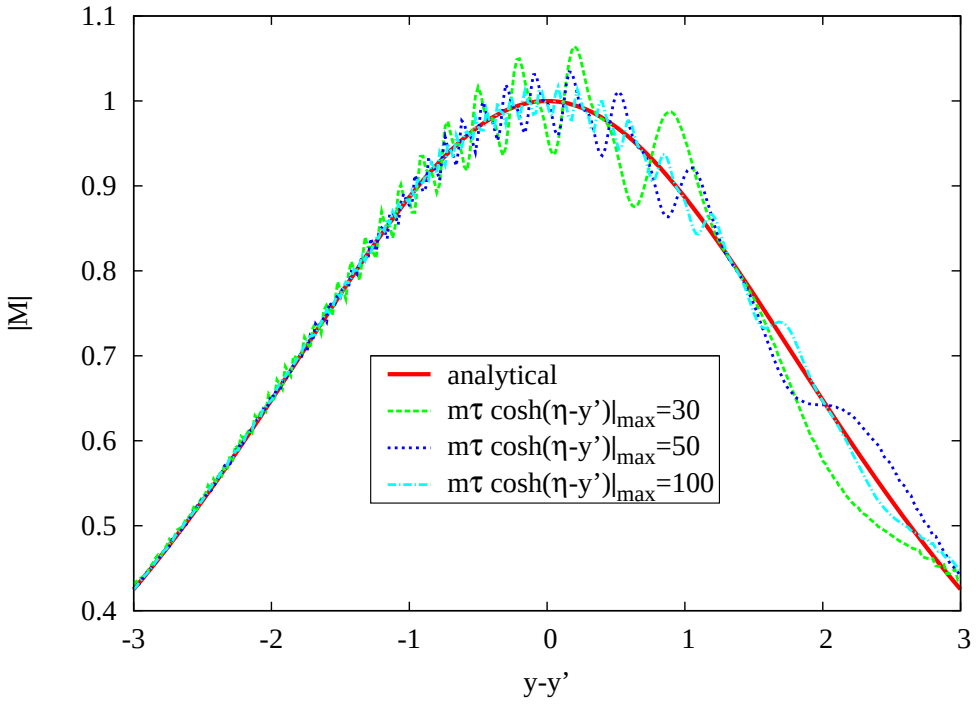

Figure 3.5: The amplitude M of one branch for the free Dirac equation when considering a fixed space-time rapidity interval. The integration interval over η varied for each value of y' such that the boundaries are given by the solution of the equation $m\tau\cosh(\eta - y') = const$, with the value of *const* given in the legend of the graph.

a certain interval around $\eta = y'$, the integration limits η_{min} to η_{max} will depend on y'. We choose the η integration limits such that at the integration boundaries the term $m\tau\cosh(\eta - y')$ has a given value. We obtain the same shape for $M(y, y')$ indifferently of the value of $m\tau\cosh(\eta - y')$ at the boundaries as long as $m\tau\cosh(\eta - y') > 25$, see Fig. 3.5. By taking a bigger lattice we get a smaller error when evaluating the oscillating integral $M(y, y')$ (since we average over a larger number of periods), but aside from this, larger values of $m\tau\cosh(\eta - y')$ at the boundaries do not change the overall amplitude M. So the results from Fig. 3.5 support the conclusion that the amplitude M is given by a small interval in η around $\eta = y'$.

Let us analyze in more detail the asymmetry of the graph in Fig. 3.5. The numerical result is very close to the analytical one for $y - y' < -1$, but for $y - y' > -1$ it has a much larger amplitude of oscillation around the analytical result. Around $y - y' = 0$ a given interval in η corresponds to less lattice points (for a fixed a_z) than for larger values of $|y - y'|$. So around $y - y' = 0$ there are not enough lattice points to

get a good estimate on the oscillating function, even though the interval over which we average contains several periods of oscillation. For $y - y' > 1$ (i.e. $y' < -1$) the problem arises since we use the right branch (Eq. (3.53)) as the initial condition for the Dirac field. For the right branch the Ψ field is constant for $z < 0$ and varies for $z > 0$ (at $\tau = 0$), so at some time τ the Ψ field will mainly vary for $z > 0$ and also for some values of $z < 0$ (but only for those with z not too far from 0). Since for $y' < -1$ the main integration interval when computing M will be for negative z values, there are not enough z lattice points in the region where Ψ varies. Choosing the left branch (Eq. (3.52)) as the initial condition gives an asymmetry which is mirrored around $y - y' = 0$ to the one in Fig. 3.5.

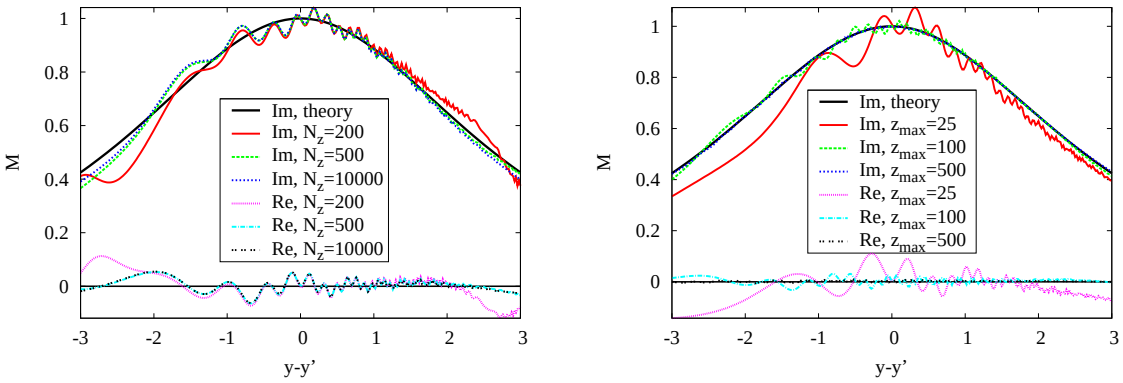

Figure 3.6: Left: The amplitude M of one branch for different lattice sizes in the z-direction (for a constant z_{max}). Right: The amplitude M of one branch for different physical sizes of the lattice in the z-direction (for a constant a_z). For $z_{max} = 500$ there is no visible difference between the analytical and the numerical result.

Since the main contribution to the amplitude M is given by the interval around $\eta = y'$ and taking into consideration that $z = \tau \sinh \eta$, one can conclude that for a given proper time τ we can compute M only for $\sinh y' \leq z_{max}/\tau$. After also taking into account the averaging procedure to deal with the oscillating result, the above relation should read $\sinh y' \leq z_{max}/(2\tau)$. The range in rapidity is also limited by the finite lattice spacing along the z direction which gives a ultraviolet cutoff for the z momentum $\sinh y \leq 2\pi/(ma_z)$.

In the following the amplitude for quark production is computed using an integration over the z parameter (Eq. (3.74)) taking as integration limits $-z_{max}$ to z_{max}. The

left panel in Fig. 3.6 shows the dependence of the numerically computed amplitude on the lattice size. The numerical results agree well with the analytical ones. For $N_z \geq 500$ there is no dependence of the amplitude on the number of lattice points. The difference between the result for $N_z = 200$ and the rest may be due to the small number of lattice points or due to bigger discretization errors. In the left panel of Fig. 3.6 the $N_z = 200$ curve corresponds to $ma_z = 0.25$, which suggests that a small difference is to be expected due to discretization errors (see Fig. 3.4). The difference between the numerical and analytical result in Fig. 3.6 is due to a relatively small z_{max} value. Using a larger z_{max} results in a more accurate value for M - see the right panel in Fig. 3.6, where for $z_{max} = 500$ there is no visible difference between the analytical and the numerical result.

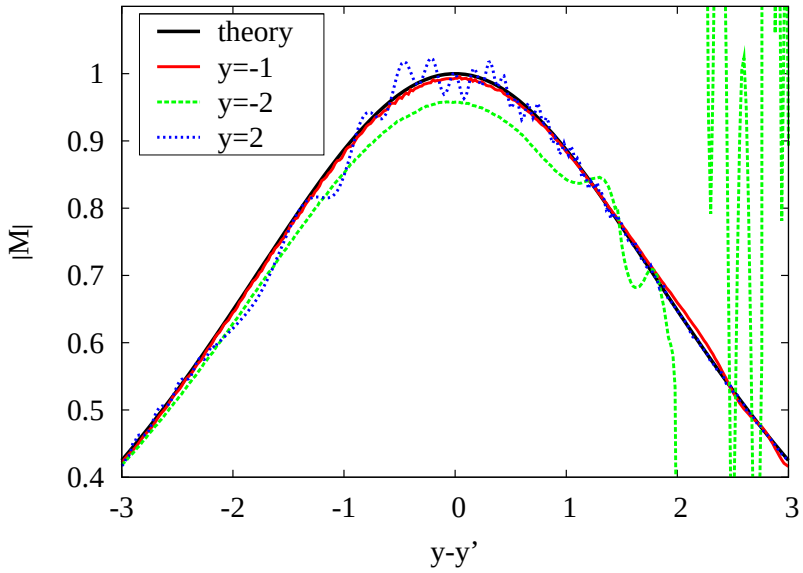

Figure 3.7: The amplitude of one branch for the free Dirac equation for different rapidities. The rest of the parameters are: $a_\tau = 0.01$, $mass = 0.5$, $N_\tau = 100$, $N_z = 5 \cdot 10^3$ and $a_z = 0.2$.

Due to boost invariance, the amplitude M should be independent of y (it should only depend on $y - y'$). Since the calculations are done using z as the longitudinal variable and not the rapidity, it is nontrivial to check that M is boost invariant. Fig. 3.7 shows that indeed the amplitude for pair production is independent (within some numerical errors) on the rapidity y. What is interesting to observe is that the numerical calculation breaks down for $y - y' > 2$ when $y = -2$. The UV momentum

cutoff is $y < 5$ while the additional condition $\sinh y' \leq z_{max}/(2\tau)$ yields $y' < 6$. So the breakdown for $y - y' > 2$ when $y = -2$ is possibly due to the UV cutoff, but this does not explain why there is no breakdown for $y - y' < -2$ when $y = 2$. The results in Fig. 3.7 are for the right branch, while for the left branch the picture is very similar but with the graph mirrored around $y - y' = 0$.

c) Dirac Equation in an External Field

The next step is to study the behavior of the discretized Dirac equation solutions in the presence of an external field. In one spatial dimension, the solution of the gauge time evolution equations is given by a constant electric field off the light cone [26]. So to study the behavior of the discretized Dirac equation in 1+1 dimensions in the presence of external fields one has to introduce it by hand. This external field should have two parameters, a mass parameter which tells how fast the field vary with τ and also a constant which controls the strength of the field. We take the external field as [26]:

$$\Phi(\tau) = cQ_s\tau J_1(Q_s\tau) \tag{3.75}$$

where Q_s is our mass parameter and c controls the field strength (with $c \ll 1$ representing the weak field limit). Such a choice is motivated in two ways, similar results were computed in [26], so it provides a good opportunity to compare our results with other numerical results. Also, the choice in Eq. (3.75) admits analytical solutions for the amplitude of quark-antiquark pair production in the weak field limit [26]. For weak fields, using first order perturbative results, one expects the amplitude $|M|$ to have a peak at:

$$\cosh\left(\frac{\Delta y}{2}\right) = \frac{Q_s}{2m}. \tag{3.76}$$

This means that for $Q_s < 2m$ we expect to have only small values for $|M|$, which should abruptly increase for $Q_s = 2m$ (with a prominent peak at $\Delta y = y - y' = 0$). For $Q_s > 2m$ the quark production amplitude should have two peaks given by the solutions of Eq. (3.76).

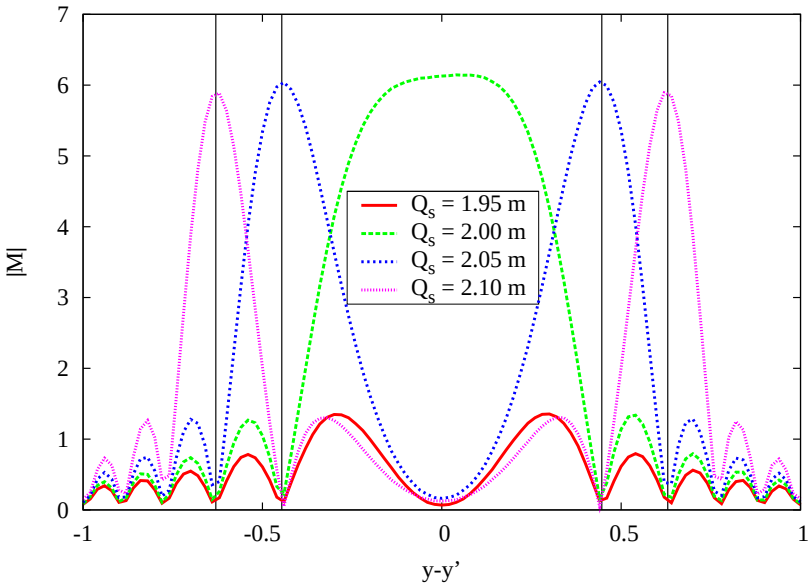

Figure 3.8: The dependence of the amplitude for quark production for different values of the Q_s parameter for weak fields ($cQ_s = 0.05m$) at $m\tau = 125$. The vertical lines show the position of the peaks predicted by Eq. (3.76) corresponding to the Q_s values plotted above.

The numerical results for a weak field ($cQ_s = 0.05m$) are shown in Fig. 3.8. As expected, for $Q_s < 2m$ we observe that the amplitude for pair production $|M|$ is small. For $Q_s \geq 2m$ we obtain the expected peak behavior predicted by Eq. (3.76). It is also interesting to observe that the peaks of the numerical result coincide relatively well with the predictions resulted from first order perturbation theory.

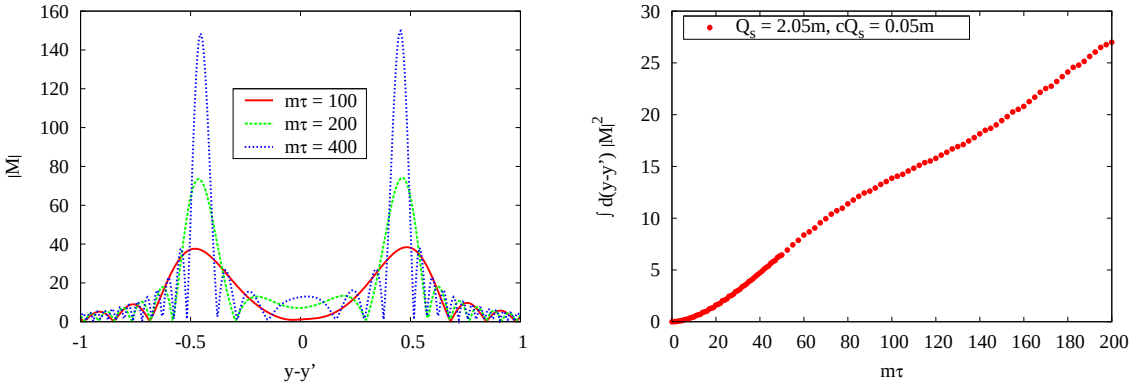

Figure 3.9: Left: The dependence of quark production amplitude $|M|$ on rapidity at different times τ for $Q_s = 2.05m$ and $cQ_s = 0.5m$. Right: The number of produced pairs per unit rapidity $\int |M|^2 d(y - y')$ as a function of proper time τ for $Q_s = 2.05m$ and $cQ_s = 0.05m$.

Fig. 3.9 shows the dependence of $|M|$ for different τ values. It can be seen

that the height of the peaks increases linearly with time while their width shrinks with time. But the area under the peaks ($\int |M| d(y-y')$) remains approximately constant pointing to delta function dependencies for $\tau \to \infty$. In Fig. 3.9 we also see that the number of quark-antiquark pair produced ($\int |M|^2 d(y-y')$) increases almost linearly with τ, especially at large $m\tau$ values. These results are in agreement with the numerical results obtain in [26].

3.5.3 Quark production in 3+1 dimensions

In this section we compute the quark production amplitude for the full three dimensional case. First we analyze the solutions of the Dirac equation in the absence of the gauge field; solutions which can be compared to analytical predictions. Then we study the quark production amplitude in the presence of the gluonic field given in Sec. 3.1, results that we compare to those in [29, 30, 31].

For the 3+1 dimensional case it is useful to split Eq. (3.33) into two parts:

$$|M(\mathbf{q_T}, \Delta y)|^2 = \int \frac{d^2 p_T}{(2\pi)^2} \left| \int \tau d^2\mathbf{x_T} d\eta \; e^{-i\mathbf{p_T}\cdot\mathbf{x_T}} e^{i m_T \tau \cosh(y-\eta)} \bar{u}(p) \gamma^\tau \Psi_q(\tau, \eta, \mathbf{x_T}) \right|^2 \quad (3.77)$$

$$\frac{dN}{dy} = \int \frac{d^2 q_T}{(2\pi)^2} \frac{d(\Delta y)}{16\pi^2} |M(\mathbf{q_T}, \Delta y)|^2 \quad (3.78)$$

where $|M(\mathbf{q_T}, \Delta y)|^2$ denotes the amplitude squared for quark production integrated over all the transverse phase space available to the final state quark (for simplicity, in the following we will refer to $|M|$ as the amplitude). The quantity $\frac{dN}{dy}$ denotes the number of quarks produced (which is also the number of quark pairs) per unit rapidity. With Δy we denote the rapidity difference between the initial state antiquark (at $t \to -\infty$) and the final state quark. Since the gauge field is boost invariant, the quark production amplitude depends only on the rapidity difference Δy and not on the individual rapidities of the quark or antiquark (as illustrated in Eqs. (3.77)-(3.78)).

The parameters of the numerical model are the strong coupling constant g (we take $g = 2$[1]), the nucleus transverse area πR_A^2, the source density parameter μ and the quark mass m. As in the case of the gluonic field only, the typical momentum

[1] In the classical field theory approach there is no reason for g to vary with energy.

scale is given by $g^2\mu$ while the parameter $g^2\mu R_A$ characterizes the strength of the gauge field (a small value of the parameter gives the weak field limit).

The Dirac wavefunction is stored on a $N^2 N_z$ lattice with $N = 180$ and $N_z = 400$. The numerical transverse area N^2a^2 corresponds to the physical area via $N^2a^2 = \pi R_A^2 = 141$ fm^2 which for a fixed N gives the size of the transverse lattice spacing a. The following numerical results are obtained for $a_z = 0.2a$, $a_\tau = 0.02a$ and for $\tau = 0.25$ fm which corresponds to about 200 time steps (unless stated otherwise).

Due to the large lattice size, the Dirac wavefunction for $N = 180$ and $N_z = 400$ needs 1.2 GB of RAM in single precision (there are 4 Dirac spinors and 3 colors). Moreover, the time evolution for each time step takes 60 - 80 s/($180^2 \cdot 400$)=4.5 to 6.0 μs for each lattice point depending on the processor. So it takes 3 to 4 hours to evolve the Dirac equation to the proper time $\tau = 0.25$ fm for a given configuration of initial charge.

a) The free Dirac equation

In the case of the free Dirac equation one can make analytical predictions for the quark pair production amplitude. Similarly as for the case of one spatial dimensions, $|M|^2$ defined in Eq. (3.77) is given by Eq. (3.55) when the initial antiquark wavefunction is given by only one of the two branches from Fig. 3.1. When using both branches, the number of quark pairs is zero as expected in the absence of an external field.

Fig. 3.10 shows that indeed the numerical results for a wide range of quark masses agree with the theoretical predictions. The agreement is not as good as for the 1+1 dimensional case, since for 3+1 dimensions the finite memory available imposes a strict limit on the lattice size, and hence on the maximum value of the mz_{max} parameter[1]. Thus the discrepancies between the numerical and the analytical result from Fig. 3.10 are mainly due to the limitation of the averaging procedure (see Sec. 3.5.2). We also tried several other procedures to deal with the oscillating values of $|M|^2$ at the ends of the lattice in the z-direction. Some of them indeed give a numerical

[1]The mz_{max} parameter is the one that controls how accurate is the averaging procedure described in Sec. 3.5.2. For more details see the right panel in Fig. 3.6.

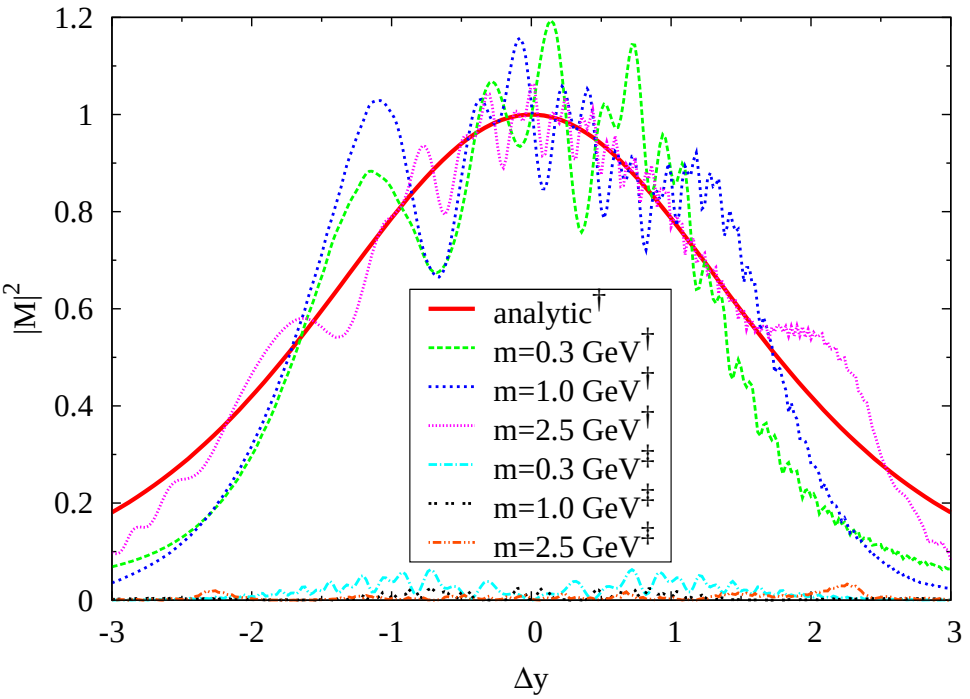

Figure 3.10: The dependence of the amplitude $|M|$ on the rapidity difference between quark and antiquark for different quark masses. † Numerical results obtained using only one of the two branches from Fig. 3.1. ‡ Numerical results obtained using both branches from Fig. 3.1.

result much closer to the analytical one, but they also have a major drawback. The form of $|M|^2$ depends very strongly on the parameters of those procedures and the analytical result is obtain only for a small range in those parameters. This is why we decided to use only the method of averaging $|M|^2$ over different integration limits (method described in Sec. 3.5.2).

The range of quark masses available in the numerical study is limited from two directions. We cannot simulate very small quark masses ($m \lesssim 0.1$ GeV) since the z lattice size in not large enough. For small quark masses the main contribution to the quark production amplitude comes from a wide interval of z values, interval which is not fully accessible for small N_z values. On the other hand, large quark masses ($m \gtrsim 3$ GeV) are not accessible due to the small transverse lattice.

b) Quark production in an external gauge field

The numerical result is expected to depend on the lattice size and spacing along the longitudinal direction, especially for small quark masses. So we studied the depen-

dence of the quark production amplitude $|M|^2$ on the lattice size and lattice spacing (see Fig. 3.11). We see that $a_z = 0.2a$ and $N_z = 400$ is more or less the limit which distinguishes between a strong dependence and a weak dependence of the result on the longitudinal lattice size and spacing. Moreover, the two graphs in Fig. 3.11 suggest that we obtained different numerical results mainly due to computing the result for

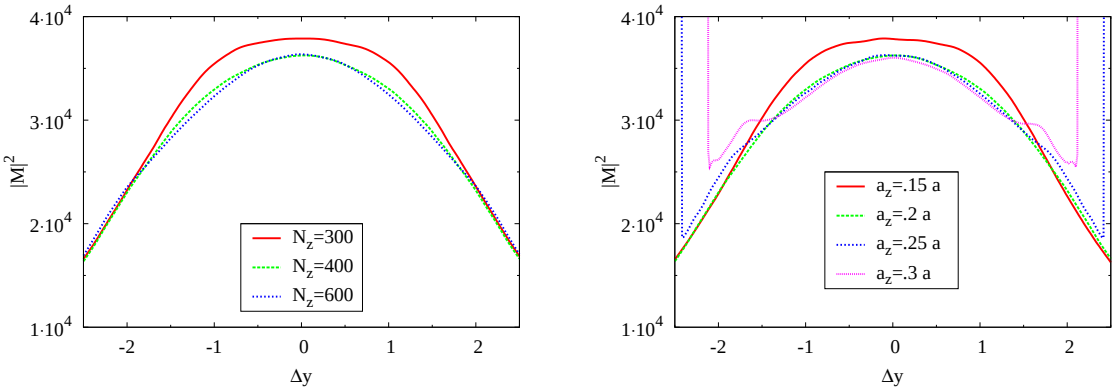

Figure 3.11: Left: Quark amplitude $|M|$ (in lattice units) as a function of Δy for different lattice size. Right: Quark amplitude $|M|$ as a function of Δy for different values of the lattice spacing along the z direction. a denotes the transverse lattice spacing. Both graph are at $\tau = 0.25$ fm, $m = 0.3$ GeV and transverse momentum $\mathbf{q_T} = (4, 4)$.

different values of z_{max}. As expected, the extension of the longitudinal lattice is not large enough to allow for an accurate averaging procedure of the oscillating integral. By varying the limits of the averaging procedure, we found that the numerical result can vary up to 10% (for $m = 0.3$ GeV). This variation becomes smaller for larger masses, such that for $m \gtrsim 1$ GeV, there is little change in the numerical results when varying the averaging boundaries. To cope with theses problems, one must take the continuum limit of the numerical results (especially for the low quark mass simulations). The vertical curves in the right panel of Fig. 3.11 as well as in Fig. 3.12 are due to the momentum cutoff because of the finite size of the lattice spacing along the z direction.

We found the quark production amplitude to be independent of the time step size in a wide range of values starting with $a_\tau = 0.04a$ and lower. Another nontrivial test is to study the dependence of $|M|$ on the initial antiquark rapidity. As explained earlier, due to boost invariance of the gauge field, we expect that the quark production

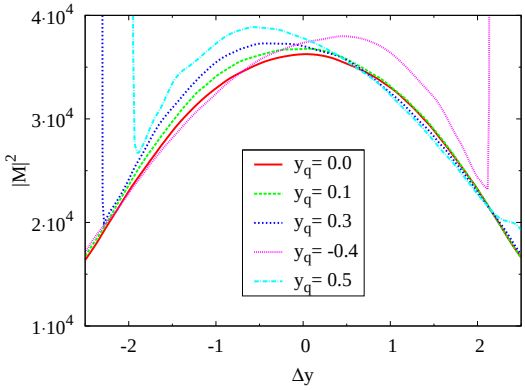

Figure 3.12: Dependence of amplitude $|M|$ (in lattice units) on rapidity difference Δy for different rapidities of the initial antiquark. The results are obtained at $\tau = 0.25$ fm, $m = 0.3$ GeV and transverse momentum $\mathbf{q_T} = (4, 4)$.

amplitude to be independent on the antiquark rapidity. This is not automatically satisfied since we use z as the longitudinal variable in the numerical calculations, and not the space-time rapidity η. As can be seen in Fig. 3.12, $|M|^2$ is independent on antiquark rapidity up to some numerical errors.

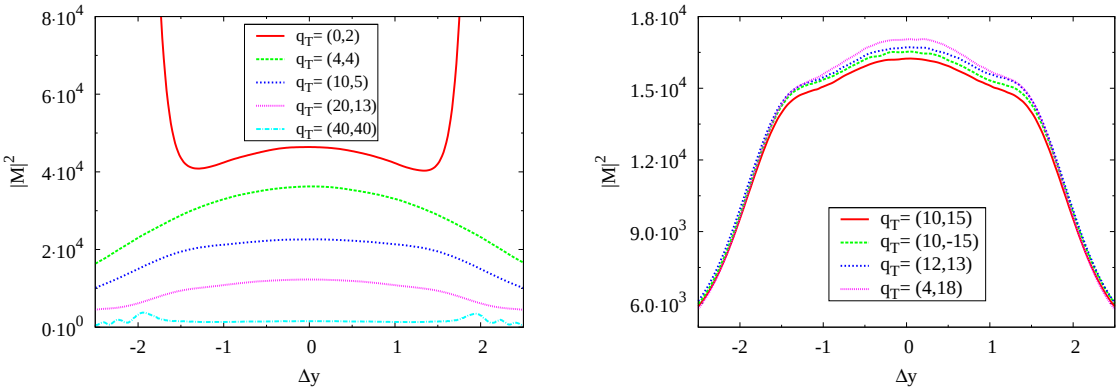

Figure 3.13: Left: Quark amplitude $|M|$ (in lattice units) as a function of Δy for different transverse momenta. Right: Quark amplitude $|M|$ as a function of Δy for different (q_x, q_y) but for the same $|q_T|$. Both results are obtained at $\tau = 0.25$ fm and $m = 0.3$ GeV.

As it can be seen from the left panel in Fig. 3.13, the quark production amplitude varies strongly with the values of the initial quark transverse momentum $|\mathbf{q_T}|$. But the right panel in Fig. 3.13 shows that $|M|^2$ is independent on the actual values of the momentum along the x and y directions and only depends on $|\mathbf{q_T}|$. This was expected, since the results presented in this section are averaged over different random distributions of color charge in the transverse plane. Thus there is no preferred

direction in the transverse plane, and any results can vary at most with $|\mathbf{q_T}|$, but not with the direction of $\mathbf{q_T}$.

The above result is especially useful since to compute the total number of quark pairs, one needs to sum over all the possible transverse momenta of the initial anti-quark (see Eq. (3.78)). Disregarding the doubler modes, on a $N^2 = 180^2$ lattice there are 90 different quark momenta for each direction. Computing $|M|^2$ for all possible values of the transverse momentum would result in more than $90^2 \cdot 3$ hours=3 years of computational time on a single CPU for just one initial configuration of color charge. This is an unfeasible task even when using a computer cluster with more than 100 CPU units.

To overcome the problem, one takes advantage of the independence on the direction of $\mathbf{q_T}$. Thus Eq. (3.78) reduces to:

$$\frac{dN}{dy} = \int \frac{|\mathbf{q_T}|\ d|\mathbf{q_T}|}{2\pi} \frac{d(\Delta y)}{16\pi^2}\ \ |M(|\mathbf{q_T}|, \Delta y)|^2. \tag{3.79}$$

If we know the values of the function only for a discrete set of $|\mathbf{q_T}|$ values, than Eq. (3.79) becomes:

$$\frac{dN}{dy} = \sum_i \frac{|\mathbf{q_T}|_{i+1} - |\mathbf{q_T}|_{i-1}}{2}\ \ \frac{|\mathbf{q_T}|_i}{2\pi} \int \frac{d(\Delta y)}{16\pi^2}\ \ |M(|\mathbf{q_T}|_i, \Delta y)|^2 \tag{3.80}$$

where $|\mathbf{q_T}|_i$ denotes the i-th element of the transverse momentum set of values. The above equation is valid for the continuum case, but for the discrete case the density of states is not the same as in the continuum since the dispersion relation is given by Eq. (3.72). So the discrete form of Eq. (3.80) is given by:

$$\frac{dN}{dy} = \frac{1}{N^2} \sum_i\ \ \Sigma(|\mathbf{q_T}|_i) \int \frac{d(\Delta y)}{16\pi^2}\ \ |M(|\mathbf{q_T}|_i, \Delta y)|^2 \tag{3.81}$$

where $\Sigma(|\mathbf{q_T}|_i)$ denotes the numbers of transverse momentum states that correspond to the transverse momentum $|\mathbf{q_T}|_i$ (i.e. the number of transverse momentum states with momentum between $|\mathbf{q_T}|_i - \frac{|\mathbf{q_T}|_i - |\mathbf{q_T}|_{i-1}}{2}$ and $|\mathbf{q_T}|_i + \frac{|\mathbf{q_T}|_{i+1} - |\mathbf{q_T}|_i}{2}$).

The transverse momentum spectrum for the quarks can be computed using Eq. (3.78) where we integrate $|M|^2$ over the rapidity difference. These spectra are shown in Fig.

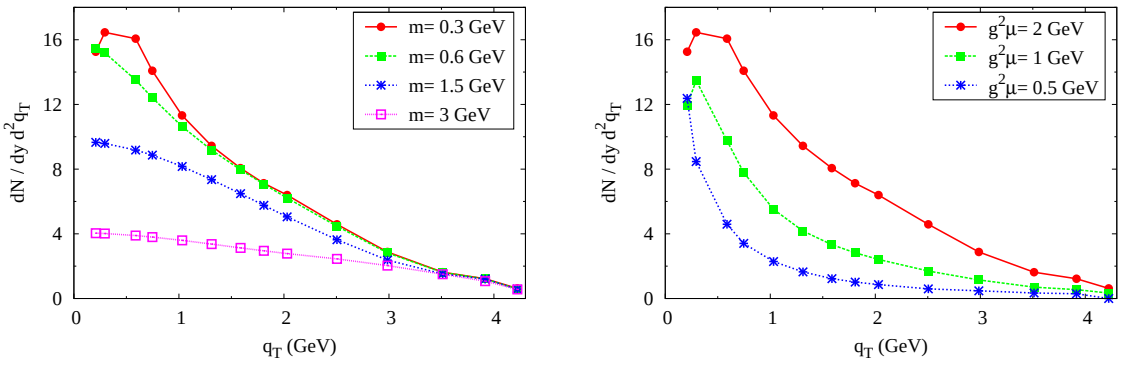

Figure 3.14: Left: The transverse momentum spectrum of quarks at $g^2\mu = 2$ GeV for different quark masses. Right: The transverse momentum spectrum of quarks at $m = 0.3$ GeV for different $g^2\mu$ values. Both results are obtained at $\tau = 0.25$ fm.

3.14. One expects the quark spectra to be flatter and smaller with increasing quark mass and larger with increasing values of the $g^2\mu$ parameter. This is exactly the behavior observed in Fig. 3.14, even though especially for small quark masses the change in spectrum is rather weak. Moreover, the spectra decrease only slowly at large transverse momentum suggesting a dependence on the transverse lattice cutoff a. This dependence should be studied by changing the size of the transverse lattice.

The quark spectrum at small transverse momenta is highly sensitive to the integration boundaries for the rapidity difference Δy. This is because, as it can be seen from Fig. 3.13, at small transverse momenta $|M|^2$ does not go to 0 as $|\Delta y|$ increases as is the case for larger transverse momenta. This is a problem mainly for the first 2 data points of each spectrum from Fig. 3.14. But this does not pose a big problem when computing the total number of quark pairs since the number of states for small transverse momenta is much smaller than the one for higher momenta, and thus the main contribution to $\frac{dN}{dy}$ comes from $|\mathbf{q_T}| \gtrsim 1$ GeV.

For computing the total number of pairs per unit rapidity we use Eq. (3.81) applied to the set of transverse momentum values given in Fig. 3.14. The results are shown in Fig. 3.15. These results are on average around 5-10% larger than similar results obtained in [29, 30, 31]. The discrepancy can be caused by multiple reasons, including the coarse range in $|\mathbf{q_T}|$ used to compute $\frac{dN}{dy}$, different boundaries for the Δy integration as well as a different averaging procedure to cope with the oscillating

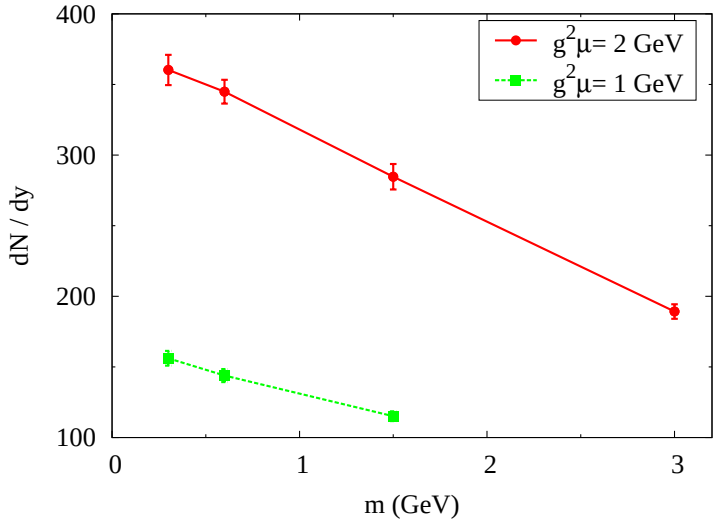

Figure 3.15: Total number of produced quark pairs per unit rapidity as a function of quark mass for $\tau = 0.25$ fm and different values of $g^2\mu$. The error bars are only statistical errors over different configurations of initial color charge.

quark production amplitude. The discrepancy is not a real problem, especially since the results computed in this model cannot be taken at face value. The results are meant to be a qualitative way to understand the initial stages of HIC.

3.6 Discussion and conclusion

Starting from the formalism described in [24, 25] for gluon field evolution and in [26] for solving the Dirac equation in the classical gluonic field, we implemented both algorithms numerically. We developed a new method for solving the nonlinear equation which gives the initial condition for the $SU(3)$ gluonic field (see Sec. 3.2).

We independently verified some of the numerical results for gluon production from [27] and most of the numerical results for quark production in [29, 30, 31]. We obtained the same number of quark pairs per unit of rapidity, even though the result is with $5-10\%$ larger than in [29, 30, 31]. This discrepancy is not worrisome because of two reasons. First, there are a lot of steps where small differences exist between us and Gelis *et al.* that could have a relatively large effect. Some of these reasons include the coarse range in $|\mathbf{q_T}|$ used to compute $\frac{dN}{dy}$ and different boundaries for the Δy integration in Eq. (3.78). Secondly, these results are meant to give a qualitative,

and not quantitative way to understand the initial stages of HIC.

The qualitative phenomenological implications of the results are as follows. Experiments at RHIC measured about 1000 particles per unit rapidity in the final state of the collision. Assuming entropy conservation, which is supported by the success of hydrodynamical calculations, leads to the existence of a similar number of particles also in the initial state [30]. The value of the μ parameter can be estimated using Eq. (2.30), which suggests that $\mu \approx 0.5$ GeV. Taking our results corresponding to $g^2\mu = 2$ GeV, for 3 quark flavors, we expect that the collision produces around 1000 quark pairs, result which is in contradiction with the RHIC observations. Moreover, this also raises questions about the assumption of gluon dominance in the initial stages of the collision.

Experimental results at RHIC suggest that the thermalization time is smaller than 1 fm [38]. If we suppose early chemical thermal equilibrium, than the quark pairs to gluons ratio is ≈ 1 [30]. For 1000 partons, this corresponds to about 400 gluons and 300 quark pairs. In our model, this is consistent with a reduced value of the saturation scale, corresponding to $g^2\mu \approx 1$ GeV. This is not unexpected, since Eq. (2.30) gives only a very crude estimate for the μ parameter.

The results show that within the classical model there are indeed a high number of produced quark-antiquark pairs, number which is close to the total number of gluons. These results suggest an early thermalization of the fireball. This is important since in the hydrodynamic models used to describe the evolution of the fireball one always assumes a medium in local kinetic thermal equilibrium. But this crucial assumption could not be proved because the processes involved in the early stages of the collision are clearly nonperturbative.

4

Photon production

In this section we present photon spectrum calculations within the CGC formalism, which is believed to describe the early stages of HIC. We start in Sec. 4.2 with a concise presentation of the theoretical framework and calculations of photon production [39, 40]. The photon rate is computed only to the leading order, since already such a calculation presents several challenges due to the strong gluonic background field.

The resulting expression is very complex and it cannot be computed numerically in the general form derived in [39, 40]. In Sec. 4.2.2, using symmetry arguments and properties of the CGC model, we argue for simplifications that make feasible the computation of the photon spectrum.

We conclude this chapter by looking at the numerical results for photon production. We do extensive tests to analyze the behavior of the numerical results on lattice size and other parameters of the numerical simulation. We end with the photon spectrum for one quark flavor with the mass $m = 0.3$ GeV in a background field characterized by $g^2\mu = 2$ GeV. We see that there are two terms that give non negligible contributions to the spectrum.

4.1 Introduction

As we discussed in the introductory part of this thesis, photon spectrum can be an important probe of nuclear collision. Photons, compared to quarks and gluons, interact with the fireball resulted in the collision only trough the electromagnetic interaction. Even at RHIC or LHC energies, the electromagnetic coupling constant is much smaller than the strong one (at RHIC energies $\alpha_{EM} \approx \frac{1}{137}$ while $\alpha_s \approx 0.12$). So,

compared to partons, photons, once produced, travel through the medium without additional rescattering until detection. But since the detector measures only the total flux of photon, it cannot distinguish between photons resulted from the different stages in HIC collision. So, to be able to use photons as a probe, one needs a good understanding of the photon production in all the HIC stages.

There are several papers that have analyzed photon production in HIC. For example, QGP photon rates were computed by treating the QGP as an expanding thermalized medium made from quarks and gluons [41, 42, 43, 44]. Other important photon production papers are [45, 46, 47] which develop the Arnold, Moore and Yaffe (AMY) formalism. The AMY formalism together with hydrodynamic evolution for the QGP are found in [48, 49] to give predictions in accordance with the experimental data.

In this section we will discuss photon production within the CGC formalism, which is believed to describe the classical gauge fields resulted in the earliest stages of the collision. The work presented here follows the guidelines from [39, 40]. Photon production in the CGC model was investigated for pA collisions in [50]. There the calculation is done perturbatively in one of the fields, which can be used to lineralize the Yang-Mills equations of motion. This is not the case for AA collisions, the ones we want to study, since both sources are strong. To overcome this problem, we sum over all the tree diagrams using the formalism developed in [22], which we than evaluate using numerical simulations.

4.2 General formulation

We want to compute photon production from a strong $SU(N_c)$ gauge theory. Since photons do not couple directly to gluons, we have to first consider the quarks produced by the gauge field, which then become sources for the photon field. This can be done by taking a combination of the QCD Lagrangian (given in Eq. (2.4)) and the QED Lagrangian. On top of this, we also have to add an additional term which is the source of the soft gluons within the CGC model. Hence our interactions are described by

the Lagrangian density:

$$\mathcal{L}(x) = -\frac{1}{4}G_{\mu\nu,a}(x)G_a^{\mu\nu}(x) + \bar{\Psi}(x)[i\not{D} - m]\Psi(x) - \frac{1}{4}F_{\mu\nu}(x)F^{\mu\nu}(x) + J_\mu(x)A^\mu(x)$$

where $G_{\mu\nu}(x)$ and $A_\mu(x)$ are the non-abelian field tensor and the gluonic gauge field (see Eq. (2.5)), while $F_{\mu\nu}$ is the electromagnetic field tensor given by:

$$F_{\mu\nu}(x) = \partial_\mu B_\nu(x) - \partial_\nu B_\mu(x) \tag{4.1}$$

with $B_\mu(x)$ the gauge field of the photon. $J_\mu(x)$ represents a current which is treated as a stochastic variable with Gaussian correlation in the MV model (see Sec. 2.2.3). The covariant derivative in the Lagrangian density is given by:

$$D_\mu = \partial_\mu - igA_\mu - ieB_\mu, \tag{4.2}$$

where we can neglect the last term both due to the smallness of the electromagnetic constant and due to a much higher number of gluons compared to photons characteristic to the early stages of HIC. Moreover, we specialize our computation for only one quark species, but it can be generalized to more than one.

The average number of produced photon is given by:

$$(2\pi)^3 2E_k \frac{dn}{d^3k} = \sum_\lambda \langle 0_{\text{in}}|b^{\lambda,\dagger}_{\text{out}}(k)b^\lambda_{\text{out}}(k)|0_{\text{in}}\rangle \tag{4.3}$$

where λ denotes the 2 photon polarizations and $b^\lambda_{\text{out}}(k)$, $b^{\lambda,\dagger}_{\text{out}}(k)$ are the creation and annihilation operators for the photon field. Using the LSZ reduction technique, Eq. (4.3) can be written as [39, 40]:

$$(2\pi)^3 2E_k \frac{dn}{d^3k} = P_{\mu\nu}(k)\frac{1}{\mathcal{Z}}\int d^4x d^4y e^{-ik\cdot(y-x)}\langle 0_{\text{in}}|J^\nu_{\text{el}}(y)J^\mu_{\text{el}}(x)|0_{\text{in}}\rangle \tag{4.4}$$

where $\mathcal{Z}$ is the photon wavefunction renormalization constant and:

$$P_{\mu\nu} = \sum_\lambda \epsilon^\lambda_\mu(k)\epsilon^{\lambda*}_\nu(k) \tag{4.5}$$

with $\epsilon^\lambda(k)$ the two polarizations vectors of the photon. With $J^\mu_{\text{el}}(x)$ we denoted the electromagnetic current given by:

$$J^\mu_{\text{el}}(x) = e\bar{\Psi}(x)\gamma^\mu\Psi(x) \tag{4.6}$$

where e denotes the electromagnetic coupling constant. So we see that the photon production rate reduces to computing a correlator of electromagnetic sources, and than taking its Fourier transform.

4.2.1 Leading order expression

Let us start by computing the electromagnetic source correlator using the lowest order approximation. Naively, the leading order approximation is given by:

$$\langle 0_{\rm in}|J^{\nu}_{\rm el}(y)J^{\mu}_{\rm el}(x)|0_{\rm in}\rangle = e^2\langle 0_{\rm in}|\bar{\Psi}_{\rm in}(y)\gamma^{\nu}\Psi_{\rm in}(y)\bar{\Psi}_{\rm in}(x)\gamma^{\mu}\Psi_{\rm in}(x)|0_{\rm in}\rangle \tag{4.7}$$

where $\Psi_{\rm in}(x)$ denotes the free fields at $t \to -\infty$. Using Wicks theorem and the definitions for the SK free propagators from Sec. 2.3, the above expression is reduced to [39, 40]:

$$\begin{aligned}\langle 0_{\rm in}|J^{\nu}_{\rm el}(y)J^{\mu}_{\rm el}(x)|0_{\rm in}\rangle =& -e^2\ {\rm Tr}[\gamma^{\mu}D^0_{+-}(x,y)\gamma^{\nu}D^0_{-+}(y,x)] \\ &+e^2\ {\rm Tr}[\gamma^{\mu}D^0_{++}(x,x)\gamma^{\nu}D^0_{--}(y,y)]\end{aligned} \tag{4.8}$$

where D^0 denotes the free fermion propagators defined in Eqs. (2.33)-(2.36). The above equation corresponds to the first two Feynman diagrams from Fig. 4.1. The two diagrams represent quark and antiquark pairs produced in a background field that radiate photons. There is another Feynman diagram that contributes to leading order (the right most diagram in Fig. 4.1). This corresponds to an initial quark/antiquark that propagates in the background field and emits photons. We drop the contribution of this diagram arguing that in a HIC the first two diagrams in Fig. 4.1 have the dominant contribution. The main difference between the two types of diagrams is that the first two have only gluons in the initial state, while the third also has a fermion. As we argued in Sec. 2.2, for small x the gluons are the dominant partons, hence we expect the first two diagrams to be present in much higher numbers than the third one. So, due to the sheer number of gluons compared to quarks, we can neglect the third diagram in Fig. 4.1.

So why did we call Eq. (4.8) the "naive" leading order approximation? In a strong gluonic background field, the non-abelian gauge field $A^{\mu}(x)$ is proportional to $\frac{1}{g}$, with

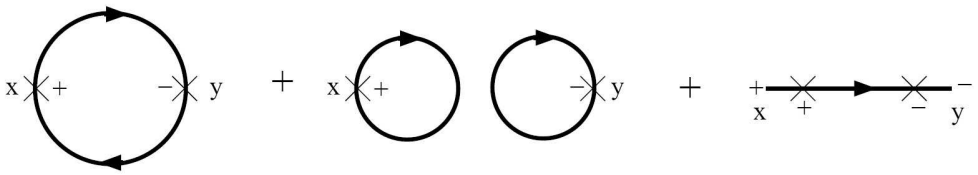

Figure 4.1: The Feynman diagrams which contribute to leading order for photon production [40]. The $\times$ symbol represents an insertion of the electromagnetic current while the $+$ and $-$ indices denote the two types of SK formalism vertices.

g the strong coupling constant. So an insertion of a gluonic line will contribute to leading order even though the coupling constant is small. Hence, to obtain the leading order approximation, we need to resum all the field insertions which contribute to $\mathcal{O}(1)$. There are two such types of contributions. The first is given by all gluon-gluon tree diagrams and gives rise to a resummed gauge field $A^\mu(x)$. The second are resummed gauge field insertions to the fermion propagator. This means that Eq. (4.8), which gives the first order contribution, should instead read:

$$\begin{aligned}\langle 0_{\rm in}|J^\nu_{\rm el}(y)J^\mu_{\rm el}(x)|0_{\rm in}\rangle =& -e^2\ {\rm Tr}[\gamma^\mu D_{+-}(x,y)\gamma^\nu D_{-+}(y,x)] \\ &+e^2\ {\rm Tr}[\gamma^\mu D_{++}(x,x)\gamma^\nu D_{--}(y,y)] \end{aligned} \tag{4.9}$$

with D the full quark propagator in the presence of the background gauge field. The full propagators are computed by solving the Lippmann-Schwinger equation (see Eq. (2.43)). As we saw in Sec. 2.3, the Lippmann-Schwinger equation is solved most easily in the RA basis. The solutions for the $D_{+-}(x,y)$ and $D_{-+}(x,y)$ propagators are given by Eqs. (2.52)-(2.53). To find the $D_{++}(x,x)$ and $D_{--}(x,x)$ propagators one uses that $D_{++}(x,x) = D_{--}(x,x)$ which applied to Eq. (2.41) gives:

$$D_{++}(x,x) = D_{--}(x,x) = \frac{1}{2}[D_{+-}(x,x) + D_{-+}(x,x)]. \tag{4.10}$$

Hence to compute Eq. (4.9) is enough to compute $D_{+-}(x,y)$ and $D_{-+}(x,y)$.

To do so we have to rewrite Eqs. (2.52)-(2.53) using that:

$$D^0_{+-}(z,z') = -\int \frac{d^4q}{(2\pi)^2} e^{iq\cdot(z-z')}\ \theta(q^0)2\pi\delta(q^2-m^2)(\not{q}-m) \tag{4.11}$$

$$D^0_{-+}(z,z') = \int \frac{d^4q}{(2\pi)^2} e^{-iq\cdot(z-z')}\ \theta(q^0)2\pi\delta(q^2-m^2)(\not{q}+m) \tag{4.12}$$

and also that $\not{q} + m = \sum_s u_s(q)\bar{u}_s(q)$ and $\not{q} - m = \sum_s v_s(q)\bar{v}_s(q)$ to obtain [39, 40]:

$$\begin{aligned} D_{+-}(x,y) =& -\sum_s \int \frac{d^4q}{(2\pi)^2} \int d^4z d^4z' \; \theta(q^0) 2\pi\delta(q^2 - m^2) \\ & \times [D_R (D_R^0)^{-1}](x,z) \; e^{iq\cdot z} v_s(q)\bar{v}_s(q) e^{-iq\cdot z'} \; [(D_A^0)^{-1} D_A](z',y) \quad (4.13) \\ D_{-+}(x,y) =& \sum_s \int \frac{d^4q}{(2\pi)^2} \int d^4z d^4z' \; \theta(q^0) 2\pi\delta(q^2 - m^2) \\ & \times [D_R (D_R^0)^{-1}](x,z) \; e^{-iq\cdot z} u_s(q)\bar{u}_s(q) e^{iq\cdot z'} \; [(D_A^0)^{-1} D_A](z',y) \quad (4.14) \end{aligned}$$

which can be simplified by using the notation [39, 40]:

$$\Psi^{(1)}_{q,s}(x) = \int d^4z \; [D_R (D_R^0)^{-1}](x,z) \; e^{-iq\cdot z} u_s(q) \quad (4.15)$$

$$\Psi^{(2)}_{q,s}(x) = \int d^4z \; [D_R (D_R^0)^{-1}](x,z) \; e^{iq\cdot z} v_s(q) \quad (4.16)$$

and that:

$$\begin{aligned} [D_R(x,z)(-i\overleftarrow{\not\partial}_z - m)u_s(q)]^\dagger \gamma^0 &= u_s^\dagger(q)(i\partial_z^\mu \gamma_\mu^\dagger - m)[D_R(x,z)]^\dagger \gamma^0 \\ &= u_s^\dagger(q)(i\partial_z^\mu \gamma_\mu^\dagger - m)[-\gamma^0 D_A(z,x)\gamma^0]\gamma^0 \\ &= -\bar{u}_s(q)(i\not\partial_z - m) D_A(z,x) \quad (4.17) \end{aligned}$$

(with a similar expression for $v_s(q)$) to finally obtain that:

$$D_{-+}(x,y) = \sum_s \int \frac{d^4q}{(2\pi)^2} \; \theta(q^0) 2\pi\delta(q^2 - m^2) \; \Psi^{(1)}_{q,s}(x) \bar{\Psi}^{(1)}_{q,s}(y) \quad (4.18)$$

$$D_{+-}(x,y) = -\sum_s \int \frac{d^4q}{(2\pi)^2} \; \theta(q^0) 2\pi\delta(q^2 - m^2) \; \Psi^{(2)}_{q,s}(x) \bar{\Psi}^{(2)}_{q,s}(y). \quad (4.19)$$

So computing the $D_{\pm\mp}(x,y)$ propagators reduces to computing the $\Psi^{(1),(2)}_{q,s}(x)$ expressions. To do so, we use the fact that the free Dirac plane waves are solutions of the Dirac equation, so:

$$[i\not\partial_z - m] \; u_s(q) e^{-iq\cdot z} = 0 \quad (4.20)$$

which when inserted into Eq. (4.15) gives:

$$\begin{aligned} \Psi^{(1)}_{q,s}(x) &= \int d^4z \; D_R(x,z)[-i\overleftarrow{\not\partial}_z - i\overrightarrow{\not\partial}_z] \; e^{-iq\cdot z} u_s(q) \\ &= -i \int d^4z \; \partial_z^\mu [D_R(x,z)\gamma_\mu e^{-iq\cdot z} u_s(q)] \quad (4.21) \end{aligned}$$

and similarly with:

$$\Psi^{(2)}_{q,s}(x) = -i \int d^4z \; \partial^\mu_z [D_R(x,z)\gamma_\mu e^{iq\cdot z} v_s(q)]. \tag{4.22}$$

This can be simplified further by using the identity [51]:

$$\lim_{t_1\to-\infty,\, t_2\to+\infty} \int_{t_1}^{t_2} dt \; \partial_t \int d^3\mathbf{x} F(\mathbf{x},t) = \left(\lim_{t\to+\infty} - \lim_{t\to-\infty}\right) \int d^3\mathbf{x} F(\mathbf{x},t) \tag{4.23}$$

which holds for any well behaved function $F(\mathbf{x},t)$. Assuming that the integrand in Eqs. (4.21)-(4.22) vanishes fast enough in space and also knowing the boundary condition $\lim_{y^0\to\infty} D_R(x,y) = 0$, we obtain:

$$\Psi^{(1)}_{q,s}(x) = i \lim_{z^0\to-\infty} \int d^3z \; D_R(x,z)\gamma^0 e^{-iq\cdot z} u_s(q) \tag{4.24}$$

$$\Psi^{(2)}_{q,s}(x) = i \lim_{z^0\to-\infty} \int d^3z \; D_R(x,z)\gamma^0 e^{iq\cdot z} v_s(q). \tag{4.25}$$

In the following we argue that the expressions given in Eqs. (4.24)-(4.25) are in fact solutions of the Dirac equation (this is why they are denoted with Ψ). Let us start from the Dirac equation in a background gluonic field and the corresponding equation for the retarded fermion propagator:

$$[i\not{\partial}_y - g\not{A} - m]\Psi(y) = 0 \tag{4.26}$$

$$D_R(x,y)[-i\overleftarrow{\not{\partial}}_y - g\not{A} - m] = \delta^4(x-y). \tag{4.27}$$

By multiplying Eq. (4.26) with $D_R(x,y)$ on the left and Eq. (4.27) with $\Psi(y)$ on the right, we obtain [39, 40]:

$$\Psi(x) = -i \int d^4y \partial^\mu_y [D_R(x,y)\gamma_\mu \Psi(y)]. \tag{4.28}$$

Now using Eq. (4.23), we finally obtain:

$$\Psi(x) = i \lim_{y^0\to-\infty} \int d^3y \; D_R(x,y)\gamma^0 \Psi(y). \tag{4.29}$$

This means that $\Psi(x)$ is the solution of the Dirac equation with the initial condition given by $\Psi(y)$ at $y^0 \to -\infty$.

When applying Eq. (4.29) to Eqs. (4.24)-(4.25) it is straightforward to see that $\Psi^{(1)}_{q,s}$ and $\Psi^{(2)}_{q,s}$ are Dirac wavefunctions corresponding to initial conditions at $t \to -\infty$

given by a free quark wavefunction ($e^{-iq\cdot y}u_s(q)$) and by a free antiquark wavefunction ($e^{iq\cdot y}v_s(q)$) respectively.

Finally, summing everything together, we obtain that the photon production rate given by Eq. (4.4) can be written using Eqs. (4.18)-(4.19) as [39, 40]:

$$\begin{aligned}(2\pi)^3 2E_k\frac{dn}{d^3k} =& P_{\mu\nu}(k)\frac{e^2}{\mathcal{Z}}\int d^4x d^4y e^{-ik\cdot(y-x)}\sum_{s_1,s_2}\int\frac{d^3q_1}{(2\pi)^3 2E_{q_1}}\frac{d^3q_2}{(2\pi)^3 2E_{q_2}}\\ &\times\Big\{\ \mathrm{Tr}[\gamma^\mu\Psi^{(1)}_{q_1,s_1}(x)\bar\Psi^{(1)}_{q_1,s_1}(y)\gamma^\nu\Psi^{(2)}_{q_2,s_2}(y)\bar\Psi^{(2)}_{q_2,s_2}(x)]\\ &\quad+\frac{1}{4}\ \mathrm{Tr}[\gamma^\mu\Psi^{(1)}_{q_1,s_1}(x)\bar\Psi^{(1)}_{q_1,s_1}(x)-\gamma^\mu\Psi^{(2)}_{q_1,s_1}(x)\bar\Psi^{(2)}_{q_1,s_1}(x)]\\ &\quad\times\ \mathrm{Tr}[\gamma^\nu\Psi^{(1)}_{q_2,s_2}(y)\bar\Psi^{(1)}_{q_2,s_2}(y)-\gamma^\nu\Psi^{(2)}_{q_2,s_2}(y)\bar\Psi^{(2)}_{q_2,s_2}(y)]\Big\}\end{aligned}\tag{4.30}$$

4.2.2 Photon rate within CGC formalism

The photon production rate given in Eq. (4.30) poses a few challenges in a numerical computation. The main one is given by the large number of integrals, 8 spatial ones and 6 in momentum space. This makes any numerical method for computing the photon production rate very computationally time intensive. So the first step is to find a simpler form for Eq. (4.30), a form that is much easier to implement numerically.

The first observation is that the photon production rate is independent on the spin of the quarks. This means that the sum over spins for the third and fourth lines of Eq. (4.30) can be easily done to obtain a factor of 2 from each line, such that in total the sum over spins cancels the $\frac{1}{4}$ factor. For the second line of Eq. (4.30) we can sum over only one of the spins (lets say s_1) to get a factor of 2. We still have to keep $\sum_{s_2}$ since one computes the superposition between a quark and an antiquark wavefunction. This depends on the spin difference between the two particles, but not on the sum of those two spins.

The next simplification results from using the notations:

$${}_1\lambda^\mu_{q_1,\,q_2s_2}(k) = \int d^4x\ e^{ik\cdot x}\ \bar\Psi^{(2)}_{q_2,s_2}(x)\gamma^\mu\Psi^{(1)}_{q_1}(x)\tag{4.31}$$

$${}_2\lambda^\mu_{q_1}(k) = \int d^4x\ e^{ik\cdot x}\ \left[\bar\Psi^{(1)}_{q_1}(x)\gamma^\mu\Psi^{(1)}_{q_1}(x)-\bar\Psi^{(2)}_{q_1}(x)\gamma^\mu\Psi^{(2)}_{q_1}(x)\right]\tag{4.32}$$

where ${}_1\lambda^\mu_{q_1,\,q_2s_2}(k)$ and ${}_2\lambda^\mu_{q_1}(k)$ are just numbers since one sums over the Dirac and

color indices. Using these notations, Eq. (4.30) simplifies to:

$$(2\pi)^3 2E_k \frac{dn}{d^3k} = P_{\mu\nu}(k)\frac{e^2}{\mathcal{Z}} \int \frac{d^3q_1}{(2\pi)^3 2E_{q_1}} \frac{d^3q_2}{(2\pi)^3 2E_{q_2}} \times \left\{ 2\sum_{s_2} {}_1\lambda^{\mu}_{q_1,\, q_2 s_2}(k) \left[{}_1\lambda^{\nu}_{q_1,\, q_2 s_2}(k)\right]^* + {}_2\lambda^{\mu}_{q_1} \left[{}_2\lambda^{\nu}_{q_2}\right]^* \right\}. \quad (4.33)$$

The polarization term $P^{\mu\nu}$ can also be used to simplify the calculation. Photons have only transverse polarization, which means that $k_\mu P^{\mu\nu} = 0$. This requirement can be fulfilled if the photon polarizations are chosen such that $\epsilon_\lambda = (0, \vec{\epsilon}_\lambda)$ with $\vec{\epsilon}_\lambda \cdot \vec{k} = 0$ [8]. Hence we have to compute only the spatial components of ${}_1\lambda$ and ${}_2\lambda$. Moreover, since we compute the photon rate only to leading order, the photon wavefunction normalization constant is $\mathcal{Z} = 1$.

Another important simplification results because the background gluonic field is boost invariant (see Sec. 3.1). This makes the photon spectrum in this model also boost invariant. Moreover, because of the boost invariance of the background gluonic field, one of the two rapidity integrals in Eq. (4.33) can be computed analytically. This is the case since the result should depend only on the rapidity sum for the first term in Eq. (4.33) and on the rapidity difference for the second term in Eq. (4.33)[1].

Before summing all up, it is convenient to use the notations:

$${}_1\Lambda_{\mathbf{q_{T1}},\, \mathbf{q_{T2}} y_2}(k) = P_{ij} \sum_{s_2} {}_1\lambda^{i}_{\mathbf{q_{T1}} y_1,\, \mathbf{q_{T2}} y_2 s_2}(k) \left[{}_1\lambda^{j}_{\mathbf{q_{T1}} y_1,\, \mathbf{q_{T2}} y_2 s_2}(k)\right]^* \Big|_{y_1=0} \quad (4.34)$$

$${}_2\Lambda_{\mathbf{q_{T1}},\, \mathbf{q_{T2}} y_2}(k) = P_{ij}\, {}_2\lambda^{i}_{\mathbf{q_{T1}} y_1}(k) \left[{}_2\lambda^{j}_{\mathbf{q_{T2}} y_2}(k)\right]^* \Big|_{y_1=0} \quad (4.35)$$

with i, j running from 1 to 3 and with $y_{1,2}$ denoting the rapidity corresponding to the 4-momentum $q_{1,2}$ in Eq. (4.33). With $\mathbf{q_T}$ we denote the transverse momentum vector. Now Eq. (4.33) simplifies even further to:

$$(2\pi)^3 2E_k \frac{dn}{d^3k} = \frac{e^2}{16\pi^2} \int \frac{d^2\mathbf{q_{T1}}}{(2\pi)^2} \frac{d^2\mathbf{q_{T2}}}{(2\pi)^2} \int_{-2y_{max}}^{2y_{max}} dy_2\, (2y_{max} - |y_2|) \times \left[2\, {}_1\Lambda_{\mathbf{q_{T1}},\, \mathbf{q_{T2}} y_2}(k) + {}_2\Lambda_{\mathbf{q_{T1}},\, \mathbf{q_{T2}} y_2}(k)\right] \quad (4.36)$$

[1]The difference between the two cases arises since for the first term in Eq. (4.30) we project a fermion wavefunction onto the wavefunction of its antiparticle while for the first term in Eq. (4.30) we project a fermion wavefunction onto itself.

where y_{max} denotes the integration limits over the fermion's rapidity interval, i.e. $\int_{-y_{max}}^{y_{max}} dy$. To obtain Eq. (4.36) we computed analytically the $y_1 - y_2$ integral for the ${}_1\Lambda(k)$ term. As we argued above, due to boost invariance of the background field, the ${}_1\Lambda(k)$ term should depend only on $y_1 + y_2$ but not on $y_1 - y_2$. The next step to obtain Eq. (4.36) is to replace the remaining $y_1 + y_2$ integral[1] with a y_2 only integral computed for $y_1 = 0$. For the ${}_2\Lambda(k)$ term we did a similar computation. In this case we analytically computed the $y_1 + y_2$ integral and than we replaced the remaining $y_1 - y_2$ integral with a y_2 only integral at $y_1 = 0$.

Even though Eq. (4.36) looks much simpler, there are still 4 integrals over the transverse momenta of the initial quark and antiquark. For the second term in Eq. (4.36) this is not such a great problem, since one needs to compute only a two dimensional transverse momentum integral of the ${}_1\lambda_{q_1}$ term (see Eq. (4.33)). This then can be squared to obtain the total contribution of the second term to the photon production rate. The problem is different for the first term from Eq. (4.36), since no similar solution can be applied. But the 4 dimensional transverse momentum integrals can still be simplified by using that the initial color charge configuration is given by a random distribution in the transverse plane. Thus, as long as we average over a large enough number of configurations of initial charge, there is no preferred transverse direction. So the 4 transverse momentum integrals reduce to 3 integrals[2]. When taking this into consideration, the transverse spectrum of photons becomes:

$$\begin{aligned}\frac{dn}{dy\, d^2k_T} =& \frac{\alpha_{_{EM}}}{4(2\pi)^4} \int \frac{q_{T1}\, dq_{T1}}{2\pi} \frac{d^2\mathbf{q_{T2}}}{(2\pi)^2} \int_{-2y_{max}}^{2y_{max}} dy_2\, (2y_{max} - |y_2|) \\ & \times \left[2\, {}_1\Lambda_{q_{T1},\, \mathbf{q_{T2}} y_2}(k) + {}_2\Lambda_{q_{T1},\, \mathbf{q_{T2}} y_2}(k)\right] \end{aligned} \tag{4.37}$$

where $\alpha_{_{EM}} = \frac{e^2}{4\pi}$ is the electromagnetic constant and q_{T1} represents the magnitude of the transverse momentum $\mathbf{q_{T1}}$.

[1] Since both the quark and antiquark rapidity vary between $-y_{max}$ to y_{max}, the rapidity sum/difference varies between $-2y_{max}$ to $2y_{max}$ (hence the integration limits over rapidity in Eq. (4.36)).

[2] The same reasoning also holds for the second term in Eq. (4.36), but as we argued above, this simplification is not needed since there is an easier way to compute the contribution of this term.

4.3 Numerical results

The parameters of the numerical model are, as in the case of quark production, the quark mass m, the strong coupling constant g, the physical area of the system πR_A^2 and the average density of charge fluctuations squared μ. On top of these, an additional parameter is the electromagnetic constant $\alpha_{_{EM}}$, whose only influence is to rescale the photon spectrum. For the numerical simulations presented here we take $g = 2$, $\alpha_{_{EM}} = \frac{1}{137}$, $\pi R_A^2 = 141$ fm^2, $m = 0.3$ GeV and $\mu = 0.5$ GeV. Also, all the results presented are computed for mid-rapidity photons ($y_\gamma = 0$), unless stated otherwise.

As for the quark pair production calculations, we consider a $N^2 N_z = 180^2 \times 400$ lattice with transverse lattice spacing $a = \sqrt{\frac{\pi R_A^2}{N^2}}$, longitudinal lattice spacing $a_z = 0.2\ a$ and time step $a_\tau = 0.02\ a$.

4.3.1 Numerical tests

In this section we analyze the dependence of the numerical results on different parameter values. In this case we plot all our results in lattice units since the important part is to compare between different numerical results and not to compare with experimental data.

The first important test is the dependence of the numerical results on the transverse lattice size. In Sec. 3.5.1, we observed that gluon multiplicity at high transverse momentum is strongly dependent on the transverse lattice size (see Fig. 3.3). The left panel in Fig. 4.2 shows a typical contribution to the photon spectrum for a given pair of ($\mathbf{q_{T1}}$,$\mathbf{q_{T2}}$) initial fermionic transverse momenta. As expected, the spectrum at high $\mathbf{k_T}$ (photon transverse momentum) does depend on the transverse lattice size. For a $N^2 = 180$ transverse lattice, we expect to have lattice size distortions of the spectrum only for momenta larger than 4 GeV (see left panel in Fig. 4.2). Thus we limit our photon spectrum calculations to $k_T \leq 4$ GeV . We will discuss at length the large single point peak later on.

Due to computational time limitations, we averaged the numerical results only

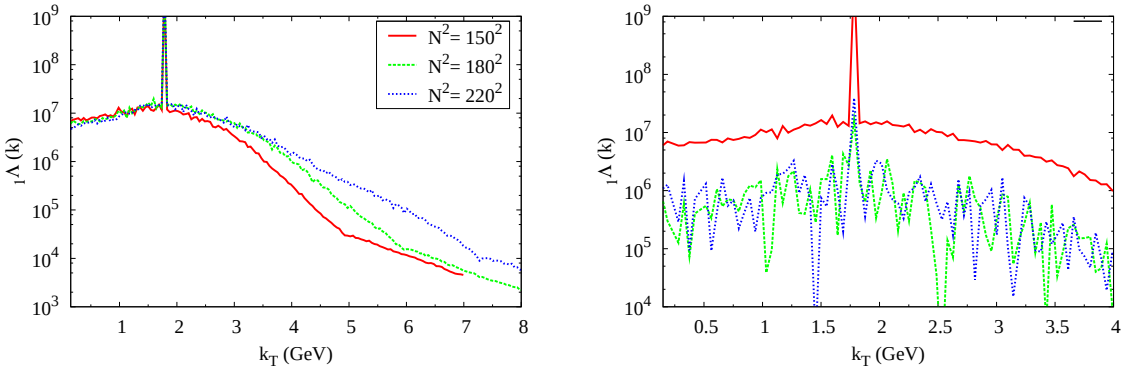

Figure 4.2: Left: The $_1\Lambda(k)$ term for different sizes of the transverse lattice. Right: The $_1\Lambda(k)$ term for different configurations of initial color charge. All results are averaged over 5 different configurations of color charge. Two of the numerical results plotted in the right panel show only the difference from the "standard" result (see text for additional details).

over 5 different configurations of initial color charge. To get an estimation of the statistical error, we compared results for the same values of the parameters, but averaged over different initial charge configurations (see the right panel in Fig. 4.2). The numerical simulations show that by averaging only over 5 charge configurations we have a statistical error around 10-15%. This can be seen from the right panel in Fig. 4.2, where the relative differences between values of $_1\Lambda(k)$ obtained for different charge configurations are under 15%.

Comparing results for different parameter values can be tricky since the difference is difficult to estimate from logarithmic scale plots with a wide vertical range. To overcome this problem, we plot one of the results (which we call "standard") while for the rest we plot only the difference from the "standard" one. This type of plots are denoted with a † symbol in the legend (see Figs. 4.3 and 4.4).

The numerical algorithm for the time evolution of the Dirac wavefunction (see Sec. 3.4.1) needs to store the two components $\Psi^\pm$ of the Dirac field at different time steps. But Eqs. (4.31)-(4.32), which give the values of $_1\lambda$ and $_2\lambda$ and implicitly the photon rate, are defined for $\Psi^\pm$ at the same time step. To overcome this problem we can bring both $\Psi^\pm$ components to the same time step or we can take the time step a_τ small enough such that even though $\Psi^\pm$ are known at different steps, this does not affect significantly the photon production rate. We choose the second option since it

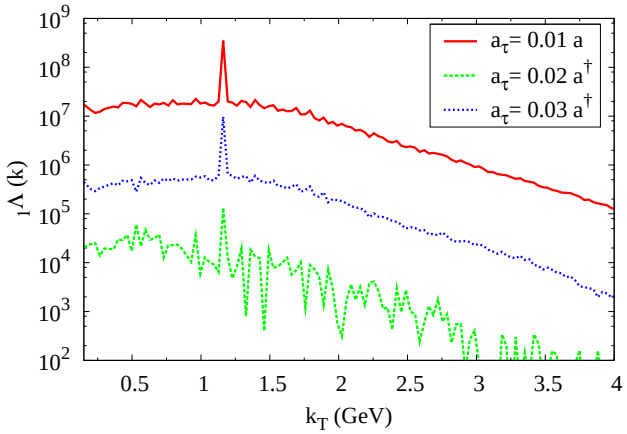

Figure 4.3: The ${}_1\Lambda(k)$ term for different values of the time step size. † We plotted only the difference from the "standard" result (see text for additional details).

minimizes both the memory requirements and the computational time. In Fig. 4.3 we compare a typical ${}_1\Lambda(k)$ contribution to the photon spectrum computed for different time step sizes. We observe that even for $a_\tau = 0.03a$, the numerical error due to the finite time step size is much smaller than other statistical and systematic errors (see Figs. 4.2 and 4.4).

In Sec. 3.5.3, we obtained that the quark pair production amplitude does vary quite strongly with the longitudinal lattice size and lattice spacing (especially for small quark masses and small longitudinal lattice $N_z \lesssim 400$). We attributed this problem to the oscillation of the longitudinal z integral on the integration boundaries which are the two lattice endpoints. When computing the photon spectrum we have a similar problem, since for example Eq. (4.31), when written in $(\tau, z, \mathbf{x_T})$ coordinates, it reads:

$$
\begin{aligned}
{}_1\lambda^{\mu}_{q_1,\, q_2 s_2}(y_\gamma, \mathbf{k_T}) = \int d\tau \int_{-z_M}^{z_M} \frac{\tau dz}{\sqrt{\tau^2+z^2}}\, e^{ik_T(\sqrt{\tau^2+z^2}\cosh y_\gamma - z\sinh y_\gamma)} \\
\times \int d^2\mathbf{x_T} e^{-i\mathbf{k_T}\cdot\mathbf{x_T}}\ \bar{\Psi}^{(2)}_{q_2,s_2}(\tau, z, \mathbf{x_T})\gamma^\mu \Psi^{(1)}_{q_1}(\tau, z, \mathbf{x_T}) \qquad (4.38)
\end{aligned}
$$

where with y_γ and $\mathbf{k_T}$ we denoted the photon rapidity and transverse momentum respectively. We expect the above expression to be a highly oscillatory function of the longitudinal integration boundary z_M. To overcome this problem, we compute Eq. (4.38) for different limits of the z integration, after which we take an average of all

these results[1]. The results presented here are an average over z_M values from $\frac{3}{4}z_{max}$ to z_{max} (with $2z_{max}$ the longitudinal lattice extension). To be able to get a precise result for Eq. (4.38) the averaging interval over z_M has to have several periods of oscillation. The variation of ${}_1\Lambda(k)$ with the size[2] of the longitudinal averaging interval is given in the left panel in Fig. 4.4. From there we can see that different sizes for the averaging

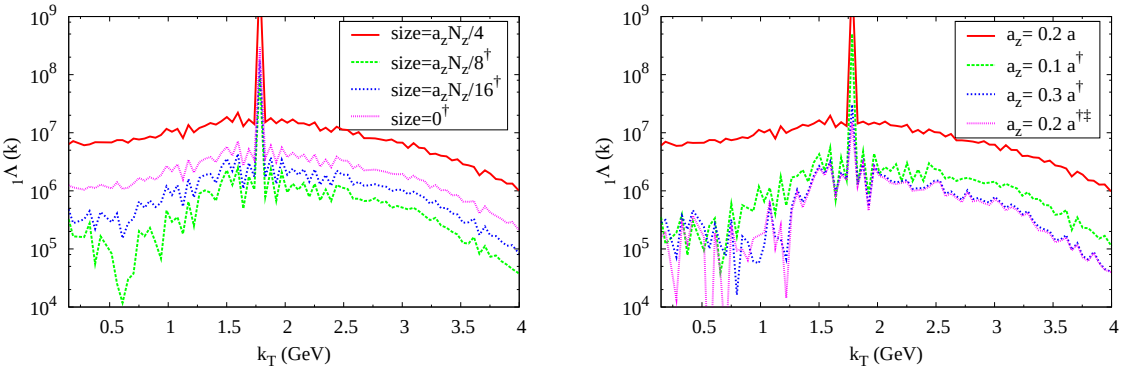

Figure 4.4: Left: The ${}_1\Lambda(k)$ term for different limits of the averaging procedure for the longitudinal spatial integral. Right: The ${}_1\Lambda(k)$ term for different longitudinal lattice spacings. † We plotted only the difference from the "standard" result (see text for additional details). ‡ Result obtained for a longitudinal lattice size $N_z = 600$.

interval give results up to 10% different. This is expected since our longitudinal lattice is not large enough for the averaging interval to contain several oscillation periods of the function given in Eq. (4.38). This problem becomes less important as we study larger quark masses, such that for $m \geq 1$ GeV this difference becomes negligible. This dependence of the result on lattice size can be removed by taking the continuum limit of the numerical results.

We also studied the behavior of our numerical results on the longitudinal lattice spacing a_z. From the right panel in Fig. 4.4 we observe that changing a_z results in about 10% relative difference, but this is due to changing the maximum lattice

[1]This is the same method that was used for quark pair production computation. For more details about the method see Sec. 3.5.2.

[2]We define the size of the longitudinal averaging interval as $z_M^{maximum} - z_M^{minimum}$, where we always take $z_M^{maximum} = z_{max}$. A larger value for "size" means we averaged over more longitudinal lattice points.

extension[1]. The discretization errors due to a_z are minimal as can be observed by comparing the two lowest most curves in the right panel of Fig. 4.4. Both curves are obtained for the same lattice extension $z_{max} = 60a$, but in one we have $a_z = 0.3a$ and $N_z = 400$ while in the other we have $a_z = 0.2a$ and $N_z = 600$.

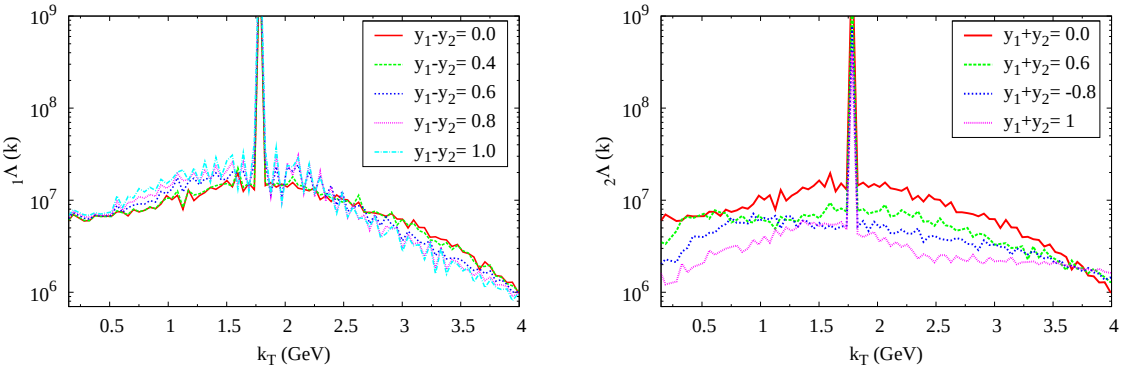

Figure 4.5: Left: The dependence of the ${}_1\Lambda(k)$ term on the quark rapidity y_1 and antiquark rapidity y_2 when $y_1 + y_2 = 0$. Right: The dependence of the ${}_1\Lambda(k)$ term on the quark rapidity y_1 and antiquark rapidity y_2 when $y_1 - y_2 = 0$

In Fig. 4.5 we have ${}_1\Lambda(k)$ for different quark and antiquark rapidities. We see that, up to numerical errors (compare to Fig. 4.8), ${}_1\Lambda(k)$ is independent on the rapidity difference between the quark and antiquark. But ${}_1\Lambda(k)$ does depend on rapidity sum of the quark rapidity y_1 and antiquark rapidity y_2, as can be seen in the right panel in Fig. 4.5. A larger $y_1 + y_2$ value makes the spectrum smaller and flatter.

We observed that the second term in Eq. (4.36) gives a negligible contribution to our numerical results. The ${}_2\Lambda(k)$ term, for a given pair of transverse momenta $(\mathbf{q_{T1}}, \mathbf{q_{T2}})$, has a similar contribution (in absolute value) to ${}_1\Lambda(k)$ for the same transverse momenta. But since the ${}_2\Lambda(k)$ term can have both positive and negative values, the sum ${}_2\Lambda_{\mathbf{q_{T1}},\,\mathbf{q_{T2}}} + {}_2\Lambda_{\mathbf{q_{T1}},\,-\mathbf{q_{T2}}}$ is more than 2 orders of magnitude smaller than just ${}_2\Lambda_{\mathbf{q_{T1}},\,\mathbf{q_{T2}}}$ (see the left panel in Fig. 4.6). Because of this reason, the contribution of the second term in Eq. (4.36) can be neglected when compared to the contribution of the first term (see the right panel in Fig. 4.6).

It may be that the second term in Eq. (4.36) brings no contribution at all to the

[1]Since in our implementation a_z is given as a function of the transverse lattice spacing, when changing a_z we also change the longitudinal extension $2z_{max}$ of the lattice.

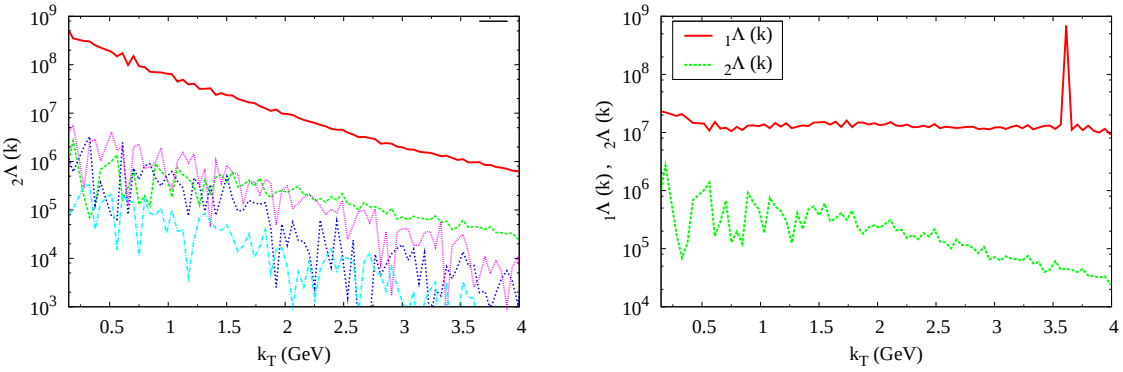

Figure 4.6: Left: The upper curve gives ${}_2\Lambda(k)$ for a given pair of transverse momenta $(\mathbf{q_{T1}}, \mathbf{q_{T2}})$. The lower curves give the sum of two ${}_2\Lambda(k)$ terms corresponding to the pairs $(\mathbf{q_{T1}}, \mathbf{q_{T2}})$ and $(\mathbf{q_{T1}}, -\mathbf{q_{T2}})$ for different $\mathbf{q_{T2}}$. The sum of the two contributions is 2 orders of magnitude smaller than one of the contributions. Right: Comparing the contributions to the photon rate given by the ${}_1\Lambda(k)$ and ${}_2\Lambda(k)$ terms for the same pairs of transverse momenta $(\mathbf{q_{T1}}, \mathbf{q_{T2}})$. The upper curve is $2({}_1\Lambda_{\mathbf{q_{T1}}, \mathbf{q_{T2}}} + {}_1\Lambda_{\mathbf{q_{T1}}, -\mathbf{q_{T2}}})$ while the lower curves is ${}_2\Lambda_{\mathbf{q_{T1}}, \mathbf{q_{T2}}} + {}_2\Lambda_{\mathbf{q_{T1}}, -\mathbf{q_{T2}}}$. The factor of 2 arises since ${}_1\Lambda$ has a twice as large contribution to the photon rate than ${}_2\Lambda$ (see Eq. (4.36)).

photon production rate. This is the case if the vacuum of the theory is invariant under charge conjugation[1]. The difficulty arises since the vacuum is not that of a free theory due to the background gluonic field. Some of the Feynman diagrams which give the resummed second diagram from Fig. 4.1 can be easily shown to be identically 0. For example the second diagram from Fig. 4.1 with no gluon insertion is 0 due to Furry's theorem, the same diagram with one gluon insertion is 0 since its contribution is proportional to $\mathrm{Tr}[t_a] = 0$ while the diagram with two gluon insertions is again 0 since is proportional to $2\ \mathrm{Tr}[t_a t_b] = \delta_{ab}$ times the QED tadpole diagram (which is 0 due to Furry's theorem). For some other diagrams, if it is indeed the case, the calculations to show that they are 0 are more involved. And the rest of these diagrams cannot be neglected since they also contribute to leading order. Numerically we cannot show that the contribution of the second diagram in Fig. 4.1 is 0 since we do not expect to have a precision higher than 2 decimal digits.

Fig. 4.7 shows the typical contributions to the photon spectrum given by different fermion transverse momenta. The contributions vary on a wide range, with the small transverse momenta having an individual contribution more than two orders of

[1]If the vacuum is invariant under charge conjugation, than according to Furry's theorem, the second diagram in Fig. 4.1 is 0.

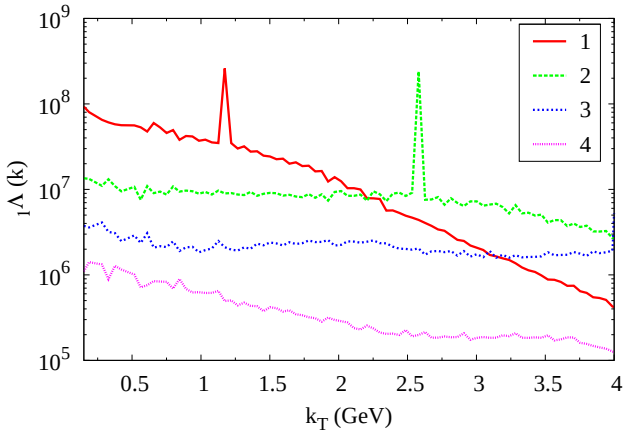

Figure 4.7: The ${}_1\Lambda(k)$ contribution to the photon spectrum for different quark and antiquark initial momenta. The curve are ordered in increasing fermion transverse momenta, such that the curve labeled with 1 gives ${}_1\Lambda(k)$ for small fermion transverse momenta while the curve labeled with 4 gives ${}_1\Lambda(k)$ for large fermion transverse momenta.

magnitude larger than the one rising from large fermion transverse momenta.

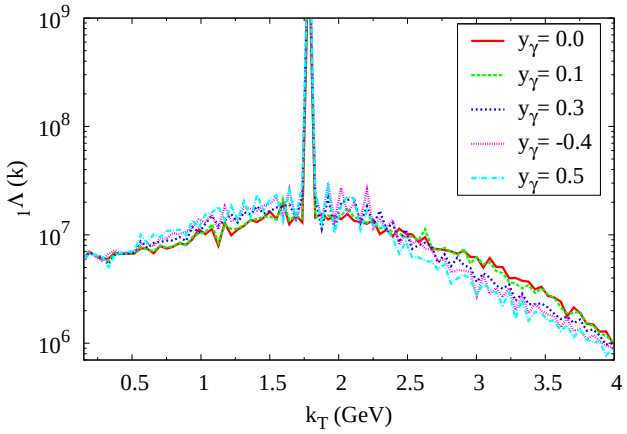

Figure 4.8: The ${}_1\Lambda(k)$ contribution to the photon spectrum for different photon rapidities y_γ.

Due to gluonic field boost invariance, we expect that the photon spectrum is rapidity invariant. This is not automatically satisfied by our numerical code since we use z as the longitudinal variable. Fig. 4.8 shows that indeed, up to numerical errors, the photon spectrum does not depend on photon rapidity.

We still have to discuss about the peak structure in the function ${}_1\Lambda(k)$ (see for example Fig. 4.7). For a pair of fermion transverse momenta $(\mathbf{q_{T1}}, \mathbf{q_{T2}})$, the peak is located at photon momentum $\mathbf{k_T} = (q_{x1} + q_{x2}, q_{y1} + q_{y2})$ and has a height 10^3 to

10^5 times larger that the rest of the ${}_1\Lambda(k)$ values. The peak is not a product of the numerical calculations, but is given by the form of the initial condition for the quark/antiquark wavefunction at $\tau = 0$ (see Eq. (3.37)). Let us analyze this in more details, to better understand what gives rise to the peak. Eq. (3.37) for a quark can be schematically represented as:

$$\Psi^{(1)}_{q_1}(\tau = 0, z, \mathbf{x_T}) = [\dots] \;\; e^{i\mathbf{q_T}\cdot\mathbf{x_T}} \; u(q) \tag{4.39}$$

with a very similar expression for an antiquark. With $[\dots]$ we denoted a complicated matrix structure whose exact expression is not important for a qualitative discussion. At a later time τ, $\Psi^{(1)}_{q_1}(\tau, z, \mathbf{x_T})$ will have a similar form as in Eq. (4.39), just that the matrix denoted by $[\dots]$ will have another form due to time evolution. Now, when computing ${}_1\lambda$ defined in Eq. (4.31), we obtain:

$$\begin{aligned} {}_1\lambda^{\mu}_{q_1,\, q_2 s_2} &= \int d^4x \; e^{ik\cdot x} \; \bar{\Psi}^{(2)}_{q_2,s_2}(x)\gamma^{\mu}\Psi^{(1)}_{q_1}(x) \\ &\propto \int d^4x \; e^{-i(\mathbf{k_T}-\mathbf{q_{T1}}-\mathbf{q_{T2}})\cdot\mathbf{x_T}} \;\; [\dots](\tau, z, \mathbf{x_T}) \end{aligned} \tag{4.40}$$

where in $[\dots](\tau, z, \mathbf{x_T})$ we incorporated all the terms that do not play an important role in our qualitative analysis. We do not expect $[\dots](\tau, z, \mathbf{x_T})$ to have a strong behavior on the transverse coordinate, so the above expression should have a large peak at $\mathbf{k_T} = \mathbf{q_{T1}} + \mathbf{q_{T2}}$. This peak is a smeared down delta function. Similarly, when computing ${}_2\lambda$ defined in Eq. (4.32), we obtain:

$$\begin{aligned} {}_2\lambda^{\mu}_{q_1} &= \int d^4x \; e^{ik\cdot x} \;\; \left[\bar{\Psi}^{(1)}_{q_1}(x)\gamma^{\mu}\Psi^{(1)}_{q_1}(x) - \bar{\Psi}^{(2)}_{q_1}(x)\gamma^{\mu}\Psi^{(2)}_{q_1}(x)\right] \\ &\propto \int d^4x \; e^{-i\mathbf{k_T}\cdot\mathbf{x_T}} \;\; [\dots](\tau, z, \mathbf{x_T}) \end{aligned} \tag{4.41}$$

thus ${}_2\lambda$ (and implicitly ${}_2\Lambda$) has a large peak only at $\mathbf{k_T} = 0$.

The $\mathbf{k_T} = 0$ peak in ${}_2\Lambda$ can be dealt with easily, by not computing the spectrum at $\mathbf{k_T} = 0$. For ${}_1\Lambda$, since the peak shifts positions with $\mathbf{q_{T1}} + \mathbf{q_{T2}}$, we have to develop a procedure to compute the contribution of the peaks to the final photon rate. The first step consists of reading the value of the peak, which is just the value of ${}_1\Lambda(k)$ at $\mathbf{k_T} = \mathbf{q_{T1}} + \mathbf{q_{T2}}$ since the peak is several orders of magnitude higher than the rest of the ${}_1\Lambda(k)$ values.

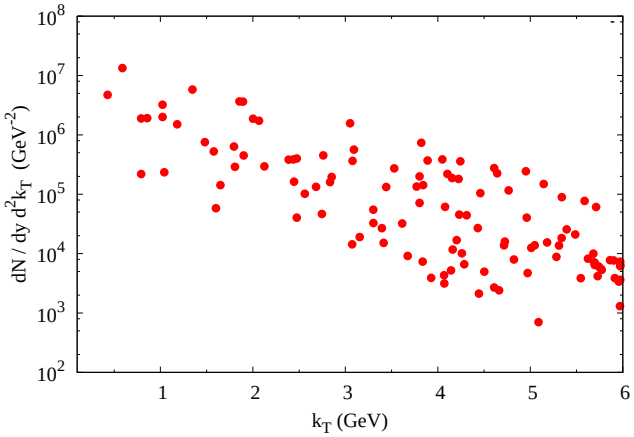

Figure 4.9: The dependence of the ${}_1\Lambda(k)$ peaks on photon transverse momentum for a set of 140 different $(\mathbf{q_{T1}}, \mathbf{q_{T2}})$ pairs. The ${}_1\Lambda(k)$ peaks plotted here are multiplied by Eq. (4.42) (see text for details).

The next step is to identify what is the overall contribution of such a peak to the final photon spectrum. For a given $\mathbf{k_T} = \frac{2\pi}{Na}(n_x, n_y)$ with $n_{x,y} = -\frac{N}{2}+1, \ldots, \frac{N}{2}$ there are $4(\frac{N}{2} - n_x)(\frac{N}{2} - n_y)$[1] different $(\mathbf{q_{T1}}, \mathbf{q_{T2}})$ pairs that satisfy $\mathbf{k_T} = \mathbf{q_{T1}} + \mathbf{q_{T2}}$. So the total fraction of fermion transverse states that give a peak at $\mathbf{k_T} = \frac{2\pi}{Na}(n_x, n_y)$ is given by:

$$\left(\frac{1}{N}\right)^4 4(\frac{N}{2} - n_x)(\frac{N}{2} - n_y). \tag{4.42}$$

The contribution of the peaks to the photon spectrum is given by Eq. (4.42) multiplied with the average value of the ${}_1\Lambda$ peak height at $\mathbf{k_T}$. This contribution for a large set of fermion transverse momenta is shown in Fig. 4.9. We see that for a given k_T value, the peaks heights vary by up to 2 orders of magnitude. Moreover we also see a dependence of the peak heights on the photon transverse momentum, dependence that will be analyzed in more detail in the next section.

4.3.2 Numerical results for photon spectrum

To compute the photon spectrum we have to sum ${}_1\Lambda(k)$ over all the initial transverse momenta of the quark and antiquark and integrate over the rapidity of one of the

[1]The equation $n = n_1 + n_2$ with $n = -\frac{N}{2}+1, \ldots, \frac{N}{2}$ and $n_{1,2} = -\frac{N}{4}, \ldots, \frac{N}{4}$ has $2(\frac{N}{2} - n)$ solutions for n odd and $2(\frac{N}{2} - n) + 1$ solutions for n even. To keep the notation simple we take that there are only $2(\frac{N}{2} - n)$ solutions.

fermions. Hence we need to calculate a five dimensional integral (which reduces to only a four dimensional integral if we take into consideration that the transverse plane has no preferred direction - see Sec. 4.2.2). We choose to compute the five dimensional integral using a Monte Carlo algorithm. We randomly generate a set of transverse momenta and quark rapidity, and for each element in that set we compute the contribution it brings to the photon spectrum. The final photon spectrum is given by the average of the contributions given by each element in the set.

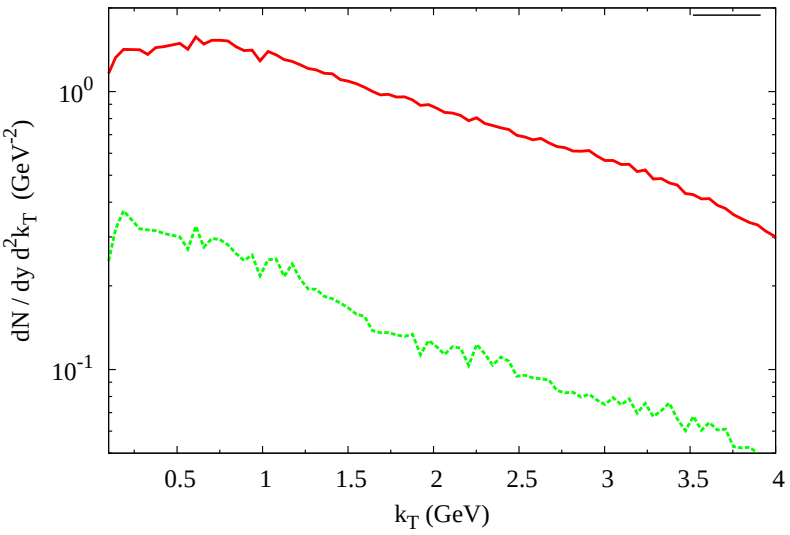

Figure 4.10: The upper curve gives the ${}_1\Lambda$ contribution to the photon spectrum of the first term after removing the peaks. The lower curve gives a statistical error estimate for the Monte Carlo method use to compute the multidimensional integral.

The result of the Monte Carlo method is independent on whether we compute the photon spectrum using a five dimensional integral (see Eq. (4.36)) or using a four dimensional integral (see Eq. (4.37)). The only difference between the two cases consists in the probability distribution that we use to generate the set of transverse momenta and quark rapidity values. The probability distribution has to be proportional to the density of states in the phase space $(\mathbf{q_{T1}}, \mathbf{q_{T2}}, y_2)$. This is straightforward to implement for the five dimensional integral, but more complicated for the four dimensional integral case, thus we choose the first case. Due to an oversight, the results obtained in this section are computed only for the fermion rapidity $y_2 = 0$.

Fig. 4.10 shows the photon spectrum obtained using a randomly generated set of 140 $(\mathbf{q_{T1}}, \mathbf{q_{T2}})$ values. The statistical error due to the integration method was estimated using a jackknife method. For a set of 140 values, the standard deviation for the photon spectrum due only to the Monte Carlo integration method is around 15%, with slightly higher values for $k_T < 1$ GeV. This error is similar to the one obtained by averaging only over 5 different configurations of initial color charge.

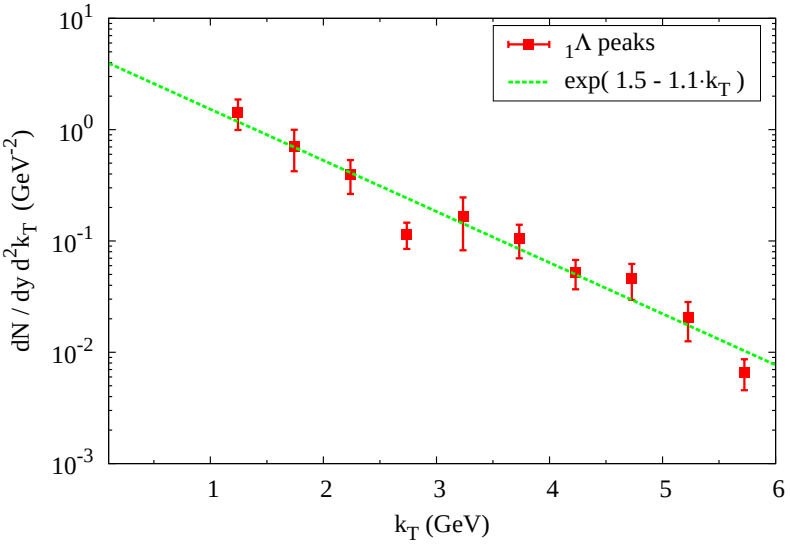

Figure 4.11: The data points represent the contribution of the $_1\Lambda$ peaks to the photon spectrum. The curve represents an exponential fit of the data with the parameters given in the legend. Each data point represents an average over 5 or more peak contributions at that given transverse momentum. The error bars represent statistical errors computed using the jackknife method.

The results from Fig. 4.10 are not the only contribution to the photon spectrum. The second contribution is given by the peaks in the first term of the photon rate (see Eq. (4.37)). Since the peaks heights vary by more than 2 orders of magnitude for a given k_T photon momentum, we took an average of those values for each k_T. The results are shown in Fig. 4.11 where we see that the results are consistent with an exponential decaying function on k_T.

Fig. 4.12 shows the two contributions (the $_1\Lambda$ term with the peaks removed and the peaks) as well as their sum which gives the total photon spectrum. We see that the two contributions are similar, with the peaks being the dominant contribution for $k_T \leq 1$ GeV while the $_1\Lambda$ term becomes dominant for $k_T \geq 1.5$ GeV. The numerical

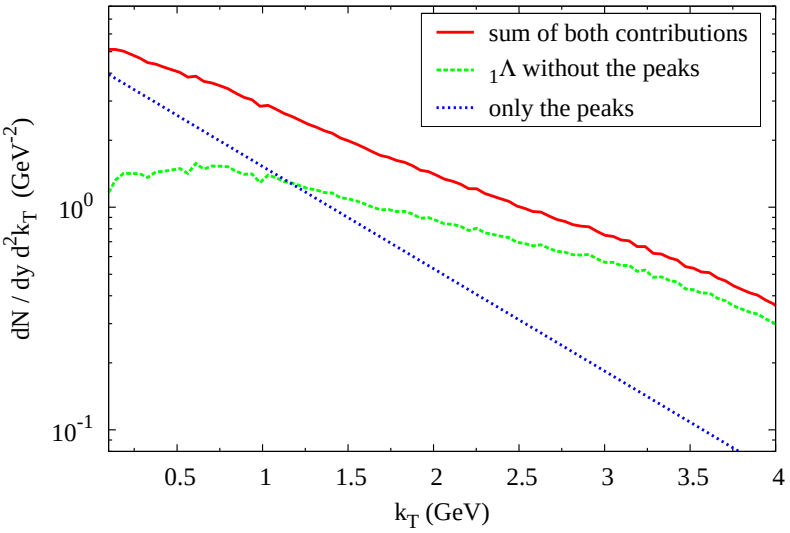

Figure 4.12: The total photon spectrum for quark mass $m = 0.3$ GeV and $\mu = 0.5$ GeV at $\tau = 0.25$ fm.

results from Fig. 4.12 correspond to 60 produced photons for $k_T \leq 4$ GeV, 40 of them are given by the continuum spectrum of $_1\Lambda$ and 20 by the peaks contribution.

The results presented in Fig. 4.12 are computed for quark rapidity $y_1 = 0$ and antiquark rapidity $y_2 = 0$. From Fig. 4.5 we see that the $_1\Lambda$ term is independent on the $y_1 - y_2$ value but does depend on the $y_1 + y_2$ value. When also taking into account this dependence on $y_1 + y_2$, we expect that the total photon spectrum to be around 15% lower[1].

4.4 Discussion and conclusion

In this section we showed that photon production for HIC in the CGC formalism is a feasible task. Starting from a complicated general expression for the photon production rate [39, 40], we simplified the equations using symmetries and properties of the CGC and MV models. This is an important step since it reduces considerably the

[1]In the right panel in Fig. 4.5 we see that by going from $y_1 + y_2 = 0$ to $y_1 + y_2 = 1$ the amplitude of the spectrum decreases by a factor of two. For a rough estimation we can take this decrease to be linear with $y_1 + y_2$. When inserting this ansatz in Eq. (4.36), we obtain that the total spectrum is 17% lower than the one computed for $y_1 = y_2 = 0$ - spectrum shown in Fig. 4.12.

computational time and resources. We continued by testing the numerical algorithm for different parameters and lattice sizes. We observed that the main contribution to the photon spectrum is given by the first Feynman diagram in Fig. 4.1, with the second diagram suppressed by at least an order of magnitude, if not more. The contribution of the first Feynman diagram can be split into a continuous spectrum plus a prominent peak at $\mathbf{k_T} = \mathbf{q_{T1}} + \mathbf{q_{T2}}$. Both give similar contributions to the final photon spectrum, so we must compute both of them. We ended with the computation of the total photon spectrum. Even though we have to compute a five dimensional integral using the Monte Carlo method, we obtain a relatively small standard deviation (under 20%) for just 140 steps in the Monte Carlo integration method.

We do not expect our results to give a good description of experimental data due to the very simple model that we used to describe the HIC. One of the major drawbacks is given by the modeling of the transverse plane where we took the same charge density squared everywhere. But in a real nucleus we expect the charge density square to be the largest in the center and then to decrease as we go towards the nucleus boundaries. In Sec. 2.2.3 we argued that the static color charge is given by independent fluctuating charges. This means that the correlation $\langle \rho^a(\mathbf{x_T}) \rho^b(\mathbf{y_T}) \rangle$ (given in our simple model by Eq. (2.31)) needs to be proportional with the nucleus thickness. Such a requirement raises another problem, since the fields in such a model have long Coulomb tails outside the nuclei [27]. Physically this is not the case, since due to confinement effects not included in our classical model, the gluonic fields should decay at distances $\sim \frac{1}{\Lambda_{QCD}}$. To solve this problem, Refs. [52, 53] propose to impose color neutrality of the sources at a length scale of the order of a nucleon radius.

The small k_T region ($k_T \lesssim 2$ GeV) of the photon spectrum is dominated by thermal photons [48]. Thus, to be able to compare our numerical results with experimental data, we have to use larger transverse lattices, such that we compute the photon spectrum up to higher k_T momenta. Further improvements may also require the expansion of the model for the color gauge field from 2+1 dimensions to the full 3+1 dimensions by dropping the boost invariance requirement.

5

Conclusion

In this thesis, we studied what are the predictions of the classical field model developed in [24, 25, 26] for quark and photon production in HIC. More specifically, we modeled the first instants of AA collisions using a boost invariant classical field theory in the framework of the CGC and MV formalisms. Both quark and photon production are important observables in HIC, observables that allows us to discover and understand new states of matter, like QGP. Photon production is especially an useful observational tool, since compared to partons, photons, once created, have a very small probability of interacting again. Thus photons are very good probes for all the stages in HIC.

In Sec. 3 we independently verified the numerical results from [29, 30, 31] for quark production in the CGC formalism. In doing so, we developed an iterative method for solving the non-linear system of equations that gives the initial condition for the gluonic field. We found this method to be much faster than typical simulated annealing methods that were used before.

In Sec. 4 we started from the photon production rate in the CGC formalism [39, 40]. The first step was a simplification of the expression using symmetries and properties of the CGC and MV models. We found that from the two Feynman diagrams included in our study, one has a much larger contribution than the other one. The dominant diagram is given by a continuum spectrum with a large peak superimposed on top. The continuum spectrum and the peak contributions have similar values, hence both of them have to be included in the final photon spectrum calculation. To the able to compare with experimental results, further improvements

are needed like taking into consideration the dependence of the charge density squared on position in the transverse plane.

A

Coordinates transformations and Dirac equation

This section serves as a short reminder of coordinate transformations and basic facts about Dirac matrices and spinors. We start with a short overview of the most important coordinate systems in HIC physics, with emphasis on the coordinate transformation rules for tensors. In the second part we present our convention for the Dirac matrices, define some useful projection operators and analyze their action on the Dirac field. We end this section with a short overview of Dirac spinors, where we give explicit expressions for the quark and antiquark spinors for a general momentum direction.

A.1 Coordinate transformations

Starting with the Cartesian coordinates $(t, z, \mathbf{x_T})$, described by the metric $g_{\mu\nu} = diag(1, -1, -1, -1)$, we define light cone (LC) coordinates $(x^+, x^-, \mathbf{x_T})$, proper time τ and space rapidity η (quantities which are very often used in HIC physics) via:

$$\begin{array}{rcccl} x^\pm & = & \frac{1}{\sqrt{2}}(t \pm x) & = & \frac{1}{\sqrt{2}}\tau e^{\pm\eta} \\ \tau & = & \sqrt{t^2 - z^2} & = & \sqrt{x^+ x^-} \\ \eta & = & \frac{1}{2}\ln\left(\frac{t+z}{t-z}\right) & = & \frac{1}{2}\ln\left(\frac{x^+}{x^-}\right) \end{array} \tag{A.1}$$

relations which can be inverted to obtain:

$$\begin{array}{rcccl} t & = & \frac{1}{\sqrt{2}}(x^+ + x^-) & = & \tau\cosh\eta \\ z & = & \frac{1}{\sqrt{2}}(x^+ - x^-) & = & \tau\sinh\eta \end{array} \tag{A.2}$$

During a coordinate transformation, the first rank tensors transform via:

$$A^{\mu'} = \frac{\partial x^{\mu'}}{\partial x^\mu} A^\mu \qquad A_{\mu'} = \frac{\partial x^\mu}{\partial x^{\mu'}} A_\mu \tag{A.3}$$

where μ denotes the tensor in the old coordinates and μ' denotes the tensor in the new coordinates. The above expressions give the transformation rules for a rank 1 tensor, but they can be very easily generalized to multiple rank tensors. For example the metric, which is a rank 2 tensor, transforms as:

$$g_{\mu'\nu'} = \frac{\partial x^{\mu}}{\partial x^{\mu'}} \frac{\partial x^{\nu}}{\partial x^{\nu'}} g_{\mu\nu}. \tag{A.4}$$

The above equation can be applied to find the metric in the other 3 coordinate systems widely use in this thesis: $(x^+, x^-, \mathbf{x_T})$, $(\tau, \eta, \mathbf{x_T})$ and $(\tau, z, \mathbf{x_T})$. The easiest way to do so is to start from Cartesian coordinates and use the relations defined in Eqs. (A.1)-(A.2), to obtain:

$$g_{\mu\nu}(x^+, x^-, \mathbf{x_T}) = \begin{pmatrix} 0 & 1 & 0 & 0 \\ 1 & 0 & 0 & 0 \\ 0 & 0 & -1 & 0 \\ 0 & 0 & 0 & -1 \end{pmatrix} \quad g_{\mu\nu}(\tau, \eta, \mathbf{x_T}) = \begin{pmatrix} 1 & 0 & 0 & 0 \\ 0 & -1 & 0 & 0 \\ 0 & 0 & -1 & 0 \\ 0 & 0 & 0 & -\tau^2 \end{pmatrix}$$

$$g_{\mu\nu}(\tau, z, \mathbf{x_T}) = \begin{pmatrix} 1 & 0 & 0 & \frac{z}{\tau} \\ 0 & -1 & 0 & 0 \\ 0 & 0 & -1 & 0 \\ \frac{z}{\tau} & 0 & 0 & -1 \end{pmatrix}.$$

Another useful example is to see how the gauge field A_μ transforms from the $(\tau, \eta, \mathbf{x_T})$ coordinates to the $(\tau, z, \mathbf{x_T})$ ones. Using Eqs. (A.1)-(A.3) we obtain:

$$A_\tau = A_\tau - \frac{z}{\tau\sqrt{\tau^2 + z^2}} A_\eta \tag{A.5}$$

$$A_z = \frac{1}{\sqrt{\tau^2 + z^2}} A_\eta \tag{A.6}$$

and with the A_x and A_y components remaining the same. In the above equations, on the left hand side are the fields in the $(\tau, z, \mathbf{x_T})$ coordinates and on the right hand side the fields in the $(\tau, \eta, \mathbf{x_T})$ coordinates.

A.2 Dirac matrices

In this thesis we choose the γ matrices in the Weyl or chiral basis (the same as in [8]) which for the case of 3 spatial dimensions are given by:

$$\gamma^0 = \begin{pmatrix} 0 & 0 & 1 & 0 \\ 0 & 0 & 0 & 1 \\ 1 & 0 & 0 & 0 \\ 0 & 1 & 0 & 0 \end{pmatrix} \qquad \gamma^1 = \begin{pmatrix} 0 & 0 & 0 & 1 \\ 0 & 0 & 1 & 0 \\ 0 & -1 & 0 & 0 \\ -1 & 0 & 0 & 0 \end{pmatrix}$$
$$\gamma^2 = \begin{pmatrix} 0 & 0 & 0 & -i \\ 0 & 0 & i & 0 \\ 0 & i & 0 & 0 \\ -i & 0 & 0 & 0 \end{pmatrix} \qquad \gamma^3 = \begin{pmatrix} 0 & 0 & 1 & 0 \\ 0 & 0 & 0 & -1 \\ -1 & 0 & 0 & 0 \\ 0 & 1 & 0 & 0 \end{pmatrix} \tag{A.7}$$

and which satisfy the relation:

$$\{\gamma^\mu, \gamma^\nu\} = 2g^{\mu\nu}. \tag{A.8}$$

The above equation is the definition of the Dirac matrices. The matrix g is the metric in Cartesian coordinates.

In HIC physics, the dynamics of the theory can be simplified using the projection operators

$$P^\pm = \frac{1}{2}(1 \pm \gamma^0\gamma^3), \tag{A.9}$$

whose explicit expressions in the chiral basis are given by:

$$P^+ = \begin{pmatrix} 0 & 0 & 0 & 0 \\ 0 & 1 & 0 & 0 \\ 0 & 0 & 1 & 0 \\ 0 & 0 & 0 & 0 \end{pmatrix} \qquad P^- = \begin{pmatrix} 1 & 0 & 0 & 0 \\ 0 & 0 & 0 & 0 \\ 0 & 0 & 0 & 0 \\ 0 & 0 & 0 & 1 \end{pmatrix}.$$

Using the definition in Eq. (A.9), it is easy to check that indeed the two matrices

satisfy the properties of projection operators:

$$P^{\pm}P^{\pm} = P^{\pm}$$

$$P^{\mp}P^{\pm} = 0$$

$$P^{+} + P^{-} = 1.$$

Moreover, using Eqs. (A.8)-(A.9), it can be shown that:

$$P^{\pm} = \frac{1}{2}(1 \pm \gamma^0\gamma^3) = \frac{1}{\sqrt{2}}\gamma^0\gamma^{\pm} = \frac{1}{\sqrt{2}}\gamma^{\mp}\gamma^0 = \frac{1}{2}\gamma^{\mp}\gamma^{\pm} \tag{A.10}$$

where the LC Dirac matrices $\gamma^{\pm}$ are defined as:

$$\gamma^{\pm} = \frac{1}{\sqrt{2}}(\gamma^0 \pm \gamma^3). \tag{A.11}$$

Another important aspect is the action of the projection operators on the Dirac field. In the following we use the notation $P^{\pm}\Psi = \Psi^{\pm}$. In the chiral basis, the $\Psi^{\pm}$ components of the Dirac field have each only two nonzero Dirac components. So the Dirac field, in terms of Dirac components, is given by:

$$\Psi = \begin{pmatrix} \Psi_1 \\ \Psi_2 \\ \Psi_3 \\ \Psi_4 \end{pmatrix}, \text{ with} \qquad \Psi^{+} = \begin{pmatrix} 0 \\ \Psi_2 \\ \Psi_3 \\ 0 \end{pmatrix} \qquad \Psi^{-} = \begin{pmatrix} \Psi_1 \\ 0 \\ 0 \\ \Psi_4 \end{pmatrix}. \tag{A.12}$$

Another important property for the $\Psi^{\pm}$ components is given by:

$$\gamma^0\gamma^3\Psi^{\pm} = \pm\Psi^{\pm} \tag{A.13}$$

which can be shown to hold using Eq. (A.10) for any representation of the Dirac matrices. This relation is necessary to obtain the Dirac equation for each $\Psi^{\pm}$ component in the $(\tau, z, \mathbf{x_T})$ coordinate system.

For the 1+1 dimensional case we chose the following basis for the Dirac matrices:

$$\gamma^0 = \begin{pmatrix} 0 & 1 \\ 1 & 0 \end{pmatrix} \qquad \gamma^3 = \begin{pmatrix} 0 & -1 \\ 1 & 0 \end{pmatrix}. \tag{A.14}$$

Now the projection matrices take the form:

$$P^+ = \begin{pmatrix} 1 & 0 \\ 0 & 0 \end{pmatrix} \qquad P^- = \begin{pmatrix} 0 & 0 \\ 0 & 1 \end{pmatrix}. \tag{A.15}$$

Eq. (A.10) holds also for the 1+1 dimensional case.

The Dirac field in 1+1 dimensions has only two Dirac components. In the chiral basis the two components are given by $\Psi^{\pm}$ such that:

$$\Psi = \begin{pmatrix} \Psi^+ \\ \\ \Psi^- \end{pmatrix} \tag{A.16}$$

where in this case $\Psi^{\pm}$ are just color vectors.

A.3 Dirac spinors

In this section we follow the approach given in [8] and [51]. The plane wave solutions of the Dirac equation are given by:

$$\Psi_1(x) = e^{-ip\cdot x}u(p) \tag{A.17}$$

$$\Psi_2(x) = e^{ip\cdot x}v(p) \tag{A.18}$$

where $\Psi_1(x)$ is the positive energy solution and $\Psi_2(x)$ is the negative energy solution, such that $p^0 > 0$ for both equations. The above two wavefunction must be solutions of the Dirac equation, hence they must satisfy:

$$(i\not{D} - m)\Psi_{1,2}(x) = 0. \tag{A.19}$$

Taking the solution given in Eq. (A.17) and inserting it into Eq. (A.19) leads to:

$$(p_\mu\gamma^\mu - m)u(p) = 0 \tag{A.20}$$

which can be evaluated most easily in the rest frame of the particle, i.e. when $\mathbf{p} = 0$. Now, the above equation reduces to:

$$(\gamma^0 - 1)u(p_0) = 0 \tag{A.21}$$

which has two solutions given by:

$$u^{\alpha}(p_0) = \sqrt{m}\begin{pmatrix}\xi^{\alpha}\\ \xi^{\alpha}\end{pmatrix} \qquad \xi^1 = \begin{pmatrix}1\\0\end{pmatrix} \qquad \xi^2 = \begin{pmatrix}0\\1\end{pmatrix} \tag{A.22}$$

where α=1,2 denotes the two possible solutions of Eq. (A.21). The two values of α denote the two different spin orientations of fermions in 3 spatial dimensions. In the expression for $u(p)$ we choose a $\sqrt{m}$ factor such that we satisfy the normalization condition $\bar{u}^{\alpha}u^{\beta} = 2m\delta^{\alpha\beta}$. The quantity $u^{\alpha}(p_0)$ denotes the Dirac spinor solution only in the rest frame, i.e. $p_0 = (m, \mathbf{0})$.

Similar calculations using Eq. (A.18) give:

$$(p_{\mu}\gamma^{\mu} + m)v(p) = 0 \tag{A.23}$$

which in the rest frame of the particle give:

$$v^{\alpha}(p_0) = \sqrt{m}\begin{pmatrix}\eta^{\alpha}\\ -\eta^{\alpha}\end{pmatrix} \qquad \eta^1 = \begin{pmatrix}1\\0\end{pmatrix} \qquad \eta^2 = \begin{pmatrix}0\\1\end{pmatrix} \tag{A.24}$$

where again α= 1,2 and $v^{\alpha}(p_0)$ denotes the Dirac spinor solution in the rest frame when $p_0 = (m, \mathbf{0})$.

Once we have the Dirac spinor in the rest frame, by boosting we can obtain the general solution in any frame. Using the approach given in [51], the general solutions are given by:

$$u^{\alpha}(p) = \frac{p_{\mu}\gamma^{\mu} + m}{\sqrt{2m(m+E)}}\, u^{\alpha}(p_0) \tag{A.25}$$

$$v^{\alpha}(p) = \frac{-p_{\mu}\gamma^{\mu} + m}{\sqrt{2m(m+E)}}\, v^{\alpha}(p_0). \tag{A.26}$$

It is straightforward to check that the above satisfy Eq. (A.20) and Eq. (A.23) respectively. This is obvious since $(p_{\mu}\gamma^{\mu} + m)(p_{\mu}\gamma^{\mu} - m) = p^2 - m^2 = 0$. Component

wise, the above equations read:

$$u^{\uparrow}(p) = \frac{1}{\sqrt{2(m+E)}} \begin{pmatrix} m+E-p_z \\ -(p_x + i\, p_y) \\ m+E+p_z \\ p_x + i\, p_y \end{pmatrix} \qquad u^{\downarrow}(q) = \frac{1}{\sqrt{2(m+E)}} \begin{pmatrix} -(p_x - i\, p_y) \\ m+E+p_z \\ p_x - i\, p_y \\ m+E-p_z \end{pmatrix}$$

$$v^{\downarrow}(q) = \frac{1}{\sqrt{2(m+E)}} \begin{pmatrix} m+E-p_z \\ -(p_x + i\, p_y) \\ -(m+E+p_z) \\ -(p_x + i\, p_y) \end{pmatrix} \qquad v^{\uparrow}(q) = \frac{1}{\sqrt{2(m+E)}} \begin{pmatrix} -(p_x - i\, p_y) \\ m+E+p_z \\ -(p_x - i\, p_y) \\ -(m+E-p_z) \end{pmatrix}$$

where $\uparrow$ and $\downarrow$ denote the two spin orientations. Eqs. (A.25) and (A.26) are chosen such that the following normalization conditions are satisfied:

$$\bar{u}^{\alpha} u^{\beta} = -\bar{v}^{\alpha} v^{\beta} = 2m\delta^{\alpha\beta} \tag{A.27}$$

$$\bar{u}^{\alpha} v^{\beta} = -\bar{v}^{\alpha} u^{\beta} = 0. \tag{A.28}$$

In the case of only 1 spatial dimension, very similar calculations give:

$$u(p) = \frac{1}{2(m+E)} \begin{pmatrix} m+E+p_z \\ m+E-p_z \end{pmatrix} = \sqrt{m} \begin{pmatrix} e^{\frac{1}{2}y} \\ e^{-\frac{1}{2}y} \end{pmatrix} \tag{A.29}$$

$$v(p) = \frac{1}{2(m+E)} \begin{pmatrix} m+E+p_z \\ -(m+E-p_z) \end{pmatrix} = \sqrt{m} \begin{pmatrix} e^{\frac{1}{2}y} \\ -e^{-\frac{1}{2}y} \end{pmatrix}. \tag{A.30}$$

As can be seen from above, in 1 spatial dimensions the Dirac particles do not have spins. As previously, the Dirac spinor are normalized such that:

$$\bar{u}u = -\bar{v}v = 2m \tag{A.31}$$

$$\bar{u}v = \bar{v}u = 0. \tag{A.32}$$

B

Additional numerical details

In the previous chapters about numerical simulations we included mostly details on how to go from the analytical Dirac equation to a stable Dirac equation on the lattice. In this chapter we focus mostly on the programming and algorithm details necessary for writing a memory and time efficient code. We start by discussing the initial condition which is complicated due to a transverse momentum integral for each point of the three dimensional spatial lattice and also due to operations with 12×12 matrices (for the special case of $SU(3)$). We continue in the next section with a more in depth look at the linear system of equation that we have to solve to evolve the Dirac field at each time step. We end by presenting the algorithm diagram for the time evolution of the gauge and Dirac fields.

B.1 Implementation of the initial condition in 3+1 dimensions

The initial condition for the 3+1 dimensions calculation given by Eq. (3.37) presents several challenges. First, for each spatial lattice point there is a transverse momentum integral. Computing these momentum integrals in the form given in Eq. (3.37) can be very time consuming. Just by splitting the initial condition in the sum of a few term which depend only on a Fourier transform in the transverse plane the code become much faster, especially if one makes use of the FFTW libraries. Depending on the size of the lattice, such a trick can decrease the computation time by over 100 times. Moreover, when working within the $SU(3)$ gauge theory, the Dirac field has 12 entries

(4 from Dirac components times 3 from the color structure). So if one does not pay attention to write Eq. (3.37) for each Dirac component, than one ends with operations involving 12×12 matrices, which is very time and memory inefficient, especially since most of the entries are 0.

In this section, for readability and simplicity in notation, we work with the continuous form of the initial condition for the Dirac wavefunction. But when implementing these details numerically, one has to pay attention to take into account the changes that arise when going from the continuum to a discrete lattice. These changes are presented in Sec. 3.4.3.

We start by splitting Eq. (3.37) in a sum of transverse Fourier transforms. First, let us define the following quantities[1]:

[1]These functions do not have any physical meaning, they are just useful in computing efficiently the initial values of the Dirac field.

$$
\begin{aligned}
A_1 &= \int \frac{d^2\mathbf{k_T}}{(2\pi)^2} e^{-i\mathbf{k_T}\cdot\mathbf{x_T}} \;\; (k_x+q_x)\frac{e^{y_q}}{\omega_q} U^{\dagger}_{(1)}(\mathbf{k_T}) \;\; \exp\left(i\frac{\omega^2_{k+q}e^{y_q}(|z|-z)}{2\omega_q}\right) \\
A_2 &= \int \frac{d^2\mathbf{k_T}}{(2\pi)^2} e^{-i\mathbf{k_T}\cdot\mathbf{x_T}} \;\; (k_y+q_y)\frac{e^{y_q}}{\omega_q} U^{\dagger}_{(1)}(\mathbf{k_T}) \;\; \exp\left(i\frac{\omega^2_{k+q}e^{y_q}(|z|-z)}{2\omega_q}\right) \\
A_3 &= \int \frac{d^2\mathbf{k_T}}{(2\pi)^2} e^{-i\mathbf{k_T}\cdot\mathbf{x_T}} \;\; (-m)\frac{e^{y_q}}{\omega_q} U^{\dagger}_{(1)}(\mathbf{k_T}) \;\; \exp\left(i\frac{\omega^2_{k+q}e^{y_q}(|z|-z)}{2\omega_q}\right) \\
C_1 &= \int \frac{d^2\mathbf{k_T}}{(2\pi)^2} e^{-i\mathbf{k_T}\cdot\mathbf{x_T}} \;\; (k_x+q_x)U^{\dagger}_{(1)}(\mathbf{k_T})\frac{1}{\omega^2_{k+q}} \;\; \left[\exp\left(i\frac{\omega^2_{k+q}e^{y_q}(|z|-z)}{2\omega_q}\right)-1\right] \\
C_2 &= \int \frac{d^2\mathbf{k_T}}{(2\pi)^2} e^{-i\mathbf{k_T}\cdot\mathbf{x_T}} \;\; (k_y+q_y)U^{\dagger}_{(1)}(\mathbf{k_T})\frac{1}{\omega^2_{k+q}} \;\; \left[\exp\left(i\frac{\omega^2_{k+q}e^{y_q}(|z|-z)}{2\omega_q}\right)-1\right] \\
C_3 &= \int \frac{d^2\mathbf{k_T}}{(2\pi)^2} e^{-i\mathbf{k_T}\cdot\mathbf{x_T}} \;\; (-m)U^{\dagger}_{(1)}(\mathbf{k_T})\frac{1}{\omega^2_{k+q}} \;\; \left[\exp\left(i\frac{\omega^2_{k+q}e^{y_q}(|z|-z)}{2\omega_q}\right)-1\right] \\
B_1 &= \int \frac{d^2\mathbf{k_T}}{(2\pi)^2} e^{-i\mathbf{k_T}\cdot\mathbf{x_T}} \;\; (k_x+q_x)\frac{e^{-y_q}}{\omega_q} U^{\dagger}_{(2)}(\mathbf{k_T}) \;\; \exp\left(i\frac{\omega^2_{k+q}e^{-y_q}(|z|+z)}{2\omega_q}\right) \\
B_2 &= \int \frac{d^2\mathbf{k_T}}{(2\pi)^2} e^{-i\mathbf{k_T}\cdot\mathbf{x_T}} \;\; (k_y+q_y)\frac{e^{-y_q}}{\omega_q} U^{\dagger}_{(2)}(\mathbf{k_T}) \;\; \exp\left(i\frac{\omega^2_{k+q}e^{-y_q}(|z|+z)}{2\omega_q}\right) \\
B_3 &= \int \frac{d^2\mathbf{k_T}}{(2\pi)^2} e^{-i\mathbf{k_T}\cdot\mathbf{x_T}} \;\; (-m)\frac{e^{-y_q}}{\omega_q} U^{\dagger}_{(2)}(\mathbf{k_T}) \;\; \exp\left(i\frac{\omega^2_{k+q}e^{-y_q}(|z|+z)}{2\omega_q}\right) \\
D_1 &= \int \frac{d^2\mathbf{k_T}}{(2\pi)^2} e^{-i\mathbf{k_T}\cdot\mathbf{x_T}} \;\; (k_x+q_x)U^{\dagger}_{(2)}(\mathbf{k_T})\frac{1}{\omega^2_{k+q}} \;\; \left[\exp\left(i\frac{\omega^2_{k+q}e^{-y_q}(|z|+z)}{2\omega_q}\right)-1\right] \\
D_2 &= \int \frac{d^2\mathbf{k_T}}{(2\pi)^2} e^{-i\mathbf{k_T}\cdot\mathbf{x_T}} \;\; (k_y+q_y)U^{\dagger}_{(2)}(\mathbf{k_T})\frac{1}{\omega^2_{k+q}} \;\; \left[\exp\left(i\frac{\omega^2_{k+q}e^{-y_q}(|z|+z)}{2\omega_q}\right)-1\right] \\
D_3 &= \int \frac{d^2\mathbf{k_T}}{(2\pi)^2} e^{-i\mathbf{k_T}\cdot\mathbf{x_T}} \;\; (-m)U^{\dagger}_{(2)}(\mathbf{k_T})\frac{1}{\omega^2_{k+q}} \;\; \left[\exp\left(i\frac{\omega^2_{k+q}e^{-y_q}(|z|+z)}{2\omega_q}\right)-1\right]
\end{aligned}
$$

where A_i, B_i, C_i and D_i (with $i = 1, 2, 3$) represent functions that depend on the position in coordinate space (i.e. $(\mathbf{x_T}, z)$). One must be careful since this functions are 3×3 matrices for the SU(3) case. These discrete functions can be computed relatively fast using a Discrete Fourier Transform (DFT) library like FFTW. Moreover, at some lattice points some of these functions are identically 0, so the computations can be simplified even further. We have the following:

- For $z < 0$ we have $|z| + z = 0$, hence $D_i = 0$ and B_i takes a much simpler form.
- For $z > 0$ we have $|z| - z = 0$, hence $C_i = 0$ and A_i takes a much simpler form.

with i=1,2,3. So for each lattice point on the z direction one has to compute only 9 two-dimensional Fourier transforms.

Using the notations given above, Eq. (3.37) reads:

$$\begin{aligned}\Psi(0,\mathbf{x_T},z) = \big\{ & P^+ U_{(1)}(\mathbf{x_T})\ (\gamma^0\gamma^1 A_1 + \gamma^0\gamma^2 A_2 + \gamma^0 A_3) \\ & + P^- \gamma^0 [i\gamma_\mathbf{T}\cdot\tilde{\mathbf{D}}_\mathbf{T} - m] U_{(1)}(\mathbf{x_T})\ (\gamma^0\gamma^1 C_1 + \gamma^0\gamma^2 C_2 + \gamma^0 C_3) \\ & + P^- U_{(2)}(\mathbf{x_T})\ (\gamma^0\gamma^1 B_1 + \gamma^0\gamma^2 B_2 + \gamma^0 B_3) \\ & + P^+ \gamma^0 [i\gamma_\mathbf{T}\cdot\tilde{\mathbf{D}}_\mathbf{T} - m] U_{(2)}(\mathbf{x_T})\ (\gamma^0\gamma^1 D_1 + \gamma^0\gamma^2 D_2 + \gamma^0 D_3) \big\} \\ \times\ & e^{-i\mathbf{q_T}\cdot\mathbf{x_T}}\ v(q) \end{aligned} \tag{B.1}$$

where $\tilde{\mathbf{D}}_\mathbf{T}$ denotes the transverse covariant derivative, such that it can be distinguished from the D_i matrices. Eq. (B.1) suggests that we can define the following quantities:

$$\begin{aligned} A_{1j} &= U_{(1)}(\mathbf{x_T})\ e^{-i\mathbf{q_T}\cdot\mathbf{x_T}}\ A_j \\ C_{1j} &= i\tilde{D}_1 \left[U_{(1)}(\mathbf{x_T})\ e^{-i\mathbf{q_T}\cdot\mathbf{x_T}}\ C_j\right] \\ C_{2j} &= i\tilde{D}_2 \left[U_{(1)}(\mathbf{x_T})\ e^{-i\mathbf{q_T}\cdot\mathbf{x_T}}\ C_j\right] \\ C_{3j} &= -mU_{(1)}(\mathbf{x_T})\ e^{-i\mathbf{q_T}\cdot\mathbf{x_T}}\ C_j \\ B_{1j} &= U_{(2)}(\mathbf{x_T})\ e^{-i\mathbf{q_T}\cdot\mathbf{x_T}}\ B_j \\ D_{1j} &= i\tilde{D}_1 \left[U_{(2)}(\mathbf{x_T})\ e^{-i\mathbf{q_T}\cdot\mathbf{x_T}}\ D_j\right] \\ D_{2j} &= i\tilde{D}_2 \left[U_{(2)}(\mathbf{x_T})\ e^{-i\mathbf{q_T}\cdot\mathbf{x_T}}\ D_j\right] \\ D_{3j} &= -mU_{(2)}(\mathbf{x_T})\ e^{-i\mathbf{q_T}\cdot\mathbf{x_T}}\ D_j \end{aligned}$$

with $j = 1, 2, 3$. The above notations reduce Eq. (B.1) to:

$$\begin{aligned}\Psi(0,z,\mathbf{x_T}) = \big\{ & P^+(\gamma^0\gamma^1 A_{11} + \gamma^0\gamma^2 A_{12} + \gamma^0 A_{13}) \\ & + P^-(C_{11} - \gamma^1\gamma^2 C_{12} - \gamma^1 C_{13} - \gamma^2\gamma^1 C_{21} + C_{22} - \gamma^2 C_{23} \\ & \quad + \gamma^1 C_{31} + \gamma^2 C_{32} + C_{33}) \\ & + P^-(\gamma^0\gamma^1 B_{11} + \gamma^0\gamma^2 B_{12} + \gamma^0 B_{13}) \\ & + P^+(D_{11} - \gamma^1\gamma^2 D_{12} - \gamma^1 D_{13} - \gamma^2\gamma^1 D_{21} + D_{22} - \gamma^2 D_{23} \\ & \quad + \gamma^1 D_{31} + \gamma^2 D_{32} + D_{33}) \big\}\ v(q) \end{aligned} \tag{B.2}$$

where we used that $\gamma^0\gamma^0 = 1$, $\gamma^1\gamma^1 = \gamma^2\gamma^2 = -1$ and $\gamma^0\gamma^{1,2} = -\gamma^{1,2}\gamma^0$. Now, using the explicit expressions of the Dirac matrices given in Eq. (A.7), we can write the Eq. (B.2) explicitly for all Dirac components of Ψ (components that we denoted with 0 to 3):

$$\begin{aligned}
\Psi[0] &= (C_{11} + C_{22} + C_{33} + i\, C_{12} - i\, C_{21})\, v[0] \\
&\quad + (-B_{11} + i\, B_{12})\, v[1] \\
&\quad + B_{13}\, v[2] \\
&\quad + (-C_{13} + C_{31} + i\, C_{23} - i\, C_{32})\, v[3] \qquad \text{(B.3)} \\
\Psi[1] &= (-A_{11} - i\, A_{12})\, v[0] \\
&\quad + (D_{11} + D_{22} + D_{33} - i\, D_{12} + i\, D_{21})\, v[1] \\
&\quad + (-D_{13} + D_{31} - i\, D_{23} + i\, D_{32})\, v[2] \\
&\quad + A_{13}\, v[3] \qquad \text{(B.4)} \\
\Psi[2] &= A_{13}\, v[0] \\
&\quad + (D_{13} - D_{31} - i\, D_{23} + i\, D_{32})\, v[1] \\
&\quad + (D_{11} + D_{22} + D_{33} + i\, D_{12} - i\, D_{21})\, v[2] \\
&\quad + (A_{11} - i\, A_{12})\, v[3] \qquad \text{(B.5)} \\
\Psi[3] &= (C_{13} - C_{31} + i\, C_{23} - i\, C_{32})\, v[0] \\
&\quad + B_{13}\, v[1] \\
&\quad + (B_{11} + i\, B_{12})\, v[2] \\
&\quad + (C_{11} + C_{22} + C_{33} - i\, C_{12} + i\, C_{21})\, v[3] \qquad \text{(B.6)}
\end{aligned}$$

Now, in the last set of equations, we took explicitly into account the Dirac component structure of the Dirac field. Actually doing the γ-matrices multiplications from Eq. (B.2) inside the numerical code would be much more time consuming because most of the entries in the γ-matrices are 0. When implementing numerically Eqs. (B.3)-(B.6) is more efficient to remember that:

- For $z < 0$, D_{ij}=0 (with i, j=1,2,3)

- For $z > 0$, C_{ij}=0 (with i, j=1,2,3)

In the following we present an algorithm diagram on how to implement the numerical code which computes the initial values of the Dirac field.

• *Compute* $U^{\dagger}_{(1)}(\mathbf{k_T})$ *and* $U^{\dagger}_{(2)}(\mathbf{k_T})$ *from* $U_{(1)}(\mathbf{x_T})$ *and* $U_{(2)}(\mathbf{x_T})$.

• *Compute* $U^{\dagger}_{3,x}(\mathbf{x_T})$ *and* $U^{\dagger}_{3,y}(\mathbf{x_T})$ *- these link matrices are need for the transverse covariant derivative.*

• *For* $z = -z_{max}$ *to 0 do:*

{

⋆ *Compute* $A_i(\mathbf{k_T}, z)$, $B_i(\mathbf{k_T}, z)$ *and* $C_i(\mathbf{k_T}, z)$.

⋆ *Using a DFT library compute* $A_i(\mathbf{x_T}, z)$, $B_i(\mathbf{x_T}, z)$ *and* $C_i(\mathbf{x_T}, z)$.

⋆ *Within a loop over the transverse spatial coordinates compute* A_{1j}, B_{1j} *and* C_{ij} *and than using Eqs.* (B.3)-(B.6) *compute* Ψ.

}

• *For* $z = 0$ *to* z_{max} *do:*

{

⋆ *Compute* $A_i(\mathbf{k_T}, z)$, $B_i(\mathbf{k_T}, z)$ *and* $D_i(\mathbf{k_T}, z)$.

⋆ *Using a DFT library compute* $A_i(\mathbf{x_T}, z)$, $B_i(\mathbf{x_T}, z)$ *and* $D_i(\mathbf{x_T}, z)$.

⋆ *Within a loop over the transverse spatial coordinates compute* A_{1j}, B_{1j} *and* D_{ij} *and than using Eqs.* (B.3)-(B.6) *compute* Ψ.

}

B.2 Solving the LU system

In this section we present in more detail the entries of M and ξ matrices from Eq. (3.66), whose solution gives the Dirac field at the new time step. The elements of the M matrix given in Eq. (3.68) are the same for both the 1+1 and 3+1 dimensional

cases. Using the left hand side of Eq. (3.62) to read the m_{ij} entries, we obtain:

$$\begin{aligned}
m_{11} &= 1 \pm i\frac{\Phi_n a_\tau}{\tau} \mp 3\frac{\sqrt{\tau^2+z^2}\pm z}{2a_z\tau}a_\tau \\
m_{12} &= \pm 4\frac{\sqrt{\tau^2+z^2}\pm z}{2a_z\tau}a_\tau \qquad \text{(B.7)} \\
m_{13} &= \mp\frac{\sqrt{\tau^2+z^2}\pm z}{2a_z\tau}a_\tau \\
&\vdots \\
m_{jj-1} &= \mp\frac{\sqrt{\tau^2+z^2}\pm z}{2a_z\tau}a_\tau \\
m_{jj} &= 1 \pm i\frac{\Phi_n a_\tau}{\tau} \qquad \text{(B.8)} \\
m_{jj+1} &= \pm\frac{\sqrt{\tau^2+z^2}\pm z}{2a_z\tau}a_\tau \\
&\vdots \\
m_{NN-2} &= \pm\frac{\sqrt{\tau^2+z^2}\pm z}{2a_z\tau}a_\tau \\
m_{NN-1} &= \mp 4\frac{\sqrt{\tau^2+z^2}\pm z}{2a_z\tau}a_\tau \qquad \text{(B.9)} \\
m_{NN} &= 1 \pm i\frac{\Phi_n a_\tau}{\tau} \pm 3\frac{\sqrt{\tau^2+z^2}\pm z}{2a_z\tau}a_\tau
\end{aligned}$$

with the convention that wherever there is a $\pm$ or $\mp$ sign, the upper one is for the Ψ^+ component and the lower one is for the Ψ^- component. Moreover, for each element m_{ij} one has to take the value of z corresponding to the i-th lattice point in the z direction (if one labels the z lattice points starting with 1 from the left most z lattice point and increases the label to the right). The structure of the m_{1j} and m_{Nj} entries is different from the rest due to a different equation used to discretize the z-derivative at the endpoints of the z lattice (see Eqs. (3.63)-(3.64)).

The M entries for the evolution of the Dirac field from $\tau = 0$ to the first time step are the same as those in Eqs. (B.7)-(B.9) if one replaces $2a_\tau$ with a_τ.

For an efficient numerical implementation of the LU decomposition algorithm described in Sec. 3.4.2 one should not define an M matrix with the above entries. One should insert Eqs. (B.7)-(B.9) directly in the expressions of the L and U matrix elements defined in Sec. 3.4.2.

The elements of the $\xi \equiv \xi_n$ matrix defined in Eq. (3.65) can also be read from Eq. (3.62). In this case, the ξ matrix will have a different structure for the 3+1 dimensions than for 1+1 dimensions. In the following we give the ξ matrix for the 3+1 dimensional case; the one for 1+1 dimensions is obtained by dropping the term with the transverse covariant derivative. Using Eq. (3.62) we obtain:

$$\begin{aligned}
\xi_1 = \quad & (1 \mp i\frac{\Phi_n a_\tau}{\tau})\Psi^{\pm;1}_{n-1} \mp \frac{\sqrt{\tau^2+z^2} \pm z}{2a_z\tau} a_\tau(-3\Psi^{\pm;1}_{n-1} + 4\Psi^{\pm;2}_{n-1} - \Psi^{\pm;3}_{n-1}) \\
& - \frac{\sqrt{\tau^2+z^2} \pm z}{\tau} 2a_\tau\, \gamma^0(\gamma_{\mathbf{T}} \cdot \mathbf{D}_{\mathbf{T}} + im)\Psi^{\mp;1}_n \qquad \text{(B.10)} \\
\vdots & \\
\xi_j = \quad & (1 \mp i\frac{\Phi_n a_\tau}{\tau})\Psi^{\pm;j}_{n-1} \mp \frac{\sqrt{\tau^2+z^2} \pm z}{2a_z\tau} a_\tau(\Psi^{\pm;j+1}_{n-1} - \Psi^{\pm;j-1}_{n-1}) \\
& - \frac{\sqrt{\tau^2+z^2} \pm z}{\tau} 2a_\tau\, \gamma^0(\gamma_{\mathbf{T}} \cdot \mathbf{D}_{\mathbf{T}} + im)\Psi^{\mp;j}_n \qquad \text{(B.11)} \\
\vdots & \\
\xi_N = \quad & (1 \mp i\frac{\Phi_n a_\tau}{\tau})\Psi^{\pm;N}_{n-1} \mp \frac{\sqrt{\tau^2+z^2} \pm z}{2a_z\tau} a_\tau(3\Psi^{\pm;N}_{n-1} - 4\Psi^{\pm;N-1}_{n-1} + \Psi^{\pm;N-2}_{n-1}) \\
& - \frac{\sqrt{\tau^2+z^2} \pm z}{\tau} 2a_\tau\, \gamma^0(\gamma_{\mathbf{T}} \cdot \mathbf{D}_{\mathbf{T}} + im)\Psi^{\mp;N}_n \qquad \text{(B.12)}
\end{aligned}$$

where we used the same notations as for the entries of the M matrix given in Eqs. (B.7)-(B.9). All the Dirac fields are defined at the same transverse lattice point which was excluded to simplify notations. The upper and lower indices from $\Psi^{\pm}$ gives the z and τ lattice points where to evaluate the Dirac field. To obtain the ξ entries for the evolution from the initial condition to the first τ step one must replace in Eqs. (B.10)-(B.12) $2a_\tau$ with a_τ.

When implementing Eqs. (B.10)-(B.12) numerically it is important to observe that only two of the Dirac components of the ξ matrix are nonzero for $\Psi^{\pm}$. When computing Ψ^{+} only the Dirac entries 2 and 3 are nonzero, while when computing Ψ^{-} only the Dirac entries 1 and 4 are nonzero.

Solving the linear system of equations which gives the new values of the Dirac field at time step $n+1$ is the bottleneck of our numerical code. This is because at every time step we have to solve an implicit system of equations for all the points of

the transverse lattice. Hence it is important to have a optimal implementation of the algorithm, to minimize the running time. The algorithm diagram for one time step resumes to the following:

• *Decide which of the two components of the wavefunction to compute,* Ψ^- *or* Ψ^+*, depending if the time step* n *is odd or even.*

• *The elements denoted with* u *of the upper diagonal matrix* U *(from* $M = LU$*) are independent of the transverse lattice coordinate (with the exception of* u_3*) - see Sec. 3.4.2. Thus compute* u_i *with* $i = 1, .., N$ *but* $i \neq 3$*.*

• *For all transverse lattice points do:*

{

⋆ *Compute the matrix entries* u_3*,* d_i^{-1} *and* l_i *with* $i = 1, .., N$ *(see Sec. 3.4.2 for the meaning of* l *and* d*).*

⋆ *Compute the entries of* ξ *for the Dirac component 1 (if solving for* Ψ^-*) or 2 (if solving for* Ψ^+*).*

⋆ *Find the new entries of the* Ψ *field with Dirac component 1 (if solving for* Ψ^-*) or 2 (if solving for* Ψ^+*).*

⋆ *Compute the entries of* ξ *for the Dirac component 4 (if solving for* Ψ^-*) or 3 (if solving for* Ψ^+*).*

⋆ *Find the new entries of the* Ψ *field with Dirac component 4 (if solving for* Ψ^-*) or 3 (if solving for* Ψ^+*).*

}

B.3 Algorithm diagram for gauge and quark fields evolution

In this section we present the algorithm diagram for gauge and quark fields time evolution as well as the necessary steps for quark and photon production. The time evolution algorithm for the gauge and quark fields can be summarized as:

• *Compute the initial conditions for the gluon field. This involves fixing the transverse Coulomb gauge. We will present more details about this stage later on.*

• *Compute the initial conditions for the Dirac wavefunction* Ψ. *See the end of Sec. B.1 for a detailed description of this stage.*

• *Compute the gauge fields at the first time step using Eqs.* (3.16)-(3.20). *We first evolve the* E_i *(with* $i = 1, 2$*) and* π *fields from* $\tau = 0$ *to* $\tau = \frac{a_\tau}{2}$ *using the* U_i *and* ϕ *fields at* $\tau = 0$. *Then using the* E_i *and* π *fields at* $\tau = \frac{a_\tau}{2}$, *we evolve the* U_i *and* ϕ *fields from* $\tau = 0$ *to* $\tau = a_\tau$[1].

• *Evolve one of the Dirac field components, lets say* Ψ^- *from* $\tau = 0$ *to* $\tau = a_\tau$. *The other component of the wavefunction,* Ψ^+, *is not evolved in time at this stage*[2]. *The algorithm for finding the new values of* Ψ^- *is presented at the end of Sec. B.2.*

• *For time step n=1 to* $\mathcal{N}$[3]*-1 do:*

{

⋆ *If n is odd than evolve the* Ψ^+ *component of the Dirac field from time step* $n-1$ *to* $n+1$. *If n is even than evolve the* Ψ^- *component of the Dirac field from time step* $n-1$ *to* $n+1$. *Keep the other component of the Dirac field unchanged. See the end of Sec. B.2 for the details of finding the new* Ψ^+ *or* Ψ^- *component.*

⋆ *Evolve the gauge field one more time step*[4]. *Take the* E_i *and* π *fields from time step* $n - \frac{1}{2}$ *to* $n + \frac{1}{2}$ *using the* U_i *and* ϕ *fields at time step n. Take the* U_i *and* ϕ *fields from time step n to* $n+1$ *using the* E_i *and* π *fields at time step* $n + \frac{1}{2}$.

}

• *Bring both components* $\Psi^\pm$ *of the Dirac field to the same time step. Depending if the total number of time steps* $\mathcal{N}$ *is odd or even, we must find* Ψ^+ *or* Ψ^- *at time step* $\mathcal{N}$. *We must use the same algorithm for finding the new value of* Ψ^+ *or* Ψ^- *as we*

[1] Using the leapfrog algorithm one needs to know the fields at time step n and $n+1$ while the momenta are computed at time steps $n - \frac{1}{2}$ and $n + \frac{1}{2}$.

[2] In the algorithm for solving the Dirac equation described in Sec. 3.4.1 the two components of the quark wavefunction $\Psi^\pm$ need to be known at different time steps. For example Ψ^- is known at odd time steps while Ψ^+ is known at even time steps.

[3] With $\mathcal{N}$ we denote the total number of time steps.

[4] We evolve the gauge fields to the next step only after first evolving the Dirac field. This is because at time step n we take one of the components $\Psi^\pm$ of the Dirac wavefunction from time step $n-1$ to $n+1$, for which we need the ϕ field at time n.

used for the time evolution at the first step of the Dirac field.

The algorithm presented above is for only one given configuration of initial charge. In the CGC and MV formalisms, one needs to average over many different configurations of initial color charge, hence the above algorithm needs to be repeated for many different configurations of initial color charge.

The algorithm for computing the initial condition for the gauge fields can be summarized as:

• *Generate the random distribution of color charges given by the MV model (see Eq. (2.29) and Sec. 2.2.3).*

• *From the charge distribution generated above compute the link matrices* $U_i^{(1)}$ *and* $U_i^{(2)}$ *for the two nuclei (with* $i = 1, 2$ *denoting the transverse directions). The link matrices are given by Eq. (3.23)*[1].

• *Find the link matrices in region (3) of the left panel in Fig. 3.1 at* $\tau = 0$*. This involves solving Eq. (3.21), which is done using the iterative method described in Sec. 3.2.*

• *Find the longitudinal field* π *at* $\tau = 0$ *using Eq. (3.22).*

• *Fix the Coulomb gauge in the transverse direction. This is done using the Fourier Acceleration (FA) method [54]*[2]*. Transform the gauge fields to the new gauge using the gauge transformation rules given in Sec. 3.1.2.*

For quark production, the gauge and quark field algorithm described above has to be supplemented with a function that computes the quark production amplitude using Eq. (3.77). This function has to be called after the evolution of the quark wavefunction.

[1]Finding the link matrices involves solving the Poisson equation for 2 dimensions. It can be solved numerically by first taking a Fourier transform to momentum space. This reduces the Poisson equation to an algebraic equation which can easily be solved. Then we take the inverse Fourier transform of the solution in momentum space, to obtain the solution of the Poisson equation in coordinate space.

[2]For large transverse lattices ($N^2 \gtrsim 100^2$) FA is expected to be the fastest method for fixing the transverse Coulomb gauge [55].

For photon production, the algorithm is more complex than for quark production. Since storing the quark wavefunction at all times is problematic[1], the other option is to evolve two quark/antiquark wavefunctions at the same time. Thus we need to modify the quark wavefunction time evolution algorithm described in this section to evolve in parallel two Dirac fields (Ψ_{q_1} and Ψ_{q_2}), task which is straightforward. Than, after every two time steps[2], one needs to compute the contribution to the photon spectrum using Eqs. (4.31)-(4.32). This gives the photon spectrum contribution for a given pair of initial fermions with momenta q_1 and q_2. The total spectrum is obtained by summing over all such pairs of momenta[3].

[1]The Dirac field for a $180^2 \times 400$ lattice in single precision needs 1.2 GB of memory. To store the quark wavefunction for 100 or more time steps requires more than 120 GB of storage space, which slows the numerical code due to reading and writing operations on the hard drive.

[2]The contribution to the photon spectrum needs to be computed only every two time steps since we modify only one of the Dirac field components at each time step, thus the Dirac field changes completely only after two time steps.

[3]Since the process of summing over all the momenta pairs (q_1, q_2) needs a large computational time, in practice we use a Monte Carlo method for approximating the momentum integral.

Bibliography

[1] **STAR** Collaboration, J. Adams *et al.*, "Experimental and theoretical challenges in the search for the quark gluon plasma: The STAR collaboration's critical assessment of the evidence from RHIC collisions," *Nucl. Phys.* **A757** (2005) 102–183, arXiv:nucl-ex/0501009.

[2] **BRAHMS** Collaboration, I. Arsene *et al.*, "Quark Gluon Plasma an Color Glass Condensate at RHIC? The perspective from the BRAHMS experiment," *Nucl. Phys.* **A757** (2005) 1–27, arXiv:nucl-ex/0410020.

[3] F. Karsch, "Lattice QCD at high temperature and density," *Lect. Notes Phys.* **583** (2002) 209–249, arXiv:hep-lat/0106019.

[4] K. Yagi, T. Hatsuda, and Y. Miake, "Quark-gluon plasma: From big bang to little bang," *Camb. Monogr. Part. Phys. Nucl. Phys. Cosmol.* **23** (2005) 1–446.

[5] S. Bethke, "QCD tests at e+ e- colliders," *Nucl. Phys. Proc. Suppl.* **64** (1998) 54–62, arXiv:hep-ex/9710030.

[6] J. E. Huth and M. L. Mangano, "QCD tests in $p\bar{p}$ collisions," *Ann. Rev. Nucl. Part. Sci.* **43** (1993) 585–634, arXiv:hep-ph/9302306.

[7] **Particle Data Group** Collaboration, C. Amsler *et al.*, "Review of particle physics," *Phys. Lett.* **B667** (2008) 1.

[8] M. E. Peskin and D. V. Schoeder, *An Introduction to Quantum Field Theory.* Addison-Wesley, 1995.

[9] E. Iancu and R. Venugopalan, "The color glass condensate and high energy scattering in QCD," arXiv:hep-ph/0303204.

[10] E. Iancu, A. Leonidov, and L. McLerran, "The colour glass condensate: An introduction," arXiv:hep-ph/0202270.

[11] **BRAHMS** Collaboration, I. G. Bearden *et al.*, "Nuclear stopping in Au + Au collisions at $\sqrt{s_{NN}} = 200$ GeV," *Phys. Rev. Lett.* **93** (2004) 102301, arXiv:nucl-ex/0312023.

[12] J. Pumplin *et al.*, "New generation of parton distributions with uncertainties from global QCD analysis," *JHEP* **07** (2002) 012, arXiv:hep-ph/0201195.

[13] **ZEUS** Collaboration, J. Breitweg *et al.*, "ZEUS results on the measurement and phenomenology of F2 at low x and low Q^2," *Eur. Phys. J.* **C7** (1999) 609–630, arXiv:hep-ex/9809005.

[14] E. Iancu, "The colour glass condensate.," *Nucl. Phys.* **A715** (2003) 219–232, arXiv:hep-ph/0210236.

[15] K. J. Golec-Biernat and M. Wusthoff, "Saturation effects in deep inelastic scattering at low Q^2 and its implications on diffraction," *Phys. Rev.* **D59** (1999) 014017, arXiv:hep-ph/9807513.

[16] L. D. McLerran and R. Venugopalan, "Computing quark and gluon distribution functions for very large nuclei," *Phys. Rev.* **D49** (1994) 2233–2241, arXiv:hep-ph/9309289.

[17] L. D. McLerran and R. Venugopalan, "Gluon distribution functions for very large nuclei at small transverse momentum," *Phys. Rev.* **D49** (1994) 3352–3355, arXiv:hep-ph/9311205.

[18] L. D. McLerran and R. Venugopalan, "Green's functions in the color field of a large nucleus," *Phys. Rev.* **D50** (1994) 2225–2233, arXiv:hep-ph/9402335.

[19] J. S. Schwinger, "Brownian motion of a quantum oscillator," *J. Math. Phys.* **2** (1961) 407–432.

[20] L. V. Keldysh, "Diagram technique for nonequilibrium processes," *Zh. Eksp. Teor. Fiz.* **47** (1964) 1515–1527.

[21] A. Kamenev, "Many-body theory of non-equilibrium systems," cond-mat/0412296.

[22] F. Gelis and R. Venugopalan, "Particle production in field theories coupled to strong external sources," *Nucl. Phys.* **A776** (2006) 135–171, arXiv:hep-ph/0601209.

[23] A. J. Baltz, F. Gelis, L. D. McLerran, and A. Peshier, "Coulomb corrections to e+ e- production in ultra- relativistic nuclear collisions," *Nucl. Phys.* **A695** (2001) 395–429, arXiv:nucl-th/0101024.

[24] A. Krasnitz and R. Venugopalan, "On colliding ultrarelativistic nuclei on a transverse lattice," arXiv:hep-ph/9706329.

[25] A. Krasnitz and R. Venugopalan, "Non-perturbative computation of gluon mini-jet production in nuclear collisions at very high energies," *Nucl. Phys.* **B557** (1999) 237, arXiv:hep-ph/9809433.

[26] F. Gelis, K. Kajantie, and T. Lappi, "Quark antiquark production from classical fields in heavy ion collisions: 1+1 dimensions," *Phys. Rev.* **C71** (2005) 024904, arXiv:hep-ph/0409058.

[27] T. Lappi, "Production of gluons in the classical field model for heavy ion collisions," *Phys. Rev.* **C67** (2003) 054903, arXiv:hep-ph/0303076.

[28] T. Lappi, "Rapidity distribution of gluons in the classical field model for heavy ion collisions," *Phys. Rev.* **C70** (2004) 054905, arXiv:hep-ph/0409328.

[29] F. Gelis, K. Kajantie, and T. Lappi, "Production of quark pairs from classical gluon fields," *Eur. Phys. J.* **A29** (2006) 89, arXiv:hep-ph/0509363.

[30] F. Gelis, K. Kajantie, and T. Lappi, "Quark-antiquark production from classical fields and chemical equilibration," *Nucl. Phys.* **A774** (2006) 809–812, arXiv:hep-ph/0509343.

[31] F. Gelis, K. Kajantie, and T. Lappi, "Chemical thermalization in relativistic heavy ion collisions," *Phys. Rev. Lett.* **96** (2006) 032304, arXiv:hep-ph/0508229.

[32] A. Krasnitz and R. Venugopalan, "The initial energy density of gluons produced in very high energy nuclear collisions," *Phys. Rev. Lett.* **84** (2000) 4309–4312, arXiv:hep-ph/9909203.

[33] A. Krasnitz, Y. Nara, and R. Venugopalan, "Coherent gluon production in very high energy heavy ion collisions," *Phys. Rev. Lett.* **87** (2001) 192302, arXiv:hep-ph/0108092.

[34] A. Kovner, L. D. McLerran, and H. Weigert, "Gluon production at high transverse momentum in the McLerran-Venugopalan model of nuclear structure functions," *Phys. Rev.* **D52** (1995) 3809–3814, arXiv:hep-ph/9505320.

[35] M. Gyulassy and L. D. McLerran, "Yang-Mills radiation in ultrarelativistic nuclear collisions," *Phys. Rev.* **C56** (1997) 2219–2228, arXiv:nucl-th/9704034.

[36] J. B. Kogut and L. Susskind, "Hamiltonian Formulation of Wilson's Lattice Gauge Theories," *Phys. Rev.* **D11** (1975) 395.

[37] A. J. Baltz and L. D. McLerran, "Two center light cone calculation of pair production induced by ultrarelativistic heavy ions," *Phys. Rev.* **C58** (1998) 1679–1688, arXiv:nucl-th/9804042.

[38] U. W. Heinz and P. F. Kolb, "Two RHIC puzzles: Early thermalization and the HBT problem," arXiv:hep-ph/0204061.

[39] F. Fillion-Gourdeau, M. Cautun, and S. Jeon *in preparation* .

[40] F. Fillion-Gourdeau, "Applications of many-body physics to relativistic heavy ion collisions," *PhD Thesis* (Montreal 2009) .

[41] J. J. Neumann, D. Seibert, and G. I. Fai, "Thermal photon production in high-energy nuclear collisions," *Phys. Rev.* **C51** (1995) 1460–1464, arXiv:nucl-th/9409008.

[42] J. Cleymans, K. Redlich, and D. K. Srivastava, "Thermal particle and photon production in Pb + Pb collisions with transverse flow," *Phys. Rev.* **C55** (1997) 1431–1442, arXiv:nucl-th/9611047.

[43] P. Aurenche, F. Gelis, and H. Zaraket, "KLN theorem, magnetic mass, and thermal photon production," *Phys. Rev.* **D61** (2000) 116001, arXiv:hep-ph/9911367.

[44] P. Aurenche, F. Gelis, and H. Zaraket, "Landau-Pomeranchuk-Migdal effect in thermal field theory," *Phys. Rev.* **D62** (2000) 096012, arXiv:hep-ph/0003326.

[45] P. Arnold, G. D. Moore, and L. G. Yaffe, "Photon emission from ultrarelativistic plasmas," *JHEP* **11** (2001) 057, arXiv:hep-ph/0109064.

[46] P. Arnold, G. D. Moore, and L. G. Yaffe, "Photon emission from quark gluon plasma: Complete leading order results," *JHEP* **12** (2001) 009, arXiv:hep-ph/0111107.

[47] P. Arnold, G. D. Moore, and L. G. Yaffe, "Photon and Gluon Emission in Relativistic Plasmas," *JHEP* **06** (2002) 030, arXiv:hep-ph/0204343.

[48] S. Turbide, R. Rapp, and C. Gale, "Hadronic production of thermal photons," *Phys. Rev.* **C69** (2004) 014903, arXiv:hep-ph/0308085.

[49] S. Turbide, C. Gale, S. Jeon, and G. D. Moore, "Energy loss of leading hadrons and direct photon production in evolving quark-gluon plasma," *Phys. Rev.* **C72** (2005) 014906, arXiv:hep-ph/0502248.

[50] F. Gelis and J. Jalilian-Marian, "Photon production in high energy proton nucleus collisions," *Phys. Rev.* **D66** (2002) 014021, arXiv:hep-ph/0205037.

[51] C. Itzykson and J.-B. Zuber, *Quantum Field Theory*. Dover Publications, 2006.

[52] A. Krasnitz, Y. Nara, and R. Venugopalan, "Elliptic flow of colored glass in high energy heavy ion collisions," *Phys. Lett.* **B554** (2003) 21–27, arXiv:hep-ph/0204361.

[53] A. Krasnitz, Y. Nara, and R. Venugopalan, "Gluon production in the color glass condensate model of collisions of ultrarelativistic finite nuclei," *Nucl. Phys.* **A717** (2003) 268–290, arXiv:hep-ph/0209269.

[54] C. T. H. Davies *et al.*, "Fourier Acceleration in Lattice Gauge Theories. 1. Landau Gauge Fixing," *Phys. Rev.* **D37** (1988) 1581.

[55] A. Cucchieri and T. Mendes, "Critical Slowing-Down in $SU(2)$ Landau Gauge-Fixing Algorithms," *Nucl. Phys.* **B471** (1996) 263–292, arXiv:hep-lat/9511020.